

AD/A-005 822

EXTENSION OF THE METHOD FOR PREDICTING  
SIX-DEGREE-OF-FREEDOM STORE SEPARA-  
TION TRAJECTORIES AT SPEEDS UP TO THE  
CRITICAL SPEED TO INCLUDE A FUSELAGE  
WITH NONCIRCULAR CROSS SECTION.  
VOLUME I - THEORETICAL METHODS AND  
COMPARISONS WITH EXPERIMENT

Marnix F. E. Dillenius, et al

Nielsen Engineering and Research, Incorporated

Prepared for:

Air Force Flight Dynamics Laboratory

November 1974

DISTRIBUTED BY:

**NTIS**

National Technical Information Service  
U. S. DEPARTMENT OF COMMERCE

# NOTICE

When Government drawings, specifications, or other data are used for any purpose other than in connection with a definitely related Government procurement operation, the United States Government thereby incurs no responsibility nor any obligation whatsoever; and the fact that the Government may have formulated, furnished, or in any way supplied the said drawings, specifications, or other data, is not to be regarded by implication or otherwise as in any manner licensing the holder or any other person or corporation, or conveying any rights or permission to manufacture, use, or sell any patented invention that may in any way be related thereto.

ACCESSION for		
NTIS	Waite Section	<input checked="" type="checkbox"/>
DDC	Bull Section	<input type="checkbox"/>
UNANNOUNCED		<input type="checkbox"/>
JUSTIFICATION.....		
BY .....		
DISTRIBUTION/AVAILABILITY CODES		
Dist.	AVAIL.	SPECIAL
A		

Copies of this report should not be returned unless return is required by security considerations, contractual obligations, or notice on a specific document.

UNCLASSIFIED  
Security Classification

AD/A-005822

DOCUMENT CONTROL DATA - R & D

(Security classification of title, body of abstract and indexing annotation must be entered when the overall report is classified)

1. ORIGINATING ACTIVITY (Corporate author) Nielsen Engineering & Research, Inc. 510 Clyde Avenue Mountain View, California 94043	2a. REPORT SECURITY CLASSIFICATION UNCLASSIFIED 2b. GROUP N/A
---	--

3. REPORT TITLE  
EXTENSION OF THE METHOD FOR PREDICTING SIX-DEGREE-OF-FREEDOM STORE SEPARATION TRAJECTORIES AT SPEEDS UP TO THE CRITICAL SPEED TO INCLUDE A FUSELAGE WITH NONCIRCULAR CROSS SECTION. Volume 1.- Theoretical Methods and Comparisons

4. DESCRIPTIVE NOTES (Type of report and inclusive dates) with Experiment  
Final Technical Report - March 1972 to February 1974

5. AUTHOR(S) (First name, middle initial, last name)  
Marnix F. E. Dillenius, Frederick K. Goodwin and Jack N. Nielsen

6. REPORT DATE November 1974	7a. TOTAL NO. OF PAGES 99	7b. NO. OF REFS 10
---------------------------------	------------------------------	-----------------------

8a. CONTRACT OR GRANT NO F33615-72-C-1375 b. PROJECT NO. 8219 c. Task No. 821902 d.	9a. ORIGINATOR'S REPORT NUMBER(S) NEAR TR 60 9b. OTHER REPORT NO(S) (Any other numbers that may be assigned this report) AFFDL-TR-74-130, Volume I
---	---

10. DISTRIBUTION STATEMENT  
Approved for public release; distribution unlimited.

11. SUPPLEMENTARY NOTES None	12. SPONSORING MILITARY ACTIVITY Air Force Flight Dynamics Lab. Wright-Patterson Air Force Base Ohio 45433
---------------------------------	---

13. ABSTRACT  
The primary objective of this report is to describe improvements and extensions which have been made to the method of predicting six-degree-of-freedom trajectories of stores released from fighter-bomber aircraft previously published by the authors in AFFDL-TR-72-83. In the present work, the circular fuselage restriction has been removed. Methods are presented for flow modeling fuselages with non-circular cross sections including canopies and engine air inlets. The inlet to free-stream velocity ratio can be varied between zero and unity. To more accurately account for wing-fuselage interference the wing-pylon vortex-lattice method used in the earlier work has been modified. A secondary objective is to present experimental results from a wind-tunnel test program designed to provide data to aid in developing and testing the theory. Comparisons between theory and experiment are presented for flow fields, store loading distributions, store forces and moments, and store trajectories.

Reproduced by  
NATIONAL TECHNICAL  
INFORMATION SERVICE  
U S Department of Commerce  
Springfield VA 22151

PRICES SUBJECT TO CHANGE

DD FORM 1473  
1 NOV 65

UNCLASSIFIED  
Security Classification

UNCLASSIFIED  
Security Classification

14. KEY WORDS	LINK A		LINK B		LINK C	
	ROLE	WT	ROLE	WT	ROLE	WT
External stores						
Aerodynamic interference						
Subsonic flow						
Store separation						
Aerodynamic loads						
Flow fields						

1 a

UNCLASSIFIED  
Security Classification

EXTENSION OF THE METHOD FOR PREDICTING  
SIX-DEGREE-OF-FREEDOM STORE SEPARATION  
TRAJECTORIES AT SPEEDS UP TO THE  
CRITICAL SPEED TO INCLUDE A FUSELAGE  
WITH NONCIRCULAR CROSS SECTION

Volume I.- Theoretical Methods and  
Comparisons with Experiment

Marnix F. E. Dillenius  
Frederick K. Goodwin  
Jack N. Nielsen

Approved for public release; distribution unlimited.

ic

## FOREWORD

This report, "Extension of the Method for Predicting Six-Degree-of-Freedom Store Separation Trajectories at Speeds up to the Critical Speed to Include a Fuselage with Noncircular Cross Section," describes a combined theoretical-experimental program directed toward extending a previously developed computer program for predicting the trajectory of an external store separated from an aircraft. Extensions were made to model realistic fuselage shapes including canopies, noncircular cross sections, and engine air inlets. This volume, Volume I.- "Theoretical Methods and Comparisons with Experiment," describes the theoretical approach and presents extensive comparisons with experimental data. The second volume, Volume II.- "Users Manual for the Computer Programs," presents detailed instructions on the use of the computer programs.

The work was carried out by Nielsen Engineering & Research, Inc., 510 Clyde Avenue, Mountain View, California 94043, under Contract No. F33615-72-C-1375. The contract was initiated under Project 8219, Task 821902, of the Air Force Flight Dynamics Laboratory. The Air Force Project Engineer on the contract was Mr. Jerry E. Jenkins, AFFDL/FGC. The report number assigned by Nielsen Engineering & Research, Inc. is NEAR TR 60.

The authors wish to thank Mr. Jenkins and Mr. Calvin L. Dyer, AFFDL/FGC, for their assistance during the course of the investigation. Also, they would like to thank Mr. James R. Myers and Mr. Robert H. Roberts of the 4T Projects Branch, Propulsion Wind-Tunnel Facility, Arnold Engineering Development Center, for the timely performance of the experimental test program.

The work documented in this report was started on March 1, 1972, and was effectively concluded with the submission of this report. The report was submitted by the authors in March 1974.

This technical report has been reviewed and is approved for publication.

FOR THE COMMANDER

---

E. H. Flinn, Acting Chief  
Control Criteria Branch  
Flight Control Division

---

*Jerry E. Jenkins*  
Jerry E. Jenkins  
Project Engineer  
Control Criteria Branch  
Flight Control Division

## ABSTRACT

The primary objective of this report is to describe improvements and extensions which have been made to the method of predicting six-degree-of-freedom trajectories of stores released from fighter-bomber aircraft previously published by the authors in AFFDL-TR-72-83. In the present work, the circular fuselage restriction has been removed. Methods are presented for flow modeling fuselages with noncircular cross sections including canopies and engine air inlets. The inlet to free-stream velocity ratio can be varied between zero and unity. To more accurately account for wing-fuselage interference the wing-pylon vortex-lattice method used in the earlier work has been modified. A secondary objective is to present experimental results from a wind-tunnel test program designed to provide data to aid in developing and testing the theory. Comparisons between theory and experiment are presented for flow fields, store loading distributions, store forces and moments, and store trajectories.

## TABLE OF CONTENTS

<u>Section</u>	<u>Page No.</u>
1. INTRODUCTION	1
2. MATHEMATICAL MODELS FOR DETERMINING FLOW FIELD	2
2.1 Fuselage with Circular Cross Section	3
2.2 Fuselage with Noncircular Cross Section	4
2.2.1 Choice of potentials	4
2.2.2 Flow tangency boundary condition	6
2.2.3 Streamwise slope of body surface	8
2.2.4 Flow tangency condition rewritten	10
2.2.5 Solution of the simultaneous equations	13
2.2.6 Selection of number of control points and number of polar harmonics	15
2.3 Fuselage Mounted Air Inlets	18
2.4 Wing-Pylon Flow Model	19
2.4.1 Vortex-lattice model with imaging to account for wing-fuselage interference	20
2.4.2 Thickness model	25
2.5 Store and Rack Flow Models	26
3. FORCE AND MOMENT CALCULATION	26
4. CALCULATION OF STORE TRAJECTORIES	27
5. COMPARISONS WITH EXPERIMENTAL DATA	28
5.1 Wind-Tunnel Model Description	28
5.2 Flow Fields	29
5.3 Store Load Distributions	32
5.4 Store Forces and Moments	33
5.5 Store Trajectories	34
6. CONCLUDING REMARKS	35
REFERENCES	84

Preceding page blank



# LIST OF ILLUSTRATIONS

<u>Figure</u>	<u>Page No.</u>
1.- Coordinate system for an axisymmetric body.	37
2.- Coordinate systems associated with general noncircular body.	38
3.- Example body contours. (a) Body contour A. (b) Body contour B.	39
4.- Range of validity tests for body contour A; $\alpha = 6^\circ$ , $M_\infty = 0.4$ . (a) Upwash velocity.	40
4.- Concluded. (b) Sidewash velocity.	41
5.- Range of validity tests for body contour B; $\alpha = 6^\circ$ , $M_\infty = 0.4$ . (a) Upwash velocity.	42
5.- Concluded. (b) Sidewash velocity.	43
6.- Polar harmonic coefficients $a_n$ calculated for body contour A with 24 control points and 16 and 23 polar harmonics; $\alpha = 6^\circ$ , $M_\infty = 0.4$ .	44
7.- Polar harmonic coefficients $a_n$ calculated for body contour B with 32 control points and 14 and 30 polar harmonics; $\alpha = 6^\circ$ , $M_\infty = 0.4$ .	45
8.- Horseshoe vortex imaging method shown in elevation.	46
9.- Horseshoe vortex imaging method shown in planform.	47
10.- Enlargement of image vortex region shown in elevation.	48
11.- Wing-fuselage combination.	49
12.- Modified wind-tunnel model. (a) Canopy mounted on fuselage nose.	50
12.- Continued. (b) Wing and duct assembly attached to circular fuselage.	51
12.- Concluded. (c) Top view of wing and duct assembly attached to circular fuselage.	52
13.- Ogive-cylinder store with rectangular cruciform fins.	53
14.- Velocity vector plot for noncircular fuselage in crossflow plane 19.66 inches aft of nose tip.	54
15.- Distribution of upwash 3 inches under the fuselage centerline for the circular fuselage and for noncircular addition attached to the fuselage; $M_\infty = 0.4$ . (a) $\alpha = 0^\circ$ .	55

# LIST OF ILLUSTRATIONS (cont.)

<u>Figure</u>	<u>Page No.</u>
15.- Concluded. (b) $\alpha = 6^\circ$ .	56
16.- Velocity vector plot for wing attached to noncircular fuselage in crossflow plane 19.66 inches aft of nose tip.	57
17.- Distribution of upwash 3 inches under the fuselage centerline; $\alpha = 6^\circ$ , $M_\infty = 0.4$ . (a) Effects of wind-tunnel model build-up.	58
17.- Concluded. (b) Effects of inlet velocity ratio.	59
18.- Distribution of upwash 3 inches under the fuselage centerline; $\alpha = 0^\circ$ , $M_\infty = 0.4$ . (a) Effects of wind-tunnel model build-up.	60
18.- Concluded. (b) Effects of inlet velocity ratio.	61
19.- Effect of wind-tunnel model build-up on the flow field in the region the store centerline would occupy if the store was present; $\alpha = 6^\circ$ , $M_\infty = 0.4$ . (a) Upwash distribution.	62
19.- Concluded. (b) Sidewash distribution.	63
20. Coordinate systems fixed in store and positive velocity and force and moment directions.	64
21.- Effect of air inlet velocity ratio on the flow field in the region the store centerline would occupy if the store was present; $\alpha = 6^\circ$ , $M_\infty = 0.4$ . (a) Upwash distribution.	65
21.- Concluded. (b) Sidewash distribution.	66
22.- Effect of wind-tunnel model build-up on the flow field in the region the store centerline would occupy if the store was present; $\alpha = 0^\circ$ , $M_\infty = 0.4$ . (a) Upwash distribution.	67
22.- Concluded. (b) Sidewash distribution.	68
23.- Effect of air inlet velocity ratio on the flow field in the region the store centerline would occupy if the store was present; $\alpha = 0^\circ$ , $M_\infty = 0.4$ . (a) Upwash distribution.	69
23.- Concluded. (b) Sidewash distribution.	70
24.- Effect of wind-tunnel model build-up on load distribution of attached store; $\alpha = 6^\circ$ , $M_\infty = 0.4$ . (a) Normal-force distribution.	71
24.- Concluded. (b) Side-force distribution.	72
25.- Effect of inlet velocity ratio on load distribution of attached store; $\alpha = 6^\circ$ , $M_\infty = 0.4$ . (a) Normal-force distribution.	73

# LIST OF ILLUSTRATIONS (conc.)

<u>Figure</u>	<u>Page No.</u>
25.- Concluded. (b) Side-force distribution.	74
26.- Effect of wind-tunnel model build-up on load distribution of attached store; $\alpha = 0^\circ$ , $M_\infty = 0.4$ . (a) Normal-force distribution.	75
26.- Concluded. (b) Side-force distribution.	76
27.- Effect of inlet velocity ratio on load distribution of attached store; $\alpha = 0^\circ$ , $M_\infty = 0.4$ . (a) Normal-force distribution.	77
27.- Concluded. (b) Side-force distribution.	78
28.- Effect of wind-tunnel model build-up on store forces and moments; $M_\infty = 0.4$ . (a) Normal- and side-force coefficients.	79
28.- Concluded. (b) Pitching- and yawing-moment coefficients.	80
29.- Effect of inlet velocity ratio on store forces and moments; $M_\infty = 0.4$ . (a) Normal- and side-force coefficients.	81
29.- Concluded. (b) Pitching- and yawing-moment coefficients.	82
30.- Comparison between calculated and captive-store trajectories for a store released from the one-third semispan pylon; $\alpha = 6^\circ$ , $M_\infty = 0.4$ , no damping.	83

# LIST OF SYMBOLS

$a$	local body radius
$a_n$	polar harmonic singularity coefficient
$C_m$	store pitching-moment coefficient, pitching moment/ $q_{\infty} S_R \ell_R$ , positive nose up and taken about store midpoint
$C_n$	store yawing-moment coefficient, yawing moment/ $q_{\infty} S_R \ell_R$ , positive nose to the right and taken about store midpoint
$C_N$	store normal-force coefficient, normal force/ $q_{\infty} S_R$ , positive up
$C_Y$	store side-force coefficient, side force/ $q_{\infty} S_R$ , positive to the right
$d$	maximum store diameter
$F_{iu}, F_{iv}, F_{iw}$	backwash, sidewash, and downwash influence coefficients for a wing image vortex; positive in the $x_w, y_w, z_w$ directions of figures 8 and 9
$F_u, F_v, F_w$	backwash, sidewash, and downwash influence coefficients for a wing or pylon vortex; positive in the $x_w, y_w, z_w$ directions of figures 8 and 9
$\ell$	body length
$\ell_R$	reference length, taken equal to $d$
$\ell_s$	store length
$m$	body contour slope given by equation (22)
$M_{\infty}$	free-stream Mach number
$q_{\infty s}$	ejected store free-stream dynamic pressure
$\vec{q}_{\infty}$	perturbation velocity vector
$r$	radial distance in crossflow plane
$s_{iv}$	semispan of a wing image vortex
$S$	local body cross-sectional area
$S'(x)$	rate of change of body cross-sectional area

$S_R$	reference area, $\pi d^2/4$
$t$	time, seconds
$u, v, w$	section 2.1, incompressible perturbation velocities in $x, y, z$ directions of figure 1; section 2.4, incompressible perturbation velocities in $x_w, y_w, z_w$ directions of figures 8 and 9; figures 4 and 5, compressible perturbation velocities in $x, y, z$ directions of figure 1
$u_i, v_i, w_i$	incompressible externally induced perturbation velocities in section 2.4
$u_r, u_\theta$	incompressible perturbation velocities in polar coordinates and associated with $\phi_2$ , section 2.2
$u_x, u_v, u_\tau$	incompressible perturbation velocities in $x, v, \tau$ coordinate system of section 2.2
$U_x, U_v, U_\tau$	incompressible free-stream velocity components in $x, v, \tau$ coordinate system of section 2.2
$v_r$	incompressible radial velocity in $y-z$ plane of figure 1
$V, W$	incompressible free-stream velocity components in $y$ and $z$ directions of section 2.2.4
$V_D$	velocity inside engine inlet
$V_s, W_s$	compressible velocities in store body coordinate system, see figure 20
$V_\infty$	free-stream velocity
$\vec{V}_\infty$	free-stream velocity vector in incompressible space
$V_{\infty s}$	separated store free-stream velocity
$W$	incompressible upwash in section 2.1
$W_B$	upwash velocity in fuselage coordinate system, positive in $-z$ direction of figures 1 and 2
$W_C$	complex potential given by equation (1)
$x, y, z$	section 2.1, coordinate system fixed in nose of axisymmetric body in incompressible space, see figure 1; section 2.2, coordinate system fixed in nose of general noncircular body in incompressible space, see figure 2; section 2.4, coordinate system with origin at midspan of the bound leg of a horseshoe vortex in incompressible space, see figure 2 of reference 1

$x_{iv,w}, y_{iv,w}, z_{iv,w}$	coordinates of bound-leg midspan of a wing image vortex in $x_w, y_w, z_w$ wing coordinate system in incompressible space
$x_s, y_s, z_s$	coordinate system in compressible space fixed in separated store with origin at store nose, see figure 20
$x_{s,m}$	$x_s$ location of store moment center
$x_w, y_w, z_w$	wing coordinate system in incompressible space, see figures 8 and 9
$x_B, y_B, z_B$	fuselage coordinate system, see figures 1 and 2
$\alpha$	fuselage and store angle of attack
$\alpha_l$	local angle of attack due to wing twist and camber
$\Gamma$	strength of a horseshoe vortex
$\theta$	polar angle, see figure 2
$\vec{v}, \vec{\tau}$	vectors normal to and tangential to the crossflow plane contour, see section 2.2.2 and figure 2
$\xi, \eta, \zeta$	axial, lateral, and vertical displacements, respectively, of the store center of gravity relative to the carriage position on the pylon in the fuselage coordinate system; positive forward, to the right, and downward, respectively
$\phi$	angle defined by equation (21)
$\phi_c$	complete potential for a body defined by equation (5)
$\phi_e$	potential associated with equivalent body of revolution
$\phi_{iv}$	dihedral angle of image horseshoe vortex
$\phi_v$	dihedral angle of the $v^{th}$ vortex on the exposed wing panel
$\phi_2$	crossflow plane potential associated with the contour of a general body
$\psi$	angle defined by equation (35)
$\psi_{iv}$	sweep angle of the bound leg of an image horseshoe vortex
$\psi_v$	sweep angle of the bound leg of a horseshoe vortex on the exposed wing panel
$\Delta\psi, \Delta\theta$	changes in yaw and pitch angles, respectively, of store from time = 0 values; positive nose to the right and nose up

WIND-TUNNEL MODEL  
COMPONENT DESIGNATION  
(see figure 12)

$A_1$	noncircular addition
$A_2D$	duct assembly
$B_1$	circular fuselage without wing
$B_2$	circular fuselage to which wing can be attached
$C_1$	canopy
$N_1$	uncambered nose
$P_{1/3}$	pylon at 1/3 semispan location
$W$	wing

EXTENSION OF THE METHOD FOR PREDICTING SIX-DEGREE-OF-FREEDOM  
STORE SEPARATION TRAJECTORIES AT SPEEDS UP TO THE CRITICAL  
SPEED TO INCLUDE A FUSELAGE WITH NONCIRCULAR CROSS SECTION

Volume I.- Theoretical Methods and Comparisons  
with Experiment

1. INTRODUCTION

This report is the final technical report describing a combined theoretical-experimental program which has been carried out with the objective of extending the six-degree-of-freedom store separation trajectory prediction method of references 1 and 2 to more realistic fuselage configurations.

In the earlier work, the fuselage was limited to an uncambered body with a circular cross section. In the present work, this restriction has been removed. The shape of the fuselage cross section is arbitrary and may vary from one axial station to the next along the fuselage. In this manner a fuselage of general cross-sectional shape can be modeled including camber, canopy, and engine inlets. The modeling of the engine inlets allows the inlet to free-stream velocity ratio to be one or less.

Two further improvements have been made to the work of references 1 and 2. For a fuselage of circular cross section (this case is included as an option in the computer program) fuselage angle-of-attack effects are included in the wing-pylon vortex-lattice boundary condition and in the trajectories of all stores. Previously, the effects were included only in the trajectories of stores separated from under the fuselage.

The second improvement which has been made is to the wing-pylon vortex-lattice model. Vortices are now laid out only on the exposed wing panels and imaged inside the fuselage. For a cylindrical fuselage this results in no flow through the fuselage surface and thus a much more accurate prediction of the flow field in the region of the wing-fuselage juncture. For noncylindrical fuselages, some flow exists through the actual surface but the wing-fuselage interference is still modeled more accurately.

The experimental program carried out in conjunction with this work was directed toward providing data to aid in the development of the flow models for the noncircular fuselage and the engine inlets. The basic



model was an uncambered fuselage of circular cross section. Through the systematic addition of a wing, an attachment making the body noncircular in cross section, engine inlets, a canopy, and a cambered nose, interference effects could be isolated. At each stage of the model build-up, flow-field survey data were taken. At most stages of the build-up, store pressure distribution and force and moment data were obtained. A representative set of trajectories was also taken.

The next section of this report will describe the mathematical models for the various aircraft components. Following this the flow-field calculation, the force and moment calculation, and the trajectory calculation will be described. Only methods which are new or have been significantly changed will be described in detail. If only minor modifications have been made, these will be described briefly with reference made to the work of reference 1 or the earlier work of reference 3.

Finally, comparisons are made between the theory and results obtained during the wind-tunnel program in order to assess the accuracy of the theoretical methods in predicting the flow field about wing-fuselage configurations with a fuselage which is noncircular in cross section. Comparisons are shown for the step-by-step build-up of the configuration and for various inlet velocity ratios. For many of the same configurations comparisons are presented between measured and predicted store load distributions and forces and moments. Comparisons are also presented between captive-store trajectories and those predicted by the six-degree-of-freedom trajectory program.

## 2. MATHEMATICAL MODELS FOR DETERMINING FLOW FIELD

This section of the report will describe the mathematical models for the various aircraft components. All of the models to be described are for the equivalent incompressible configuration. The determination of this configuration from the actual configuration is discussed in section 3 of reference 1. Two fuselage models will first be described. The first is for an uncambered fuselage with a circular cross section at all axial stations and the second is for a fuselage whose cross section may be noncircular. Next, the method of accounting for fuselage mounted air inlets, including inlet to free-stream velocity ratio, will be presented. This will be followed by a description of the wing-pylon flow model. The

revised wing-pylon vortex-lattice model will be described in detail and changes in the thickness model will be pointed out. Finally, the store and rack flow models will be briefly mentioned.

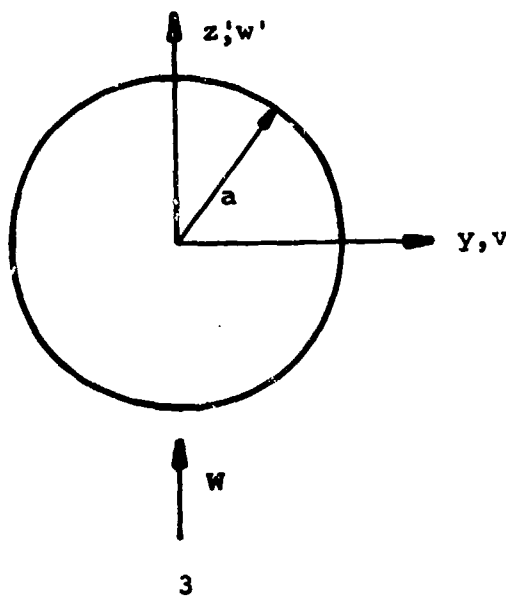
## 2.1 Fuselage with Circular Cross Section

The flow model for a fuselage with circular cross section consists of two parts. The first part models the volume distribution of the fuselage by a distribution of three-dimensional point sources along the body longitudinal axis. The source strengths are determined in the manner described in section 4.1 of reference 3. The coordinate system associated with the circular fuselage is shown in figure 1 of the present report. The perturbation velocities  $u$  and  $v_r$  induced at point  $x, r$  by the source distribution are given by equations (4) and (5) of reference 1.

The second part of the circular fuselage model is a two-dimensional crossflow plane solution which accounts for fuselage angle-of-attack effects, the so-called Beskin upwash effect. This is a crossflow velocity field and is obtained from the complex potential given on page 29 of reference 4. The formal operations required to obtain the crossflow velocities will now be shown. For the case of uniform upwash  $W$ , the complex potential in the crossflow plane is given by

$$W_C(\sigma) = -iW\left(\sigma - \frac{a^2}{\sigma}\right) \quad (1)$$

where  $\sigma = y + iz'$ . The meanings of the symbols are shown in the sketch:



Note that  $z'$  is opposite in direction to the  $z$  coordinate of the general body coordinate system in figure 1. This complex potential includes the free-stream component in the crossflow plane which will be subtracted, subsequently, in order to obtain expressions for the perturbation velocities.

The perturbation velocities are related to the complex potential through

$$v - iw' = \frac{d(W_c + iW\sigma)}{d\sigma} = -iW \frac{a^2}{\sigma^2} \quad (2)$$

Substituting for  $\sigma$  and multiplying the numerator and denominator on the right-hand side by the conjugate of  $\sigma^2$

$$v - iw' = -iW \frac{a^2 (y - iz')^2}{(y^2 + z'^2)^2} \quad (3)$$

Equating the real and imaginary parts of the equation and putting  $z = -z'$  and  $w = -w'$  leads to the following results for the perturbation velocities induced by a circular fuselage due to angle of attack

$$\left. \begin{aligned} v(y,z) &= \frac{2yz}{(y^2 + z^2)^2} a^2 W \\ w(y,z) &= - \frac{y^2 - z^2}{(y^2 + z^2)^2} a^2 W \end{aligned} \right\} \quad (4)$$

These last expressions are in the coordinate system of figure 1 with  $v$  and  $w$  positive in the positive  $y$  and  $z$  directions, respectively.

## 2.2 Fuselage with Noncircular Cross Section

### 2.2.1 Choice of potentials

The approach employed to model bodies with noncircular cross section is based on the equivalence rule cited in reference 5. This rule states that the following conditions hold for a general slender body:

- (a) "Far away from a general slender body, the flow becomes axisymmetric and equal to the flow around the equivalent body of revolution."

- (b) "Near the general slender body, the flow differs from that around the equivalent body of revolution by a two-dimensional constant density crossflow part that makes the tangency condition at the actual body surface satisfied."

The equivalent body of revolution is an axisymmetric body with the same cross-sectional area distribution along its longitudinal axis as the actual body. The outer axisymmetric flow is given by the potential  $\phi_e$  associated with this equivalent body. The inner flow is represented by a two-dimensional potential  $\phi_2$  which in the outer limit becomes  $[U_x(x)/2\pi V_\infty] S'(x) \ln r$ . The total velocity in the axial direction  $x$  of the body is  $U_x(x)$  and  $S'(x)$  is the rate of change of the cross-sectional area  $S$  with  $x$ . In accordance with (b), body angle of attack and contour variations are accounted for in the flow tangency condition applied on the actual body surface. This boundary condition will be analyzed in a later section. A solution valid for the entire flow field is then given by a composite solution

$$\phi_c(r, \theta) = \phi_e(r) + \phi_2(r, \theta) - \frac{U_x(x)}{2\pi V_\infty} S'(x) \ln r \quad (5)$$

where  $r$  is the radial distance from the body centerline, see figure 2.

In the method used here, the inner potential is composed of higher order singularities, given by polar harmonics, and a two-dimensional source term

$$\phi_2(r, \theta) = \sum_{n=1}^{MH} \frac{a_n \cos n\theta}{r^n(\theta)} + \frac{U_x(x)}{2\pi V_\infty} S'(x) \ln r \quad (6)$$

where  $MH$  is the number of polar harmonics. The definitions of  $r$  and  $\theta$  are shown in figure 2. The underlying assumptions and derivations associated with the two-dimensional polar harmonics are described in great detail in reference 4.

Potential  $\phi_e$  of the equivalent body is determined on the basis of flow modeling a body of revolution at zero angle of attack with the same cross-sectional area distribution  $S(x)$  as the actual body. The inner potential  $\phi_2$  is determined independently from  $\phi_e$  in the crossflow plane

and satisfies the flow tangency condition on the actual body contour. The polar harmonics are "excited" by either or both angle of attack and change in cross-sectional area  $S'(x)$ . It should be noted here that both  $\phi_e$  and  $\phi_z$  depend on  $S'(x)$ .

The harmonic terms as expressed under the summation in equation (6) require flow symmetry about the vertical plane. Consequently, the body contour in figure 2 must also be symmetric about the  $x$ - $z$  plane.

In actual practice, the following procedures are followed. The strengths of the three-dimensional potentials representing the equivalent body of revolution are determined from the flow tangency condition applied at points on the surface of the equivalent body at zero angle of attack using the method of section 4.1 in reference 3. Polar harmonic solutions are then obtained at a number of crossflow plane stations along the body longitudinal,  $x$ , axis. The  $x$  range over which the stations are distributed is that where the local flow needs to be calculated. For the case of a noncircular fuselage, the range includes the  $x$  range the wing occupies and the  $x$  range the store is expected to occupy during its trajectory. The density of placement of the crossflow stations depends on how rapidly the body contour is changing shape or how rapidly the cross-sectional area is changing with respect to the longitudinal coordinate,  $x$ .

At each crossflow plane station, a number of control points are distributed at equal angular spacings in  $\theta$  on the body contour over the half range,  $\theta = 0^\circ$  to  $\theta = 180^\circ$ . The first and last control points are displaced from the positive and negative  $z$ -axes, respectively, by an angle equal to one half of the angular spacing, see figure 2.

The flow tangency condition, to be discussed next, is applied at the control points resulting in a finite set of simultaneous equations in terms of the unknown polar harmonic coefficients. The solution is obtained in the least-square sense.

#### 2.2.2 Flow tangency boundary condition

For each control point on the crossflow plane contour a coordinate system  $v, \tau$  is introduced such that  $v$  is in the direction normal to and  $\tau$  tangential to the contour at the point. Figure 2 shows the unit vectors associated with those directions. Assume, see reference 5, that the shape

of the body surface can be expressed as

$$F(x, v, \tau) = 0, \quad -l \leq x \leq 0 \quad (7)$$

where  $l$  is the body length. Then the unit vector normal to the body surface (not the contour) at the point is given in reference 6 as

$$\vec{e}_n = \frac{\text{grad } F}{|\text{grad } F|} \quad (8)$$

where

$$\text{grad } F = \frac{\partial F}{\partial x} \vec{e}_x + \frac{\partial F}{\partial v} \vec{e}_v + \frac{\partial F}{\partial \tau} \vec{e}_\tau \quad (9)$$

If the free-stream (not necessarily uniform) and the perturbation velocity vectors are  $\vec{V}_\infty = \vec{V}_\infty(x, v, \tau)$  and  $\vec{q}_\infty = \vec{q}_\infty(x, v, \tau)$ , respectively, the flow tangency boundary condition in the  $(x, v, \tau)$  system is

$$[\vec{V}_\infty(x, v, \tau) + \vec{q}_\infty(x, v, \tau)] \cdot \vec{e}_n = 0 \quad (10)$$

where the bracketed term represents the resultant velocity vector. Expanding the vectors inside the brackets in terms of their respective components in the  $x, v$  and  $\tau$  directions results in

$$\vec{V}_\infty(x, v, \tau) + \vec{q}_\infty(x, v, \tau) = (U_x + u_x) \vec{e}_x + (U_v + u_v) \vec{e}_v + (U_\tau + u_\tau) \vec{e}_\tau \quad (11)$$

and substituting equations (8), (9), and (11) into (10), the boundary condition becomes

$$(U_x + u_x) \frac{\partial F}{\partial x} + (U_v + u_v) \frac{\partial F}{\partial v} + (U_\tau + u_\tau) \frac{\partial F}{\partial \tau} = 0 \quad (12)$$

This equation represents the nonlinear flow tangency condition for any body situated in a nonuniform flow. In the treatment which follows, geometrical properties of the unit vectors  $\vec{e}_n, \vec{e}_v$  and  $\vec{e}_\tau$  will be used to simplify equation (12) without any loss of generality.

The unit vectors  $\vec{e}_n$  and  $\vec{e}_v$  drawn at a point on the surface of the body lie in the same longitudinal plane, see figure 2. Since  $\vec{e}_v$  is perpendicular by definition to  $\vec{e}_\tau$ , then  $\vec{e}_n$  is also at a right angle to  $\vec{e}_\tau$ . Therefore,

$$\vec{e}_n \cdot \vec{e}_\tau = 0 \quad (13)$$

and with the aid of equations (8) and (9), equation (13) gives

$$\left( \frac{\partial F}{\partial x} \vec{e}_x + \frac{\partial F}{\partial v} \vec{e}_v + \frac{\partial F}{\partial \tau} \vec{e}_\tau \right) \cdot \vec{e}_\tau = 0 \quad (14)$$

As a result, on the body surface

$$\frac{\partial F}{\partial \tau} = 0 \quad (15)$$

This fact is actually obvious since  $F(x, v, \tau)$  is constant and equal to zero on the body surface and, therefore, invariant with respect to the tangential vector  $\vec{e}_\tau$ . From the specification of the body surface as given by equation (7), the differential of  $F(x, v, \tau)$  is

$$dF(x, v, \tau) = \frac{\partial F}{\partial x} dx + \frac{\partial F}{\partial v} dv + \frac{\partial F}{\partial \tau} d\tau = 0 \quad (16)$$

Together with equation (15), equation (16) yields the relation

$$\frac{\partial F}{\partial x} = - \frac{\partial F}{\partial v} \frac{dv}{dx} \quad (17)$$

Finally, substituting equations (15) and (17) into (12) yields the non-linear flow tangency condition that must be satisfied at points on the surface of a general body.

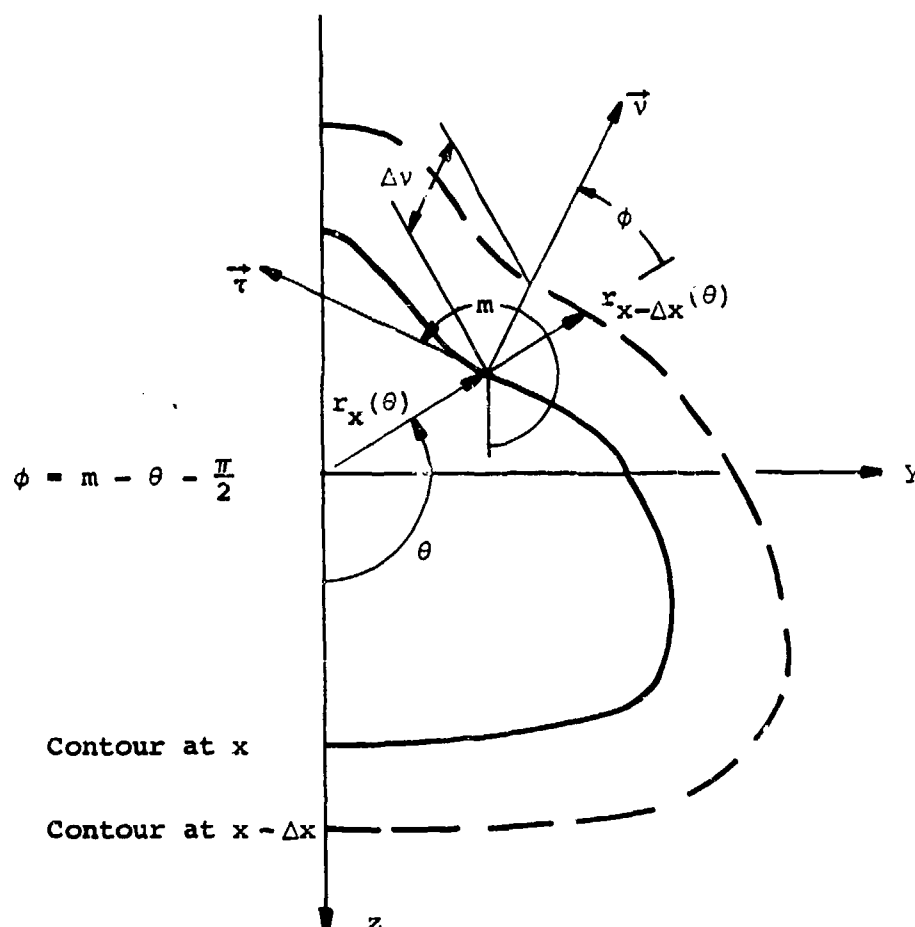
$$\left[ U_x(x) + u_x(x, v, \tau) \right] \frac{dv}{dx} = U_v(x) + u_v(x, v, \tau) \quad (18)$$

The definition and determination of the streamwise body slope,  $dv/dx$ , will be discussed next. Then, the velocities on the right-hand side of equation (18) will be rewritten in terms of components along the  $y$  and  $z$  axes and the  $\theta$  and  $x$  directions.

### 2.2.3 Streamwise slope of body surface

For purposes of deriving an analytical expression for the streamwise body slope, the following sketch is drawn consistent with the conventions already established in figure 2. The analysis is in accordance with the principles stated in reference 5. Note that the body radius  $r$  and its

derivatives with respect to  $\theta$  must be single valued and continuous for a given value of  $\theta$ .



Vector  $\vec{v}$  is perpendicular to and  $\vec{\tau}$  tangential to the body contour at  $x$ . Let  $\Delta v$  denote the change measured in the direction of  $\vec{v}$  of the location of the contour when going in a longitudinal plane from the cross section at  $x$  to the one at  $x - \Delta x$  ( $\Delta x$  is a positive quantity and  $x$  is negative behind the tip of the body nose, see fig. 2). The slope of the body in this longitudinal plane is then given by

$$\frac{dy(\theta)}{dx} = \lim_{\Delta x \rightarrow 0} \frac{\Delta y(\theta)}{\Delta x} \quad (19)$$



In the present work this body slope is approximated by

$$\left. \begin{aligned} \frac{dy(\theta)}{dx} &\approx \frac{\Delta r(\theta) \cos \phi}{\Delta x} \\ \Delta r(\theta) &= r_{x-\Delta x}(\theta) - r_x(\theta) \end{aligned} \right\} \quad (20)$$

This approximation should be sufficiently accurate for body contours varying smoothly from one  $x$  location to the next.

From the sketch above, angle  $\phi$  between the normal  $\vec{v}$  and the radial direction  $r$  can be expressed in terms of the contour slope  $m$  and the polar angle  $\theta$ :

$$\phi = m - \theta - \frac{\pi}{2} \quad (21)$$

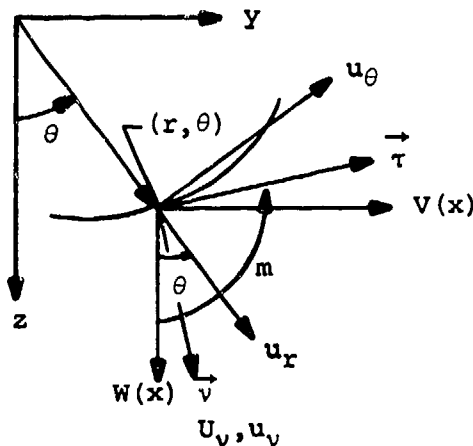
The body contour slope  $m$  ( $0 \leq m \leq 2\pi$ ) is found from

$$m = \lim_{\Delta\theta \rightarrow 0} \left[ \tan^{-1} \frac{\frac{\Delta y}{\Delta\theta}}{\frac{\Delta z}{\Delta\theta}} \right] = \tan^{-1} \left[ \frac{\frac{dr(\theta)}{d\theta} \sin \theta + r(\theta) \cos \theta}{\frac{dr(\theta)}{d\theta} \cos \theta - r(\theta) \sin \theta} \right] \quad (22)$$

since  $z = r(\theta) \cos \theta$  and  $y = r(\theta) \sin \theta$ .

#### 2.2.4 Flow tangency condition rewritten

The nonlinear form of the flow tangency condition as given by equation (18) will now be rewritten in a more useful form. With the aid of the sketch below,  $U_v(x)$  will be expressed in terms of the free-stream



components  $V(x)$  and  $W(x)$ , and  $u_v(x, v, \tau)$  will be rewritten in terms of the radial and tangential perturbation velocities  $u_r(r, \theta)$  and  $u_\theta(r, \theta)$ . Adding the free-stream component contributions in the  $\vec{v}$  direction gives (note  $\vec{v}$  perpendicular to  $\vec{\tau}$ ):

$$U_v(x, r, \theta) = W(x) \cos(m - \frac{\pi}{2}) + V(x) \sin(m - \frac{\pi}{2}) \quad (23)$$

and adding the  $u_r$  and  $u_\theta$  contributions results in

$$u_v(r, \theta) = u_r(r, \theta) \cos[\theta - (m - \frac{\pi}{2})] - u_\theta(r, \theta) \sin[\theta - (m - \frac{\pi}{2})] \quad (24)$$

According to the section concerned with the choice of potentials, the inner potential  $\phi_2$  is the potential that satisfies the flow tangency condition on the actual body surface. This assumes that the effects of the other two potentials  $\phi_e$  and  $-(U_x(x)/2\pi V_\infty) S'(x) \ln r$ , see equation (5), cancel one another on the body surface. In fact, this condition holds true on the surface of the equivalent body and is satisfied approximately on the actual body surface. For the cases studied in this report, it was found that inclusion of the contributions of the other two potentials in the boundary condition had an extremely small effect. Therefore, the effects of only the inner potential  $\phi_2$  will be considered in the boundary condition. In polar coordinates, the perturbation velocities in equation (24) are related to the crossflow or inner potential  $\phi_2$  as follows

$$\left. \begin{aligned} \frac{u_r}{V_\infty}(r, \theta) &= \frac{\partial \phi_2(r, \theta)}{\partial r} \\ \frac{u_\theta}{V_\infty}(r, \theta) &= \frac{1}{r(\theta)} \frac{\partial \phi_2(r, \theta)}{\partial \theta} \end{aligned} \right\} \quad (25)$$

It should be noted that the inner potential  $\phi_2$  as specified in equation (6) includes the assumption of flow symmetry about the vertical or x-z plane. Sideslip or yaw is therefore not considered in this analysis but would be a simple extension by adding additional polar harmonics of the  $\sin n\theta$  type. Differentiation of equation (6) gives

$$\frac{u_r}{V_\infty}(r, \theta) = - \sum_{n=1}^{MH} \frac{n a_n \cos n\theta}{r^{n+1}(\theta)} + \frac{U_x(x)}{2\pi V_\infty} \frac{S'(x)}{r(\theta)}$$

(Continued on next page)

(26)  
(Conc.)

$$\frac{u_\theta}{V_\infty}(r, \theta) = - \sum_{n=1}^{MH} \frac{na_n \sin n\theta}{r^{n+1}(\theta)}$$

Substitute equation (26) into (24). Using this result and equation (23), with  $V(x)$  equal to zero, the flow tangency condition given by equation (18) becomes

$$\begin{aligned} \left[ U_x(x) + u_x(x, v, \tau) \right] \frac{dv(\theta)}{dx} = W(x) \cos\left(m - \frac{\pi}{2}\right) + V_\infty \left[ \frac{U_x(x)}{2\pi V_\infty} \frac{S'(x)}{r(\theta)} \right. \\ \left. - \sum_{n=1}^{MH} \frac{na_n \cos n\theta}{r^{n+1}(\theta)} \right] \cos\left[\theta - \left(m - \frac{\pi}{2}\right)\right] \\ + V_\infty \sum_{n=1}^{MH} \frac{na_n \sin n\theta}{r^{n+1}(\theta)} \sin\left[\theta - \left(m - \frac{\pi}{2}\right)\right] \end{aligned} \quad (27)$$

This is the nonlinear form of the flow tangency condition expressed in velocity components in both polar and rectangular coordinate systems. The perturbation term  $u_x(x, v, \tau)$  will be omitted from here on since it is small compared to  $U_x(x)$ . With this simplification and after dividing by  $V_\infty$ , the flow tangency condition is given by

$$\begin{aligned} \frac{U_x(x)}{V_\infty} \frac{dv(\theta)}{dx} = \frac{W(x)}{V_\infty} \cos\left(m - \frac{\pi}{2}\right) + \left[ \frac{U_x(x)}{2\pi V_\infty} \frac{S'(x)}{r(\theta)} - \sum_{n=1}^{MH} \frac{na_n \cos n\theta}{r^{n+1}(\theta)} \right] \cos\left[\theta - \left(m - \frac{\pi}{2}\right)\right] \\ + \sum_{n=1}^{MH} \frac{na_n \sin n\theta}{r^{n+1}(\theta)} \sin\left[\theta - \left(m - \frac{\pi}{2}\right)\right] \end{aligned} \quad (28)$$

As already mentioned in the discussion pertaining to the choice of potential, MH is the number of polar harmonics.

The rate of change with  $x$  of the body cross-sectional area,  $S'(x)$ , is also used in the determination of the outer or axisymmetric potential  $\phi_e$ . In terms of the equivalent body radius  $R_{eq}$ , the source term in equation (28) may be rewritten as follows:

$$\frac{U_x(x)}{2\pi V_\infty} \frac{S'(x)}{r(\theta)} = \frac{U_x(x)}{2\pi V_\infty} \frac{1}{r(\theta)} \frac{d}{dx} (\pi R_{eq}^2) = \frac{U_x(x)}{V_\infty r(\theta)} R_{eq} \frac{dR_{eq}}{dx} \quad (29)$$

The flow tangency condition is applied at control points on the body contour as explained previously in the section concerning the choice of potentials. Let MC be the number of control points over the half range of  $\theta$  from  $0^\circ$  to  $180^\circ$ . The result is a set of MC flow tangency equations in MH unknown polar harmonic coefficients  $a_n$ . This set of equations will be solved in the least-square sense and regardless of the other factors discussed later that may influence the choice of the number of polar harmonics and control points, the following requirements holds.

$$MH \leq MC \quad (30)$$

#### 2.2.5 Solution of the simultaneous equations

The method of solution will now be discussed. Equation (28) is re-written by transposing and factoring terms and is applied at MC control points yielding the following set of equations.

$$\sum_{n=1}^{MH} \left[ \frac{na_n}{r^{n+1}(\theta_i)} \left\{ -\cos n\theta_i \cos \left[ \theta_i - \left( m_i - \frac{\pi}{2} \right) \right] + \sin n\theta_i \sin \left[ \theta_i - \left( m_i - \frac{\pi}{2} \right) \right] \right\} \right] \\ = \frac{U_x(x)}{V_\infty} \frac{dv(\theta_i)}{dx} - \frac{W(x)}{V_\infty} \cos \left( m_i - \frac{\pi}{2} \right) - \frac{U_x(x)}{2\pi V_\infty} \frac{S'(x)}{r(\theta_i)} \cos \left[ \theta_i - \left( m_i - \frac{\pi}{2} \right) \right] \quad (31)$$

$$i = 1, 2, \dots, MC$$

The objective is to find the best possible values for a set of unknowns  $a_1, a_2, \dots, a_{MH}$  for a set of MC linear equations. As an alternative to the exact solution that exists when  $MH = MC$ , the set of MC equations will be satisfied in the least-square sense; that is, minimize the quantity

$$E = \sum_{i=1}^{MC} \delta_i^2 \quad (32)$$

where

$$\delta_i = \sum_{n=1}^{MH} \left[ \frac{na_n}{r^{n+1}(\theta_i)} \left\{ -\cos n\theta_i \cos \left[ \theta_i - \left( m_i - \frac{\pi}{2} \right) \right] + \sin n\theta_i \sin \left[ \theta_i - \left( m_i - \frac{\pi}{2} \right) \right] \right\} \right] \\ - \frac{U_x(x)}{V_\infty} \frac{dv(\theta_i)}{dx} + \frac{W(x)}{V_\infty} \cos \left( m_i - \frac{\pi}{2} \right) + \frac{U_x(x)}{2\pi V_\infty} \frac{S'(x)}{r(\theta_i)} \cos \left[ \theta_i - \left( m_i - \frac{\pi}{2} \right) \right] \quad (33)$$

Following the procedure indicated in reference 7, in order to minimize E, equate to zero the partial derivatives

$$\frac{\partial E}{\partial a_1}, \frac{\partial E}{\partial a_2}, \dots, \frac{\partial E}{\partial a_{MH}} \quad (34)$$

Letting

$$\psi_i = \theta_i - m_i + \frac{\pi}{2} \quad (35)$$

and performing the indicated differentiations leads to the following result:

$$\sum_{i=1}^{MC} \left[ \left\{ \sum_{j=1}^{MH} \frac{ja_j}{r^{j+1}(\theta_i)} (-\cos j\theta_i \cos \psi_i + \sin j\theta_i \sin \psi_i) \right\} \frac{n}{r^{n+1}(\theta_i)} \right. \\ \left. \cdot (-\cos n\theta_i \cos \psi_i + \sin n\theta_i \sin \psi_i) \right] + \sum_{i=1}^{MC} \left[ -\frac{U_x(x)}{V_\infty} \frac{dv(\theta_i)}{dx} + \frac{W(x)}{V_\infty} \cos \left( m_i - \frac{\pi}{2} \right) \right. \\ \left. + \frac{U_x(x)}{2\pi V_\infty} \frac{S'(x)}{r(\theta_i)} \cos \psi_i \right] \frac{n}{r^{n+1}(\theta_i)} (-\cos n\theta_i \cos \psi_i + \sin n\theta_i \sin \psi_i) = 0 \quad (36)$$

$$n = 1, 2, \dots, MH$$

Interchanging the summation signs and transposing the "forcing" terms to the right-hand side gives

$$\sum_{j=1}^{MH} \left[ ja_j \sum_{i=1}^{MC} \frac{-\cos j\theta_i \cos \psi_i + \sin j\theta_i \sin \psi_i}{r^{j+1}(\theta_i)} \frac{n}{r^{n+1}(\theta_i)} (-\cos n\theta_i \cos \psi_i \right. \\ \left. + \sin n\theta_i \sin \psi_i) \right] = \sum_{i=1}^{MC} \left[ -\frac{U_x(x)}{V_\infty} \frac{dv(\theta_i)}{dx} + \frac{W(x)}{V_\infty} \cos \left( m_i - \frac{\pi}{2} \right) + \frac{U_x(x)}{2\pi V_\infty} \frac{S'(x)}{r(\theta_i)} \cos \psi_i \right] \frac{n}{r^{n+1}(\theta_i)} \quad (36)$$

(Continued on next page)

$$+ \sin n\theta_i \sin \psi_i) \Big] - \sum_{i=1}^{MC} \left[ \frac{U_x(x)}{V_\infty} \frac{dv(\theta_i)}{dx} - \frac{W(x)}{V_\infty} \cos(m_i - \frac{\pi}{2}) \right. \\ \left. - \frac{U_x(x)}{2\pi V_\infty} \frac{S'(x)}{r(\theta_i)} \cos \psi_i \right] \frac{n}{r^{n+1}(\theta_i)} (-\cos n\theta_i \cos \psi_i + \sin n\theta_i \sin \psi_i) \quad (37)$$

$$n = 1, 2, \dots, MH$$

The final result is a set of MH equations in unknowns  $a_1, a_2, \dots, a_{MH}$  to be solved simultaneously. The number of control points MC and the number of polar harmonics MH must be specified and are subject to equation (30). The determination of these two numbers from the point of view of accuracy and economy of computation may require a good amount of judgment and this will be the topic of the following discussion.

#### 2.2.6 Selection of number of control points and number of polar harmonics

For a given body cross-sectional shape, MC and MH cannot be arbitrarily chosen. They must at least satisfy the condition indicated in equation (30). The set of simultaneous equations given by equation (37) produces a solution for any combination of MC and MH subject only to the restriction of equation (30). The solution, when applied to the degenerate case of a body with a circular cross section, can be pushed to the limit, that is MC equal MH. The exact result is the expected doublet solution. All polar harmonic coefficients except the first are zero for this case and convergence problems of any kind do not exist.

In general, the success or validity of the solution depends on the extent to which the Laplace equation is valid in the crossflow plane. The potential  $\phi_2$  given by equation (6) satisfies Laplace's equation but the usual slender-body assumptions apply. The principles are laid out in references 4 and 8. The occurrence of sharp corners on the body cross section tends to make the solution locally invalid and influences the selection of the number of harmonics. However, by "softening" up on the solution by means of the least-squares method, solutions can still be obtained with some sacrifice in accuracy near the corners. In the following examples, a general procedure for determining the number of control points and harmonics will be given.

Consider the two body contours shown in figure 3. The upper contour, body contour A, has one  $90^\circ$  corner and the lower contour, body contour B, has three  $90^\circ$  corners over the  $\theta$  range from  $0^\circ$  to  $180^\circ$ . For  $6^\circ$  angle of attack, calculations were performed for both contours to determine the perturbation upwash and sidewash at the indicated field points as a function of the number of polar harmonics MH for given numbers of control points MC. This is a pure incidence problem since the contours are not changing with axial position. The selected field points are in fact members of the first chordwise row of wing control points at which the flow tangency condition must be satisfied. The spanwise locations of the points is determined by the wing-fuselage interference scheme described in a later section. The results are shown in figures 4(a) and 4(b) for body contour A and in figures 5(a) and 5(b) for body contour B. The perturbation velocities  $v$  and  $w$  are positive in the  $y$  and  $z$  directions, respectively, shown in figure 3 and are the sums of the perturbation velocities induced by the equivalent body of revolution and the two-dimensional polar harmonics. The effects of the two-dimensional source terms appearing in the complete potential, equation (5), and the two-dimensional potential, equation (6), cancel each other.

The number of control points MC varied from 16 to 64. For each number of control points, successive calculations were performed for different and increasing numbers of polar harmonics MH until the solution "blew up." The solution is considered "blown up" or beyond the range of validity when the induced perturbation velocities from the solution are observed to diverge from the established trend. This observation is not always readily apparent. An additional indication of the validity of the solution is given by the series of the polar harmonic coefficients. They must show convergence trends.

Refer now to figures 4(a), 4(b), and 6, which pertain to body contour A. Consider the case with 24 control points. Increasing MH has very little effect on either velocity component until MH reaches 23. For this number of harmonics both components show large deviations and the associated polar harmonic coefficients listed in figure 6 indicate a diverging trend as compared with the set shown for MH equal to 16. The same type of observations can be made for the other numbers of control points. The number of polar harmonics can be increased as the number of control points is increased. The conclusion can be drawn that for a body

contour with one  $90^\circ$  corner, such as body contour A, a solution with  $MC = MH$  can still be obtained but the flow velocities observed at the field point and the polar harmonic coefficients show diverging trends. This is because the solution is forced to go through all control points and the solution tends to become singular near the sharp corner. However, solutions with harmonic coefficients showing convergence trends can be generated for a variety of  $MC$  and  $MH$  combinations as long as  $MH$  does not exceed the integer nearest  $0.9 MC$ .

A more difficult case is offered by body contour B. Similar results to those just presented for contour A are shown in figures 5(a), 5(b), and 7. The field point chosen for this case lies on a sharp corner, see figure 3(b). A nonsingular solution can never be obtained at this point. But, since this point may be a member of the first chordwise row of wing control points, it is important to investigate the behavior of the method here. It will be shown that solutions can be generated with seemingly converging sets of polar harmonic coefficients for combinations of  $MH$  and  $MC$  with  $MH \leq 0.9 MC$ . For 16 control points, both velocity components diverge at 13 polar harmonics. As the number of control points is increased, the upwash does not afford conclusive evidence as to the maximum allowable number of polar harmonics. The sidewash, however, shows some signs of diverging. For the case of 32 control points, gradual dropping off sets in at 18 polar harmonics. The case of 48 control points indicates divergence starts above 26 harmonics. Calculations performed for all numbers of control points  $MC$  do not indicate sets of polar harmonic coefficients with diverging trends until  $MH$  equals the integer nearest  $0.9 MC$ . This behavior is the same as for the simpler contour A. If the maximum value reached by the sidewash is used as a criteria, then a safe choice would be 32 control points and 14 harmonics. The associated series of polar harmonic coefficients is shown in figure 7 together with the series for 30 harmonics. The latter shows strongly diverging trends. These results indicate the desirability of locating the wing control points off the singularity. However, if it is located there, no great overall loss of accuracy should result provided  $MH$  is much less than  $MC$ .

Another factor entering into the specification of  $MC$  and  $MH$  is the calculation time required by that part of the program dealing with body flow modeling. This time increases sharply with the number of polar

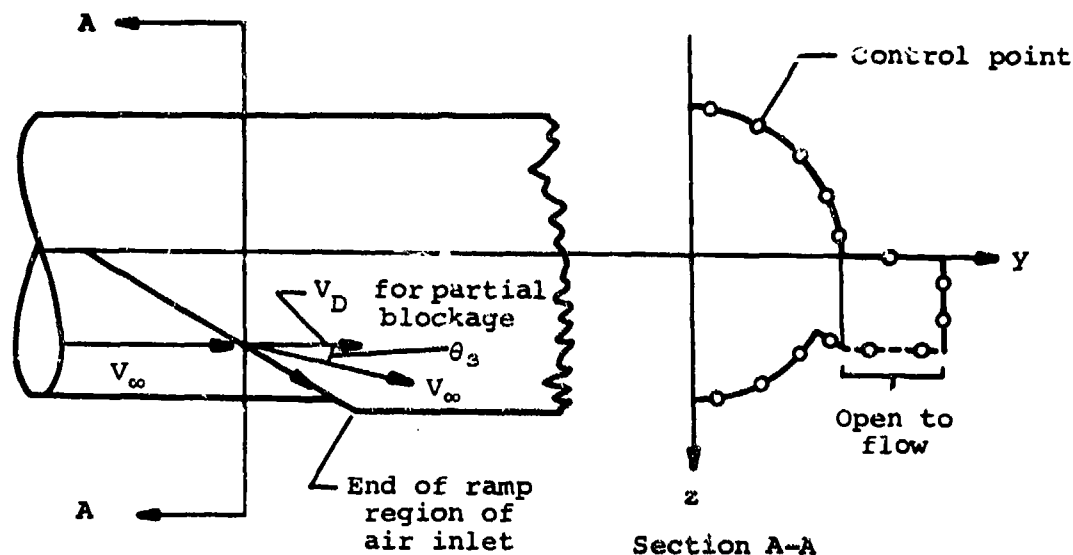


harmonics for a given number of control points. The time increases less severely with increasing number of control points.

Bodies with smoothly varying curvature in the longitudinal direction and on the contour in the crossflow plane should not show any of the problems associated with the body contours just examined.

### 2.3 Fuselage Mounted Air Inlets

The air inlets, which, as referred to here, include the entire region from the mouth back to the engine exhaust, are treated as part of the fuselage. In crossflow planes in which the contour of the inlet is a solid boundary, such as downstream of the ramp shown in the following sketch, the polar harmonics are determined as described in section 2.2



using the appropriate cross-sectional area distribution as will be discussed subsequently.

In a region where the contour is not a solid boundary, as is the case in the sketch in the ramp region where there is no lower surface so that it is open to the flow, the body slope boundary condition used in the polar harmonic calculation is determined in a slightly different manner. The inlet is first considered to have a solid boundary. Control points are laid out on the half range  $0^\circ \leq \theta \leq 180^\circ$ , of the crossflow contour. With each control point there will be associated a streamwise

body slope and upwash if angle of attack is considered. The streamwise body slopes are calculated on the basis of body radii at consecutive axial stations as described in a previous section. For the control points lying on the part of the crossflow contour which is not a solid boundary, the streamwise slopes  $\theta_3$  depend on the inlet to free-stream velocity ratio. For a velocity ratio of unity, streamlines are parallel to the axis of the inlet, and for lesser values they point downward for the air inlet shown in the sketch.

Designate the ratio  $V_D/V_\infty$  as the air inlet velocity ratio due to blockage to the flow in the air inlet. To account for the change in streamline direction caused by the blockage, the streamwise slopes calculated for the solid boundary are modified to give slopes  $\theta_3$  as follows.

$$\theta_3 = \left(1 - \frac{V_D}{V_\infty}\right) \frac{dv(\theta)}{dx} \Big|_{\text{solid boundary}} \quad (38)$$

The streamwise body slope  $dv(\theta)/dx$  that appears in the flow tangency condition, equation (28), is replaced by slopes  $\theta_3$  given by the above expression. Before the solution can proceed, however, the rate of change of cross-sectional area,  $S'(x)$ , must be determined. For an inlet velocity ratio of zero, the entire cross-sectional area of the inlets is added to the cross-sectional area of the fuselage. For an inlet velocity ratio of one half, only one half of the inlet cross-sectional area is added to the fuselage area, and so on. In this way, the area distribution is adjusted to reflect the inlet velocity ratio. The polar harmonic coefficients can now be solved for, following the methods described in the previous sections, and the inner or crossflow potential  $\phi_2(r, \theta)$  in equation (6) is determined.

The outer or axisymmetric potential  $\phi_e$  is also adjusted to reflect the inlet velocity ratio. Its cross-sectional area distribution is modified exactly as described in the previous paragraph and the axisymmetric solution is determined using the methods of reference 3. The solution for the entire flow field is again given by equation (5).

#### 2.4 Wing-Pylon Flow Model

The wing-pylon flow model used in the present work is a modification of that used in the work of reference 1. This modification together with the inclusion of fuselage angle-of-attack effects in the potential flow

model for the fuselage, both circular and noncircular, accounts for nearly all of the wing-fuselage interference. In the earlier work, fuselage angle-of-attack effects were not included and the wing panels over which the vortex lattice was laid out extended to the fuselage vertical plane of symmetry. In the method adopted here, the fuselage is first represented by the potential flow methods described previously. Then the influence of the fuselage on the exposed wing panels is determined. A vortex lattice with unknown vortex strengths is laid out on the exposed wing panels and pylon and an image vortex lattice of the wing is constructed inside the fuselage. The wing-pylon loading is computed in terms of the vortex strengths with the inclusion of the fuselage influence on the exposed wing panels and pylon. The inclusion of the image vortices inside the fuselage approximately satisfies the condition of no flow through the surface and thus accounts for nearly all of the wing-fuselage interference. A second iteration would be to allow the wing and pylon to induce velocities on the fuselage and then determine a new singularity distribution for the fuselage. This singularity distribution would then be used to determine a new wing-pylon vorticity distribution. This iteration is considered a second-order effect and is not performed.

#### 2.4.1 Vortex-lattice model with imaging to account for wing-fuselage interference

This discussion will describe the modifications made to the horseshoe vortex-lattice approach described in reference 1 to account for wing-fuselage interference.

The wing-vortex layout is altered so that it does not go through the fuselage. Only the portion of the wing outside the circular fuselage or the equivalent body of revolution for the noncircular fuselage is covered with a vortex lattice using the methods of reference 1. If the body of revolution radius varies over the region of influence of the wing, an average radius can be used. In practice the maximum radius is used. Each horseshoe vortex that is outside the body of revolution is then imaged inside. In this way, velocities normal to the equivalent body are exactly zero in the wing chordal plane and they are very small at all other locations on the body of revolution surface near the wing-body junction. For noncircular bodies the actual fuselage surface is generally close to the equivalent body surface so that to a good approximation the same conditions hold for the actual fuselage surface.

The crossflow plane theory for the imaging scheme is described in reference 9 and extended to three dimensions. With this approach, the semi-infinite lengths of the vortex-trailing legs are located at their image locations inside the body of revolution. For a filament located at radial distance  $r_{v_1}$  from the body centerline, the image is located at radial distance  $r_{iv_1}$  as shown in figure 8. Distance  $r_{iv_1}$  is given by

$$r_{iv_1} = \frac{a^2}{r_{v_1}} \quad (39)$$

where  $a$  is the maximum radius of the equivalent or circular body. The imaged semi-infinite filament runs parallel to all the exterior filaments. By constructing the images of the two trailing legs belonging to an exterior horseshoe vortex and connecting the beginnings of the imaged filaments, the image of a horseshoe vortex bound leg is formed. The vortex strength of the image horseshoe vortex is equal to the strength of the associated exterior horseshoe vortex on the wing panel.

$$\Gamma_{iv} = \Gamma_v \quad (40)$$

Figure 8 also shows the positive sense of the circulation of the vortex-trailing legs on the wing and their images. Strictly speaking, each filament on the wing also leads to a filament with the same circulation direction at the center of the equivalent body. Because of symmetry about the  $x$ - $z$  plane, however, the net circulation at the center is zero.

Figure 8 shows the projection of the exterior and image horseshoe vortex in elevation and figure 9 projects the exterior and image horseshoe vortex in planform. The bound-leg midpoint coordinates of the image vortex must be expressed in terms of the associated exterior vortex bound-leg quantities in the wing coordinate system. The origin of the wing coordinate system is at a different position in the fuselage  $x, y, z$  system than was used in the work of reference 1. It is still in the  $y = 0$  plane but the  $x$  and  $z$  coordinates are now the intersection of the wing leading edge with the circular or equivalent body surface as shown in figures 8 and 9. In laying out the image vortex system the directions of the wing coordinates  $(x_w, y_w, z_w)$  are assumed parallel to the fuselage coordinates  $(x, y, z)$ . Thus, wing incidence relative to the fuselage is ignored.

From figure 8 the following relationships hold

$$\left. \begin{aligned} \theta_1 &= \tan^{-1} \frac{z_{v_1,w} + z_o}{y_{v_1,w}} \\ \theta_2 &= \tan^{-1} \frac{z_{v_2,w} + z_o}{y_{v_2,w}} \\ \theta_3 &= \theta_2 - \theta_1 \end{aligned} \right\} \quad (41)$$

where subscripts  $v_1$  and  $v_2$  denote the right and left trailing legs, respectively, of a horseshoe vortex located on the left wing panel and  $z_o$  is the  $z$  coordinate measured in the fuselage system of the origin of the wing coordinate system. The radial distances of the vortex-trailing legs from the fuselage centerline are

$$\left. \begin{aligned} r_{v_1} &= [y_{v_1,w}^2 + (z_{v_1,w} + z_o)^2]^{1/2} \\ r_{v_2} &= [y_{v_2,w}^2 + (z_{v_2,w} + z_o)^2]^{1/2} \end{aligned} \right\} \quad (42)$$

From equations (39), (41), and (42) the coordinates of the image bound-leg midpoint expressed in the wing coordinate system are given by

$$\left. \begin{aligned} x_{iv,w} &= x_{v,w} \\ y_{iv,w} &= - \frac{\frac{a^2}{r_{v_1}} \cos \theta_1 + \frac{a^2}{r_{v_2}} \cos \theta_2}{2} \\ z_{iv,w} &= - \frac{\frac{a^2}{r_{v_1}} \sin \theta_1 + \frac{a^2}{r_{v_2}} \sin \theta_2}{2} - z_o \end{aligned} \right\} \quad (43)$$

To fully specify the image horseshoe vortex, the dihedral and sweep angles and span must also be specified. Referring to figure 10 which is an enlargement of the image vortex region of figure 8, the following

relationships are established. The span  $2s_{iv}$  of the image horseshoe vortex is expressed as

$$(2s_{iv})^2 = \left(\frac{a^2}{r_{v_2}}\right)^2 + \left(\frac{a^2}{r_{v_1}}\right)^2 - 2 \frac{a^2}{r_{v_2}} \frac{a^2}{r_{v_1}} \cos \theta_3 \quad (44)$$

and the angle  $\theta_4$  shown in figure 10 is given by

$$\theta_4 = \sin^{-1} \left[ \frac{a^2}{r_{v_2}} \frac{\sin \theta_3}{2s_{iv}} \right] \quad (45)$$

The dihedral  $\phi_{iv}$  of the image horseshoe vortex is as follows.

$$\left. \begin{aligned} \phi_{iv} &= -(\theta_4 - \theta_1) \\ \phi_{iv} < -\frac{\pi}{2}, \phi_{iv} &= \phi_{iv} + \pi; \phi_{iv} > \frac{\pi}{2}, \phi_{iv} &= \phi_{iv} - \pi \end{aligned} \right\} \quad (46)$$

The sweep angle  $\psi_{iv}$  of the image bound leg measured in the planform plane is shown in figure 9 and is determined from

$$\tan \psi_{iv} = - \frac{(y_{v_2,w} - y_{v_1,w}) \tan \psi_v}{(y_{iv_1,w} - y_{iv_2,w})} \quad (47)$$

and when transformed into the wing chordal plane

$$\tan \psi_{iv} \Big|_{\text{chordal plane}} = \tan \psi_{iv} \Big|_{\text{planform}} \cos \phi_{iv} \quad (48)$$

The image horseshoe vortex is now fully specified in terms of the coordinates of its bound-leg midpoint, the bound-leg sweep angle, dihedral angle, and the horseshoe vortex span given by equations (43), (48), (46) and (44) respectively. The wing loading can now be determined.

The vortex lattice is laid out on the exposed wing panels and pylons following the procedure described in section 4.2.2 of reference 1. The wing image vortex lattice is established inside the equivalent body representing the fuselage using the methods described above. Note that the pylon vortices are not imaged. The vortex strength of each imaged horseshoe vortex is equal to the strength of the associated exterior horseshoe vortex, equation (40). Thus, the flow tangency condition applied at the

wing control points as described in reference 1 must be expanded to reflect the influence of the image horseshoe vortices. Specifically, equations (6) and (7) on pages 10 and 11 of reference 1 are rewritten as follows. With  $M$  control points on the left wing panel exterior to the equivalent body and  $MP$  on the left pylon, the boundary condition on the left wing panel is given by

$$\begin{aligned} \sum_{n=1}^M \frac{\Gamma_n}{4\pi V_\infty} \left[ (F_{w_{v,n}} + F_{iw_{v,n}}) \cos \phi_v - (F_{v_{v,n}} + F_{iv_{v,n}}) \sin \phi_v \right] \\ + \sum_{n=M+1}^{M+MP} \frac{\Gamma_n}{4\pi V_\infty} (F_{w_{v,n}} \cos \phi_v - F_{v_{v,n}} \sin \phi_v) \\ = (\alpha + \alpha_{\ell_v}) \cos \phi_v + \frac{v_{i,v}}{V_\infty} \sin \phi_v - \left( \frac{u_{i,v}}{V_\infty} \alpha_{\ell_v} + \frac{w_{i,v}}{V_\infty} \right) \cos \phi_v \end{aligned} \quad (49)$$

$$v = 1, 2, \dots, M$$

With the camberless pylon at zero incidence, the pylon boundary condition is written for  $MP$  control points as

$$- \sum_{n=1}^M \frac{\Gamma_n}{4\pi V_\infty} (F_{v_{v,n}} + F_{iv_{v,n}}) - \sum_{n=M+1}^{M+MP} \frac{\Gamma_n}{4\pi V_\infty} F_{v_{v,n}} = \frac{v_{i,v}}{V_\infty} \quad (50)$$

$$v = M+1, M+2, \dots, M+MP$$

All terms are fully described in reference 1 except for the added influence functions  $F_{iw}$  and  $F_{iv}$ . These functions relate the perturbation velocity components, induced at some point by a wing image horseshoe vortex, to its circulation and the coordinates of the point relative to the bound-leg midpoint of the image horseshoe vortex. Using the Biot-Savart law, see reference 10, the perturbation velocities induced at a point by an image horseshoe vortex are then

$$\left. \begin{aligned} u(x,y,z) &= \frac{\Gamma}{4\pi V_\infty} F_{iu}(x,y,z,s_{iv},\psi_{iv},\phi_{iv}) \\ v(x,y,z) &= \frac{\Gamma}{4\pi V_\infty} F_{iv}(x,y,z,s_{iv},\psi_{iv},\phi_{iv}) \\ w(x,y,z) &= \frac{\Gamma}{2\pi V_\infty} F_{iw}(x,y,z,s_{iv},\psi_{iv},\phi_{iv}) \end{aligned} \right\} \quad (51)$$

The influence functions depend only upon the coordinates  $(x,y,z)$  of the point at which the velocity is to be computed relative to the image horseshoe vortex, and the image vortex semispan  $s_{iv}$ , bound-leg sweep angle  $\psi_{iv}$ , and dihedral angle,  $\phi_{iv}$ . The analytical expressions for the above influence functions are identical to equations (10), (11) and (12) in reference 1. They also are subject to equation (13) of that reference to account for the images of the horseshoe vortices laid out on the right wing panel.

Equations (49) and (50) represent a set of  $M+MP$  simultaneous equations in which the unknowns are the  $M+MP$  values of circulation strength  $\Gamma$ . Therefore, the values can be obtained through a matrix solution for a given angle of attack, twist and camber distribution, and a specified set of externally induced perturbation velocities  $u_i/V_\infty$ ,  $v_i/V_\infty$ , and  $w_i/V_\infty$  caused by wing and pylon thickness effects and from other aircraft components such as fuselage, rack and stores. The addition of the images does not increase the number of unknowns. When calculating flow fields at specified field points, the influence of the image horseshoe vortex system must be added to the influence of the horseshoe vortices located on the exposed wing panels.

#### 2.4.2 Thickness model

The three-dimensional source panel method used in reference 1 to account for wing and pylon thickness has been unaltered except for the fact that the wing thickness strips are now only laid out on the exposed wing panels. The equations presented in section 4.2.3 of reference 1 can be used directly even though a new wing coordinate system origin was introduced in connection with the new vortex-lattice model. The wing thickness strips are not imaged inside the fuselage. This refinement could be added and would improve the accuracy in accounting for wing-fuselage interference. This



same comment can be made with regard to imaging the pylon thickness strips and vortex lattice.

## 2.5 Store and Rack Flow Models

The flow models for all stores present on the aircraft and an ejector rack, if one is present, have not been changed from those described in reference 1. These models were discussed in sections 4.1 and 4.3, respectively, of that reference.

## 3. FORCE AND MOMENT CALCULATION

The methods and equations used to calculate the aerodynamic forces and moments acting on the separated store at each point in its trajectory are unchanged from those presented in section 5 of reference 1. The only change to the discussion presented there is with regard to the calculation of the perturbation velocity field.

The second term in the three expressions of equation (29) of reference 1 is the perturbation velocity term. This is comprised of the perturbation velocities induced by the fuselage, wing, pylon, rack and other stores and is calculated by the methods presented in section 4 of reference 1 or section 2 of this report. It is to be remembered that these methods apply to the equivalent incompressible configuration. At each point in the trajectory the points at which the velocities are required must be located in the incompressible space. The perturbation velocities produced by a circular fuselage are calculated using equations (4) and (5) of reference 1 for the volume effects and equation (4) of this report for the angle-of-attack effects. For a noncircular fuselage the complete potential is given by equation (5) of this report. The perturbation velocities associated with the equivalent body potential  $\phi_e$  are also given by equations (4) and (5) of reference 1. The perturbation velocities associated with potential  $\phi_2$  are given by equation (26) of this report. The perturbation velocity produced by the last term of equation (5) is equal and opposite in sign to the last term in the  $u_r/V_\infty$  expression of equation (25). The perturbation velocities induced by the rack and store volumes are also calculated using equations (4) and (5) of reference 1. Those induced by the wing-pylon vortex lattice are determined by equation (8) of that reference by summing over all vortices, including the image wing vortices. The velocities induced by the wing and pylon thickness

distribution are obtained from equations (19) and (25) by summing over all thickness strips. The velocities calculated using these equations are in the coordinate system of each aircraft component. Prior to transforming these back to the compressible space they must be summed up in the fuselage coordinate system since this is the coordinate system in which the compressibility correction was applied.

On page 25 of reference 1 a discussion of the velocity field calculation for the special case of a store released from under the fuselage centerline is presented. This case was handled differently from that where the store is under the wing. With the new fuselage flow models and the new vortex-lattice model described in this report which account for wing-fuselage interference, this special treatment is no longer required. The method of calculating the perturbation velocity field is now independent of store position.

#### 4. CALCULATION OF STORE TRAJECTORIES

The method of calculating store trajectories described in section 6 of reference 1 has not been changed. The equations of motion are discussed in section 6.1 and derived in Appendix II of that report. The computer program is described in section 6.2. This description is still applicable with the exception of the brief discussion of the fuselage input data.

The computer program now contains two fuselage options. These options are a circular cross-section fuselage and a noncircular cross-section fuselage. The index which is read in to indicate whether or not a fuselage is present further indicates which option is to be used.

The input data for the circular fuselage option consist of the length, maximum radius, source distribution, and series of segmented polynomials specifying the fuselage shape. These polynomials are the ones which were used in calculating the source distribution.

The first input data for the noncircular fuselage option are the length, maximum radius of the equivalent body of revolution, and source distribution for this body. The remainder of the input data are required to perform the crossflow-plane polar-harmonic calculation described in section 2.2. The number of stations at which the calculation is to be performed is specified as is the number of control points to be used and the inlet to free-stream velocity ratio if inlets are present. For each

crossflow plane the number of polar harmonics is specified. This number may change from station to station. Data defining the actual crossflow plane contour of the fuselage including inlets are input in tabular form.

## 5. COMPARISONS WITH EXPERIMENTAL DATA

This section of the report will present comparisons with experimental data in order to assess the accuracy of the flow models presented in section 2 for the circular and noncircular fuselages and the wing-pylon vortex-lattice model with the wing vortices imaged inside the fuselage. Comparisons will be made with flow-field data, store body load distributions, and store body forces and moments. Store trajectory comparisons will also be made.

### 5.1 Wind-Tunnel Model Description

In order to provide systematic data with which the theory could be tested, a wind-tunnel test program was conducted in the 4T wind tunnel at Arnold Engineering Development Center. The basic model used in the tests was used in the work of reference 1. This model is shown in figure 11. For the present tests this model was modified so that additional components could be attached. This modified model is shown in figure 12. Figure 12(a) shows canopy  $C_1$  attached to the uncambered nose  $N_1$ . Figures 12(b) and 12(c) show other components attached to the basic wing-fuselage combination. The wing is designated  $W$  and the fuselage  $B_2$ . Two components are shown which can be attached to  $B_2$ . They are the non-circular addition  $A_1$  and the duct assembly  $A_2D$ . This assembly consists of a piece identical to  $A_1$  and two rectangular ducts located on either side of the fuselage (the right one is not shown in the figure). An assembly was located downstream of the end of the ducts which allowed plugs to be positioned in various locations relative to the duct exit. In this way the inlet to free-stream velocity ratio could be varied. Static and total pressure measurements were taken in the ducts and used to determine the air inlet velocity ratio.

In addition to the models shown, a wingless circular fuselage  $B_1$  was constructed. The noncircular addition  $A_1$  could be attached to this body. A cambered nose was also constructed. It is the same length as nose  $N_1$  and has the same area distribution. The camber line is a circular arc. The tip of the nose lies on a line tangent to the bottom of

the cylindrical body and the camber line is tangent to the longitudinal axis of the cylinder at the nose base.

The store used in the test program is shown in figure 13. The model used to measure the load distributions does not have the cruciform tail fins and has 19 pressure orifices equally spaced over the length of the body. By rolling the model through  $360^\circ$  a complete pressure distribution was obtained. The load distribution was determined by numerically integrating the pressures. The store used in the force and moment tests also did not have the cruciform fins. The trajectory data to be shown was obtained using the finned store. In addition, the pylon shown in figures 12(b) and 12(c) was present. The pylon designation is  $P_{1/3}$ .

Comparisons will be presented using all components of the model just described with the exception of the canopy and the cambered nose. They produced no effect on the flow field behind the base of the nose. The method presented in section 2.2 for modeling noncircular fuselages is nevertheless applicable to components of this type.

## 5.2 Flow Fields

The new features of the flow-field prediction method include the addition of the capability to handle noncircular fuselages with and without air inlets as well as vortex-lattice imaging to account for wing-fuselage interference. To illustrate the application of the method to a noncircular fuselage, a crossflow velocity vector plot is shown in figure 14. The wind-tunnel model is the original circular fuselage with the noncircular addition attached. The wing is not present and the fuselage angle of attack is  $6^\circ$ . As a reference velocity vector, the component of the free stream in the crossflow plane is also shown in the figure. Agreement is quite good except very close to the sharp lower corner. For cross-sectional shapes without sharp corners, the agreement should be improved.

Figure 15 shows comparisons for two angles of attack between theory and experiment for axial upwash distributions under the fuselage centerline for the circular fuselage  $N_1B_1$  with and without the noncircular addition  $A_1$ . There is a large measured effect of the noncircular addition in the region where it develops which is well predicted by the theory at both angles of attack. A line indicating the change in velocity equivalent to  $1^\circ$  of flow angle is shown on the figure. The sketch of the fuselage at the top of the figure is in its proper longitudinal location relative to the data.

Figure 16 shows a crossflow plane velocity vector plot for the same fuselage model as figure 14 but with the wing attached. The angle of attack is  $6^\circ$ . The results predicted by the theory agree well with the experimental data thereby illustrating the validity of the wing-fuselage interference method. In both figures 14 and 16, the axial location is aft of the ramp region of the noncircular addition.

Distributions of upwash  $w_B/V_\infty$  under the fuselage centerline for the various stages of the wind-tunnel model buildup and various inlet velocity ratios are plotted in figure 17. The angle of attack is  $6^\circ$ . Figure 17(a) shows the effect of model buildup. The three models are circular body with wing  $N_1B_2W$ , circular body with wing and noncircular addition  $N_1B_2WA_1$ , and circular body with wing and duct assembly  $N_1B_2WA_2D$ . For the latter configuration the ratio of the inlet or duct velocity to the free-stream velocity,  $V_D/V_\infty$ , is 1.0.

Compared with the data associated with the circular fuselage configuration, the effects of adding the noncircular addition and duct assembly are seen to be most pronounced near the end of the ramp region. In general the trends are indicated by the theory. The magnitudes of the changes in upwash are predicted only in part.

Figure 17(b) shows the effect of air inlet velocity ratio on the upwash distribution. The effect of reducing the air inlet velocity ratio is to increase the downwash very strongly near the end of the ramp region. The theory predicts this effect partially. Just downstream of the ramp region slight flow separation may have occurred. The effect of this would be to increase the downwash.

Figure 18 presents similar results, as those presented in figure 17, for an angle of attack of  $0^\circ$ . The data indicate the same effects as observed for  $6^\circ$  angle of attack. The theory again predicts the trends but not all of the magnitudes of the changes. In general the theory is in better agreement with the data at  $\alpha = 0^\circ$  than at  $\alpha = 6^\circ$ . Thus, it appears an angle-of-attack effect is occurring which is not accounted for by the theory. This checks the separation hypothesis advanced above for  $\alpha = 6^\circ$ . The extent of separation would increase with angle of attack. This separation effect is Reynolds number dependent which will be discussed later.

Upwash  $W_s/V_{\infty_s}$  and sidewash  $V_s/V_{\infty_s}$  are shown in figures 19(a) and 19(b) for the region the store centerline would occupy if the store was in the position shown in figures 12(b) and 12(c). The angle of attack is  $6^\circ$  and the pylon is not present. The  $x_s, y_s, z_s$  coordinate system is shown in figure 20 as are the positive directions of  $W_s$  and  $V_s$ . Experimental data and predictions are presented for the various fuselage configurations with the wing attached. The largest effect indicated by the experiment is an increase in upwash of about  $1^\circ$  caused by the addition of the ducts. The sidewash does not show much variation. The theory predicts only part of this increase in upwash. This fact will be discussed later.

Figures 21(a) and 21(b) indicate the significant effects of inlet velocity ratio on the upwash and sidewash distributions for the configuration with the ducts attached amounting in some cases to several degrees. As the inlet velocity ratio is decreased, the measured upwash angles range from  $4.5^\circ$  to  $6^\circ$  at locations beyond one-third of the store length whereas the theory predicts only  $3.5^\circ$  on the average for all inlet velocity ratios. In figure 21(b), the measured sidewash actually turns inboard in the aft positions as the inlet velocity ratio is decreased. The sidewash predictions for the lower velocity ratios do indicate the trends including the cross over of the zero inlet velocity ratio curve but not to the extent shown by the experimental data. Referring to figure 12(b), locate the lower outboard corner of the duct. Consider a vortex shed from this corner with its axis parallel and next to the duct wall. The strength of the vortex increases with the amount of flow spilling over the lower inlet lip and with angle of attack. The circulation of the flow caused by the vortex would increase the upwash and add an inboard component to the sidewash and thus explain the differences between theory and experiment in figures 21(a) and 21(b).

Comparable results to those presented in figures 19 and 21 for  $\alpha = 6^\circ$  are presented in figures 22 and 23 for  $\alpha = 0^\circ$ . Figure 22 shows the effect of model buildup. There is a small measured effect which is fairly well predicted by the theory. Figure 23 indicates the effects of inlet velocity ratio. The changes indicated by the data when the velocity ratio is reduced are similar to those shown in figure 21 for  $\alpha = 6^\circ$  but are much smaller. They can also be explained by the presence of a vortex. The vortex strength is reduced since the angle of attack is  $0^\circ$ .

All wind-tunnel data presented here were obtained at a Reynolds number of  $3.4 \times 10^6$  per foot and a Mach number of 0.4. The effects of the vortex described above would be reduced with higher Reynolds number. Actual flight conditions would result in an order of magnitude higher Reynolds numbers than used during the tests. The accuracy of the flow prediction methods described here should increase when applied at flight Reynolds numbers.

### 5.3 Store Load Distributions

The force distributions along the finless store in the attached position, the position shown in figure 12(b) and 12(c) with the pylon removed, due to the upwash and sidewash fields just described are shown in figure 24 for the various stages of the model buildup. The positive force directions are shown in figure 20. The store half silhouette is outlined along the horizontal axis. The angle of attack is  $6^\circ$ . The normal-force distribution is affected very little by the fuselage buildup. The side-force distribution is affected somewhat more. Agreement between theory and experiment in loading is good even though some discrepancy exists in the flow-field comparisons shown in figures 19(a) and 19(b) at the aft positions along the store centerline. On the basis of slender-body theory, the loading on the cylindrical portion of the store only depends on the velocity gradient and not the magnitude. Figures 19(a) and 19(b) show the slopes of the theoretical lines in fair agreement with the experimental gradients. The peaks in the loading distributions of figure 24 are somewhat overpredicted as a consequence of slender-body theory. It has been shown in reference 1 that the use of a source-doublet method to calculate loading reduces the overprediction of the peaks at the expense of computer time.

Figures 25(a) and 25(b) show the effect of inlet velocity ratio on the loading distributions. When the ratio is reduced to one half, the measured local normal force is reduced in the region just aft of the store nose while the local side force shows an increase. The discrepancy between theory and experiment in terms of the flow field shown in figures 21(a) and 21(b) has a larger effect in this figure than the previous one. This discrepancy can be explained by a vortex near the lower outside corner of the inlet as was mentioned previously in connection with the flow fields. However, agreement between theory and experiment is considered good. The

side-force distribution over the nose region is overpredicted, partially due to the discrepancy in the predicted velocity gradient.

Comparisons between theory and experiment for  $\alpha = 0^\circ$  are shown in figures 26 and 27. These are for the same stages of model buildup and values of the inlet velocity ratio as shown in figures 24 and 25 for  $\alpha = 6^\circ$ . In general, the agreement between theory and experiment at  $\alpha = 0^\circ$  is as good as that obtained at  $\alpha = 6^\circ$ .

#### 5.4 Store Forces and Moments

In figures 28(a) and 28(b), the variations with angle of attack of the store forces and moments are shown for the various stages of the model buildup. The finless store is in the attached position but the pylon is not present, see figure 12(b). Up to  $6^\circ$  angle of attack, the effect of the fuselage configuration on the force and moment coefficients is small except for side force which is increased by adding the noncircular addition and duct assembly. In this angle-of-attack range, the theory is in good agreement with experiment although the predicted side-force slope for the configurations without inlets is slightly less negative than indicated by the experiment. At higher angles of attack, large variations are indicated by the experimental data due to highly nonlinear effects not accounted for by the theory.

Figures 29(a) and 29(b) show the effect of inlet velocity ratio on the force and moment coefficients. In the  $0^\circ$  to  $6^\circ$  angle-of-attack range, the experimental data indicate an increase in side force and yawing moment as the inlet velocity ratio is reduced. The side-force increment due to inlet velocity ratio is partially predicted by the theory but the yawing moment is not. The latter is determined from the side-force distribution in figure 25(b). In that figure, the predicted side-force loading overestimates the experimental loading on the nose, which tends to turn the store nose outboard. As was mentioned previously in connection with the flow fields, the reason for this discrepancy is the result of using slender-body theory as well as the result of a vortex shed from the lower, outboard inlet corner. In particular, the effect on sidewash and, therefore, side loading becomes more pronounced as the inlet velocity ratio is reduced. Increasing the Reynolds number would reduce this discrepancy as already discussed. At higher angles of attack, large nonlinearities are exhibited by the data.



## 5.5 Store Trajectories

The methods of analyzing noncircular fuselages with and without air inlets presented in a previous section have been incorporated into the six-degree-of-freedom trajectory prediction program described in reference 2. A number of trajectories have been run to provide predictions for several fuselage configurations for comparison with captive-store trajectories obtained in the wind tunnel. Comparisons with two of these trajectories will now be presented.

In order to represent full-scale conditions, the wind-tunnel models shown in figures 11 through 13 have been scaled up by a factor of twenty. The following input quantities have been used:

$$\text{Store Mass} = 15.53 \text{ slugs}$$

$$I_{xx} = 8 \text{ slug-ft}^2$$

$$I_{yy} = I_{zz} = 80 \text{ slug-ft}^2$$

$$I_{xy} = I_{yz} = I_{xz} = 0$$

$$M_{\infty} = 0.4$$

$$\text{Altitude} = 5000 \text{ ft}$$

$$\dot{\zeta}|_{t=0} = 10 \text{ ft/sec (initial vertical velocity of ejected store)}$$

$$\zeta|_{t=0} = 0.625 \text{ ft (initially, ejected store is one radius below attached position)}$$

Initial store and aircraft angles of attack are equal.

Comparison between calculated trajectories and captive-store trajectories for no damping are shown in figure 30 for two parent aircraft configurations and a store with cruciform empennage (fig. 13). The two parent aircraft configurations are the circular fuselage with wing and the circular fuselage with wing and duct assembly. For both configurations a pylon is at the one-third semispan location as shown in figure 12. For the latter configuration the inlet velocity ratio is 0.5. The store is ejected at  $t = 0$  with a 10-ft/sec downward velocity one store radius beneath its attached position on the pylon at the one-third semispan

position under the left wing panel. The angle of attack is  $6^\circ$  and the Mach number is 0.4.

In figure 30 the three left-hand curves show the position of the store center of gravity relative to its carriage position on the pylon. The positions  $\xi, \eta, \zeta$  are respectively positive forward, positive to the right (inboard), and positive down. The left-hand curves show a slight rearward movement of the store, no lateral movement, and a vertical movement equivalent to free fall. Fuselage effects are minimal and the motion is well predicted. The two right-hand curves are the angular attitudes of the store. The angles  $\Delta\theta$  and  $\Delta\psi$  are respectively pitch, positive nose up, and yaw, positive nose to the right. The theory agrees quite well with experiment for the model without the inlets. The experimental data show an influence of the inlets when they are attached to the fuselage. The effect of the inlets on the pitch motion is well predicted. The effect of the inlets on the yaw motion is not well predicted. This could be a result of vortices shed from the inlets as was discussed in conjunction with the flow-field data, section 5.2.

One other theoretical curve has been added to the pitch-motion plot. This curve is the pitch-motion time history when there is no interference flow field. The effect of the interference flow field is well predicted.

## 6. CONCLUDING REMARKS

This report presents the results of an investigation which has been conducted with the objective of improving the store separation prediction method of reference 1. In that work the parent aircraft fuselage was restricted to one which was circular in cross section and fuselage-mounted engine air inlets were not included. Also, wing-fuselage interference was not accounted for, thus, precluding the accurate calculation of the velocity field near the wing-fuselage juncture. These shortcomings have all been eliminated in the present work.

In the work of reference 1 the fuselage was restricted to an uncambered body with a circular cross section. In the present work the cross section is arbitrary and can change from one axial station to the next. The basic method employed to model such bodies uses a distribution of three-dimensional point sources and sinks along the longitudinal axis of an equivalent body of revolution to account for far field effects. Polar harmonic

singularities and a two-dimensional source term account for the near field solution and satisfy the flow tangency condition at points on the actual body contour. In this way fuselage angle-of-attack effects as well as noncircular fuselage cross section and changes in shape with axial distance are accounted for. Fuselage-mounted engine inlets are included in the noncircular cross section. Inlet velocity ratios between zero and one are modeled by modifying the streamwise body slope in the boundary condition.

Wing-fuselage interference is accounted for by a modification of the wing-pylon vortex-lattice model of reference 1. The vortices are laid out on the exposed wing panels and an image vortex system is constructed inside the equivalent body of revolution. By including fuselage-induced velocities in the wing-pylon flow tangency condition, the boundary condition of no flow through the actual fuselage surface is very nearly satisfied.

In conjunction with the analytical work, an extensive and systematic wind-tunnel test program was carried out to provide data for checking the accuracy of the flow models. A wind-tunnel model was constructed which allowed the fuselage to be built up systematically from a circular cross section to a noncircular cross section with air inlets. The inlet velocity ratio could be varied between zero and unity.

Fair to good agreement between experiment and prediction for flow fields, store loading distributions, store forces and moments, and store trajectories was obtained. Most of the differences between experiment and theory are believed to be due principally to vortices shed from the sharp lower corners of the inlets. Their influence should be reduced at higher Reynolds numbers. Actual flight conditions would result in an order of magnitude higher Reynolds number than that which was used in the test program. The theory should also produce more accurate results for configurations with noncircular cross sections with fewer sharp corners than are present on the wind-tunnel model.

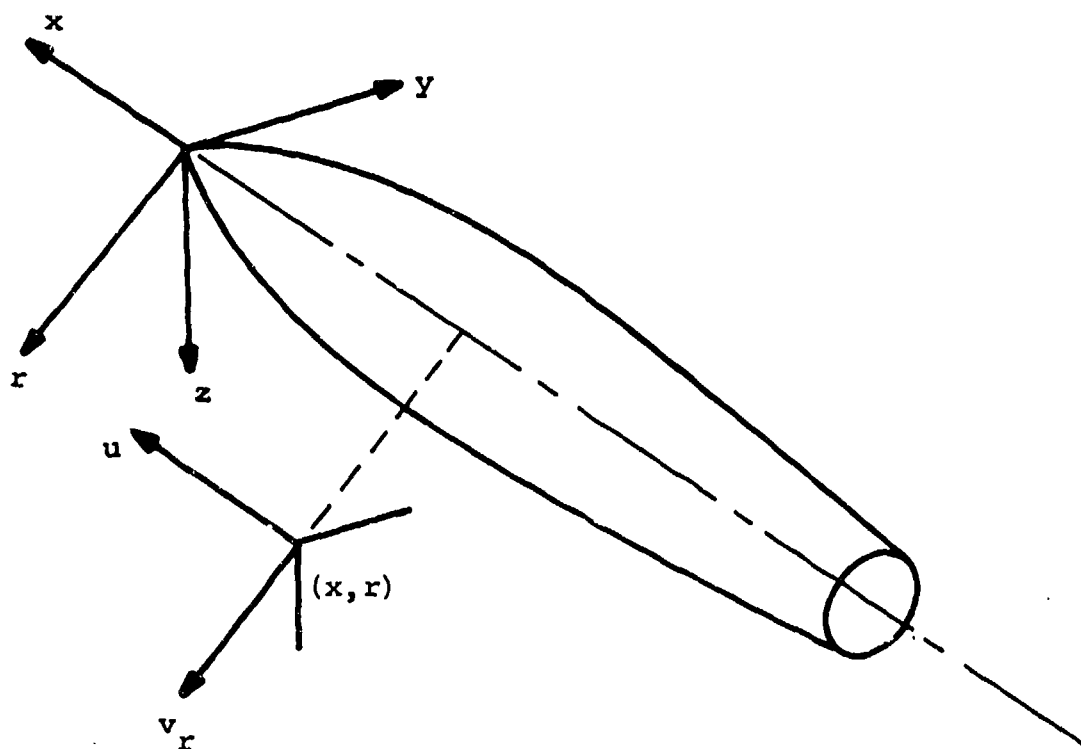
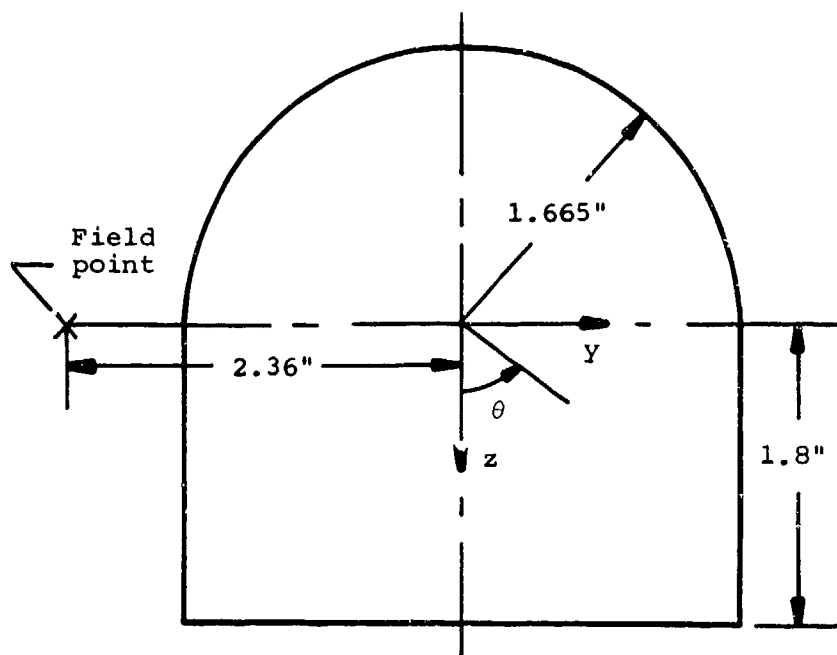
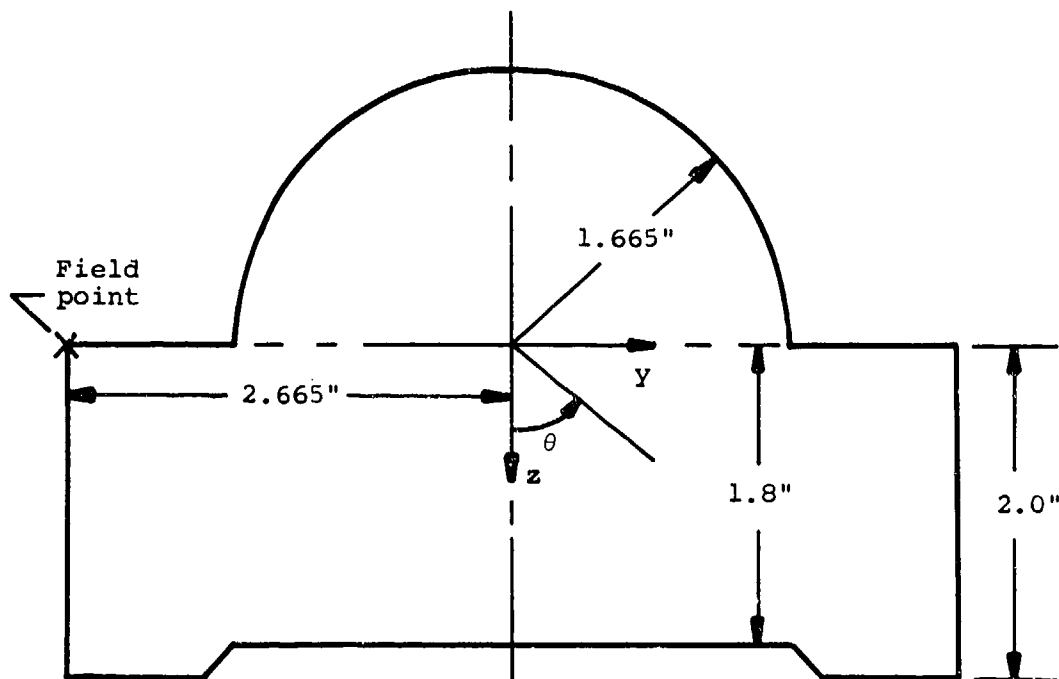


Figure 1.- Coordinate system for an axisymmetric body.



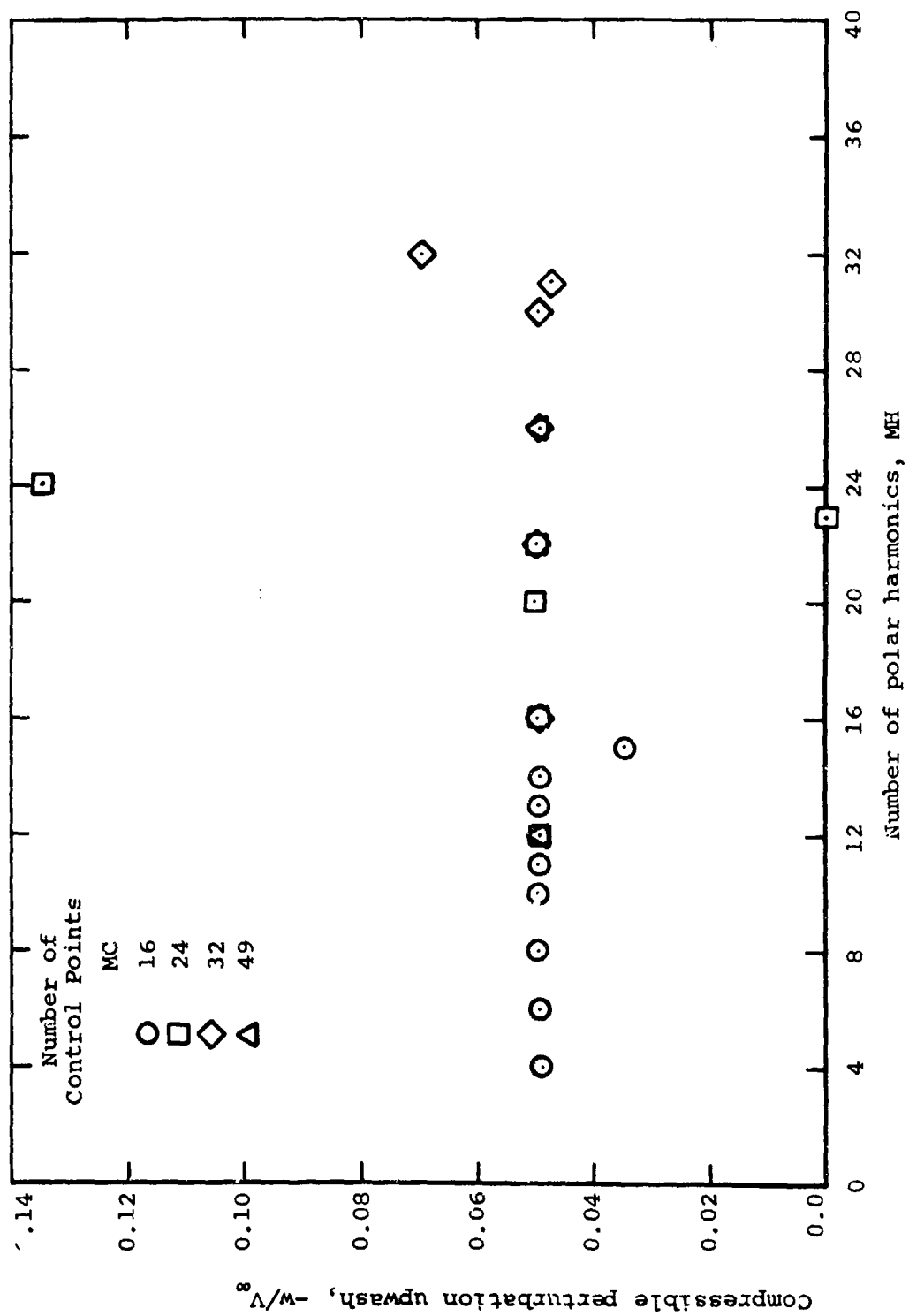


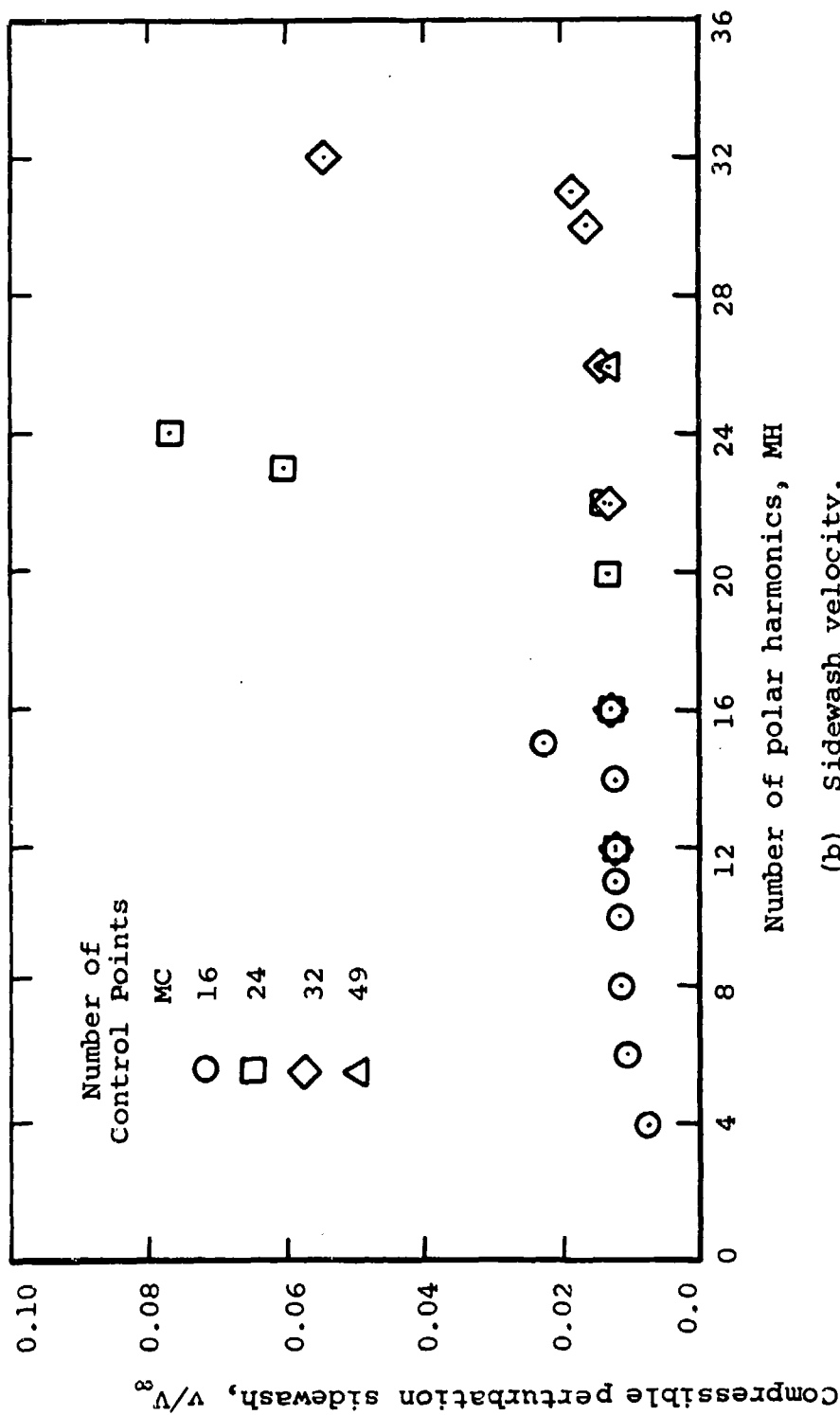
(a) Body contour A.



(b) Body contour B.

Figure 3.- Example body contours.

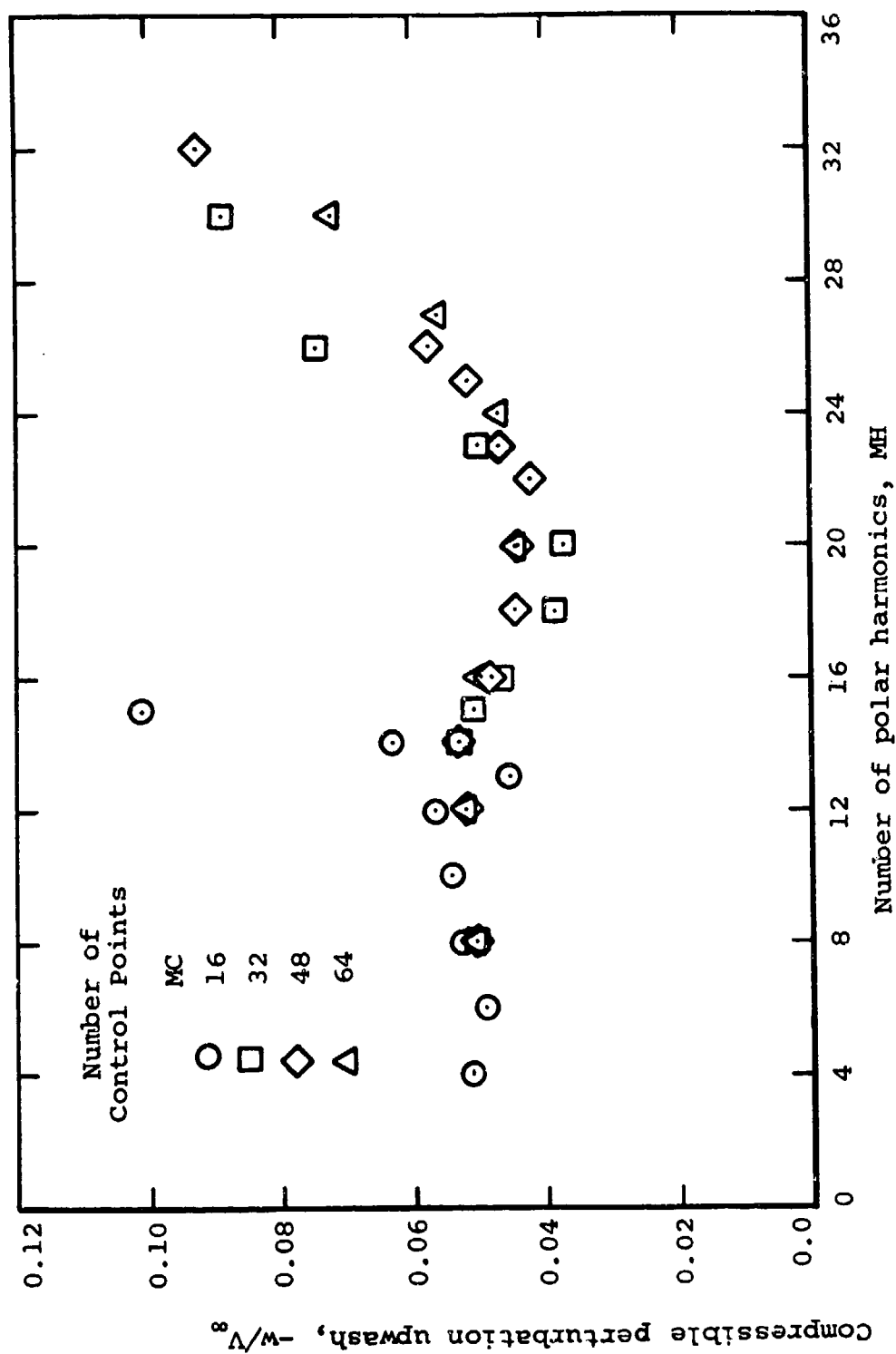




(b) Sidewash velocity.

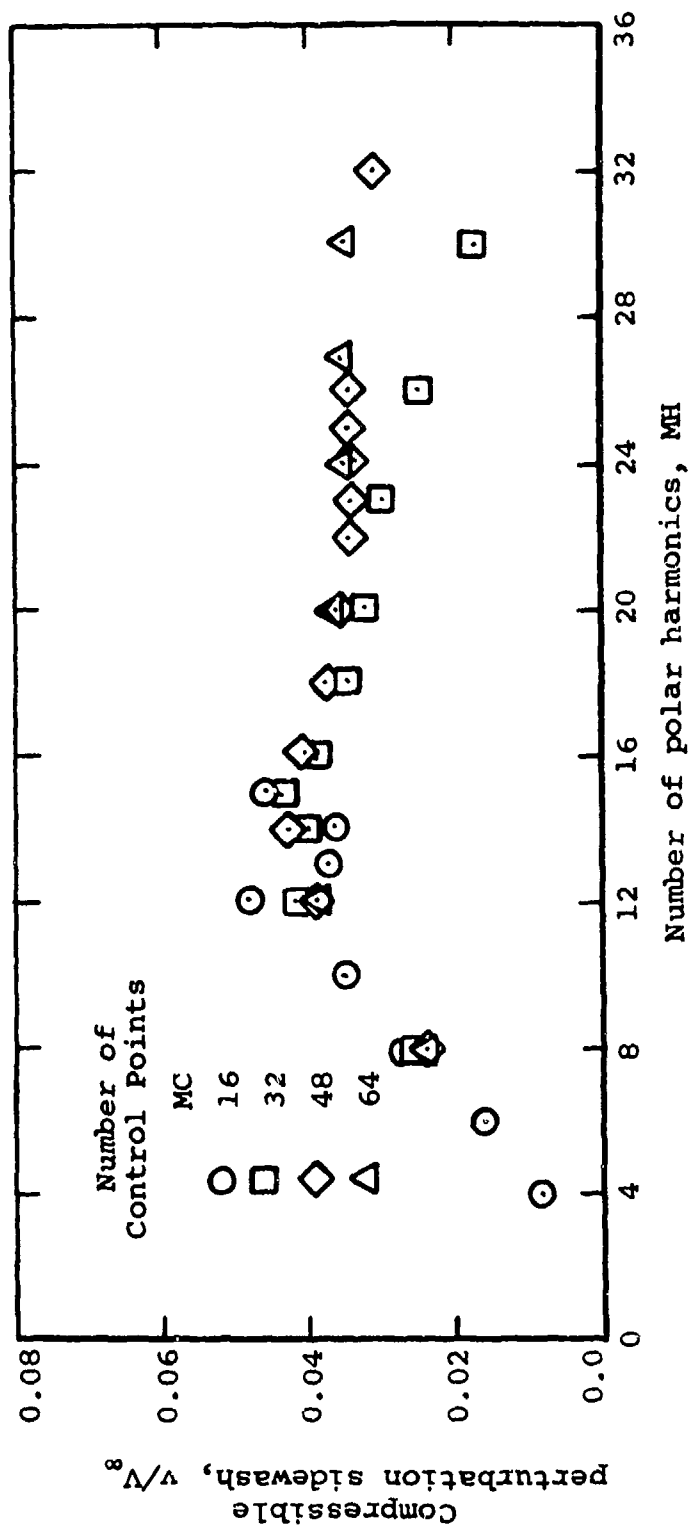
Figure 4.- Concluded.





(a) Upwash velocity.

Figure 5.- Range of validity tests for body contour B;  
 $\alpha = 6^\circ$ ,  $M_\infty = 0.4$ .



(b) Sidewash velocity.

Figure 5.- Concluded.

MC = 24  
MH = 16

$a_n$

-.96134E-01  
-.13200E-01  
-.76638E-02  
.12195E-02  
.67647E-02  
.69854E-02  
.37602E-02  
-.81159E-04  
-.26141E-02  
-.31733E-02  
-.21305E-02  
-.50135E-03  
.68831E-03  
.10052E-02  
.69826E-03  
.27002E-03

MC = 24  
MH = 23

$a_n$

-.12116E+00  
-.50052E-01  
-.20894E-01  
.21153E-01  
.37335E-01  
.23947E-01  
.54654E-02  
-.10154E-01  
-.33487E-01  
-.52540E-01  
-.33184E-01  
.27987E-01  
.87369E-01  
.10250E+00  
.62290E-01  
-.35366E-01  
-.17926E+00  
-.28671E+00  
-.21270E+00  
.98925E-01  
.48041E+00  
.63723E+00  
.42465E+00

Figure 6.- Polar harmonic coefficients  $a_n$   
calculated for body contour A with  
24 control points and 16 and 23  
polar harmonics;  
 $\alpha = 6^\circ$ ,  $M_\infty = 0.4$ .

MC = 32  
MH = 14

$a_n$

-.10742E+00  
-.24012E-01  
.36529E-02  
.17743E-01  
.10662E-01  
-.23899E-02  
-.73013E-02  
-.38294E-02  
.74858E-03  
.20669E-02  
.10233E-02  
-.37444E-04  
-.27350E-03  
-.11336E-03

MC = 32  
MH = 30

$a_n$

-.13063E+00  
-.35756E-01  
.51891E-02  
.21817E-01  
.29237E-01  
.27075E-01  
-.95736E-02  
-.60023E-01  
-.61313E-01  
.63593E-02  
.88965E-01  
.11368E+00  
.40846E-01  
-.10983E+00  
-.23037E+00  
-.16265E+00  
.12826E+00  
.41233E+00  
.35317E+00  
-.10296E+00  
-.56759E+00  
-.56276E+00  
-.41869E-01  
.53004E+00  
.65036E+00  
.27210E+00  
-.21349E+00  
-.41983E+00  
-.30639E+00  
-.10183E+00

Figure 7.- Polar harmonic coefficients  $a_n$   
calculated for body contour B with  
32 control points and 14 and 30  
polar harmonics;  
 $\alpha = 6^\circ$ ,  $M_\infty = 0.4$ .

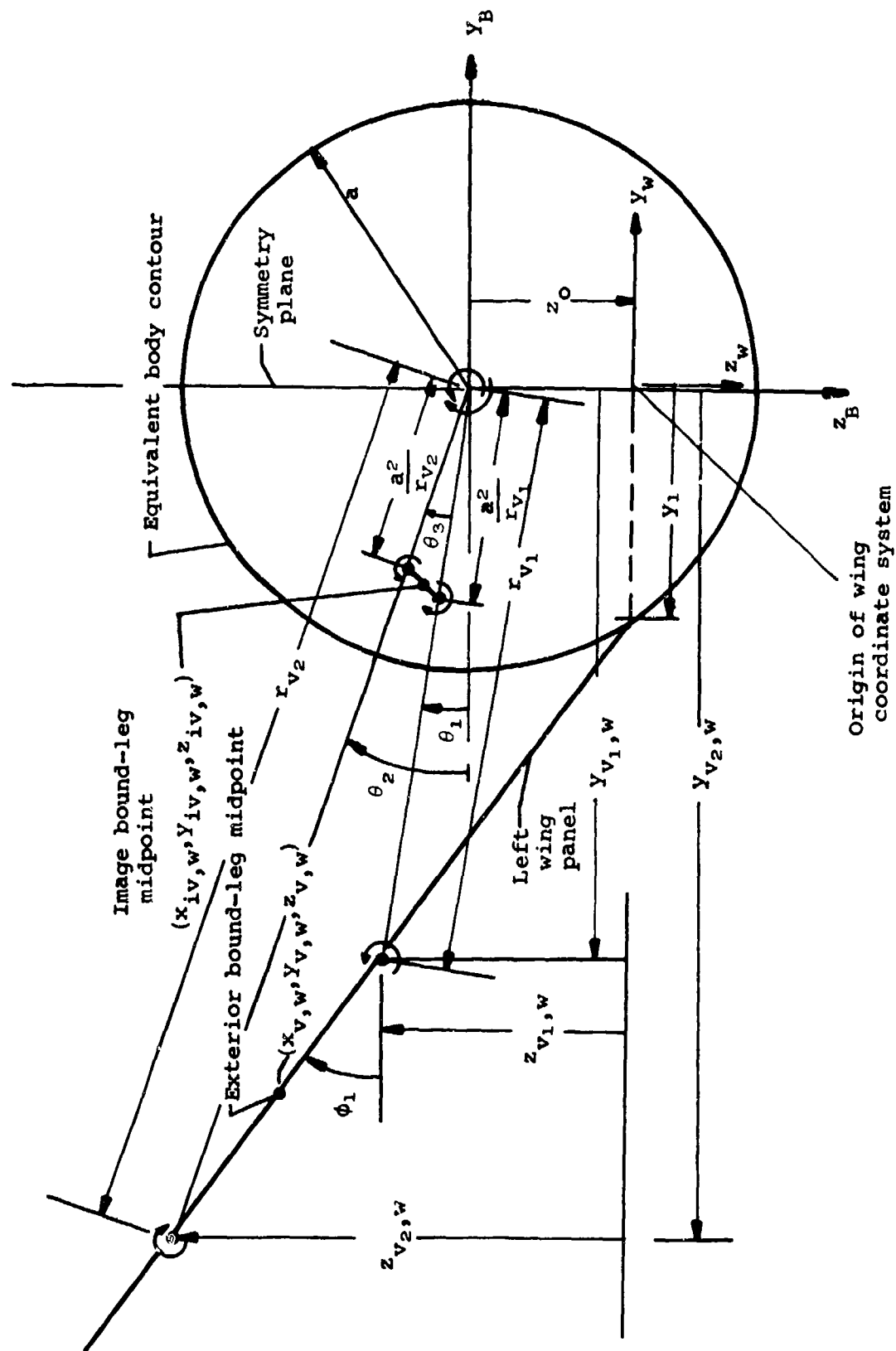


Figure 8.- Horseshoe vortex imaging method shown in elevation.

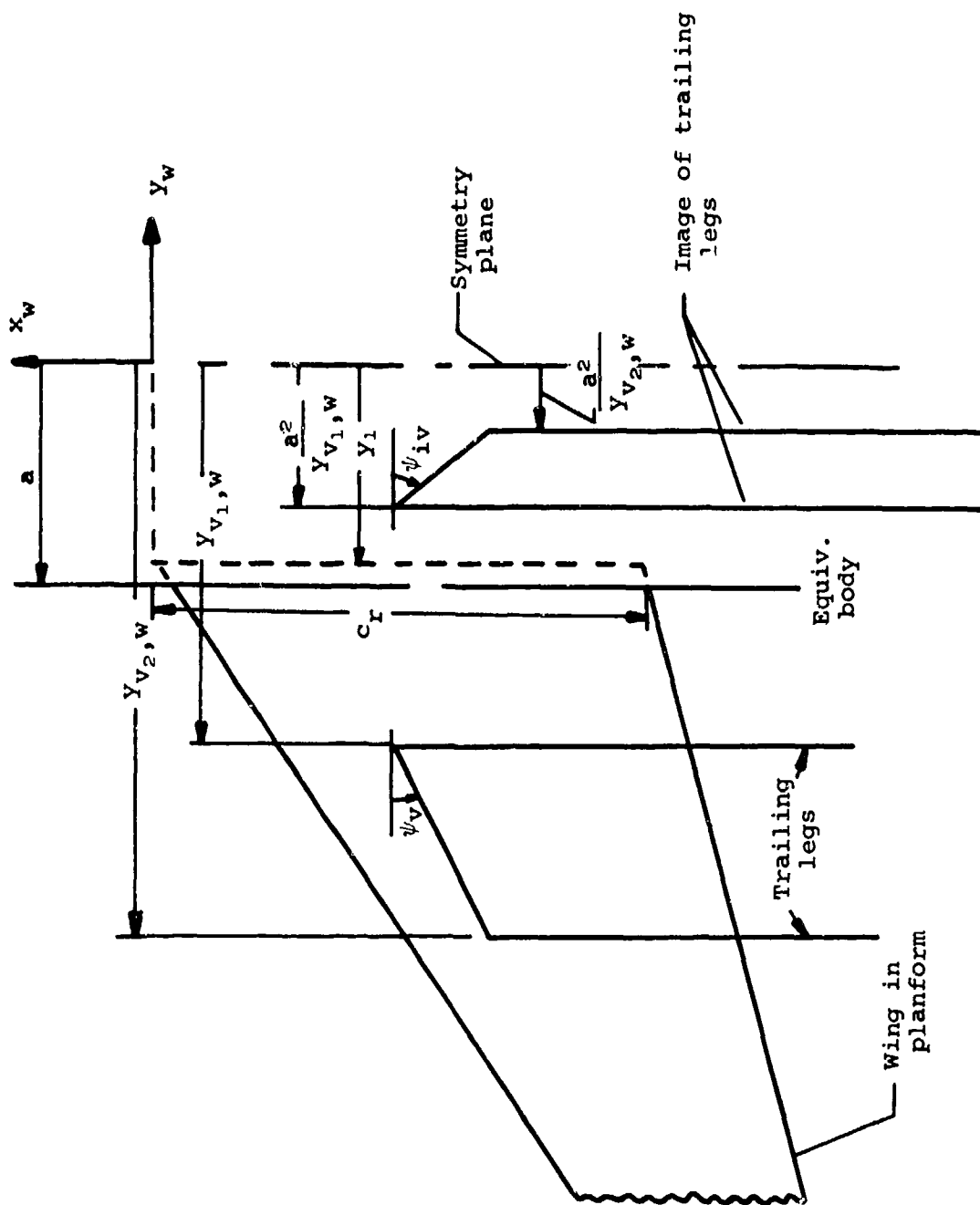


Figure 9.- Horseshoe vortex imaging method shown in planform.

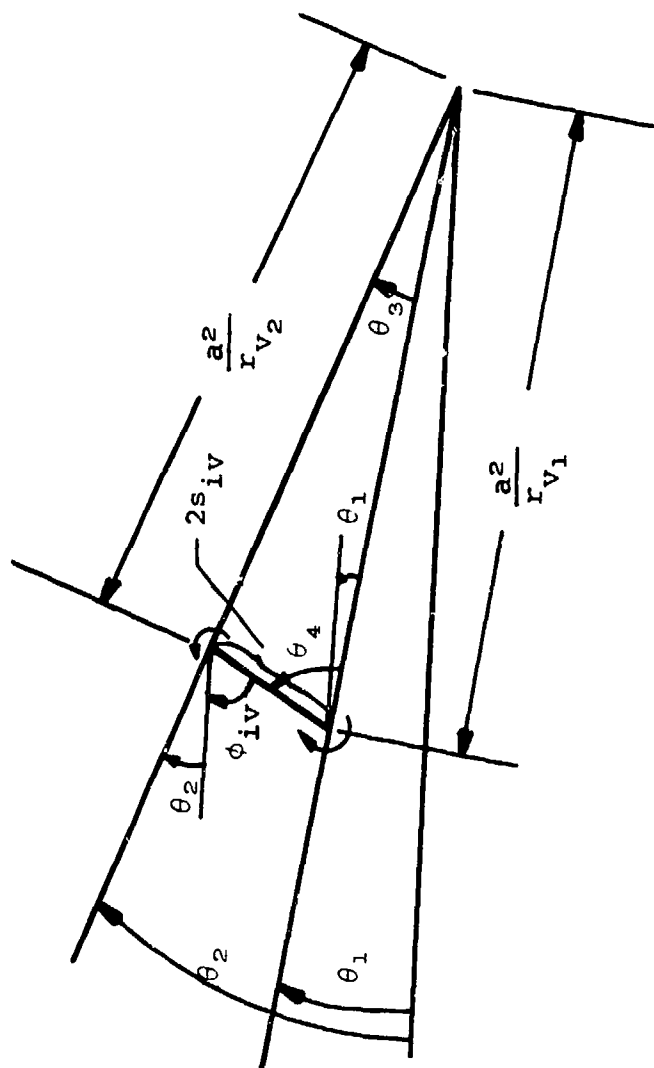


Figure 10.- Enlargement of image vortex region  
shown in elevation.

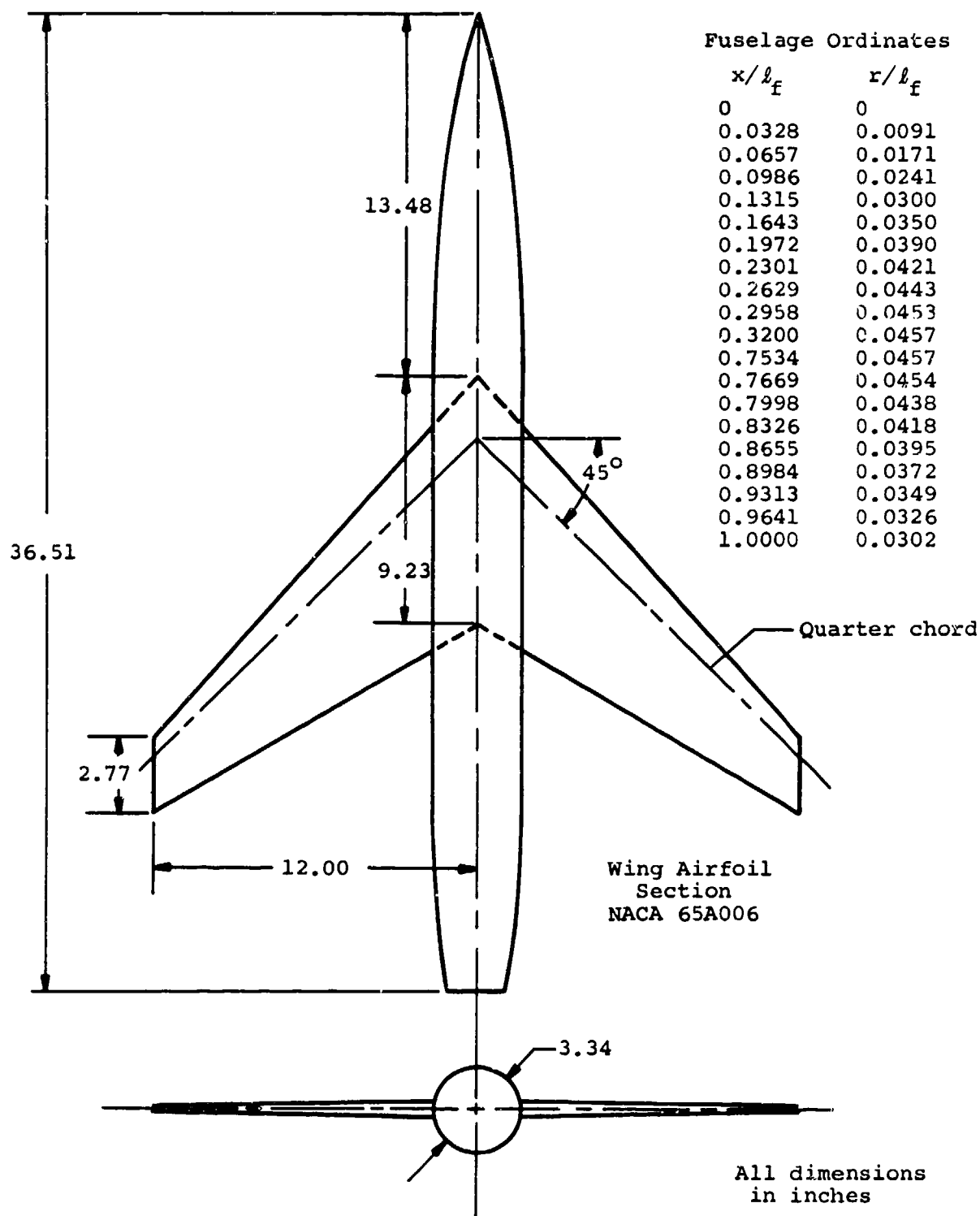
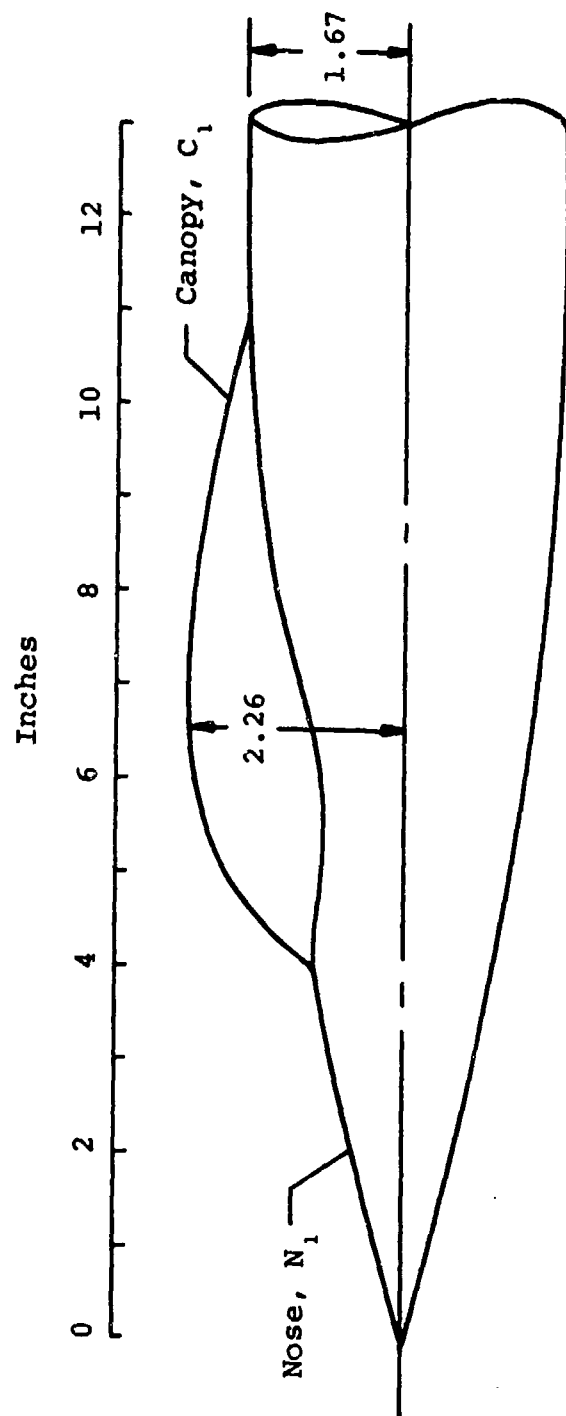
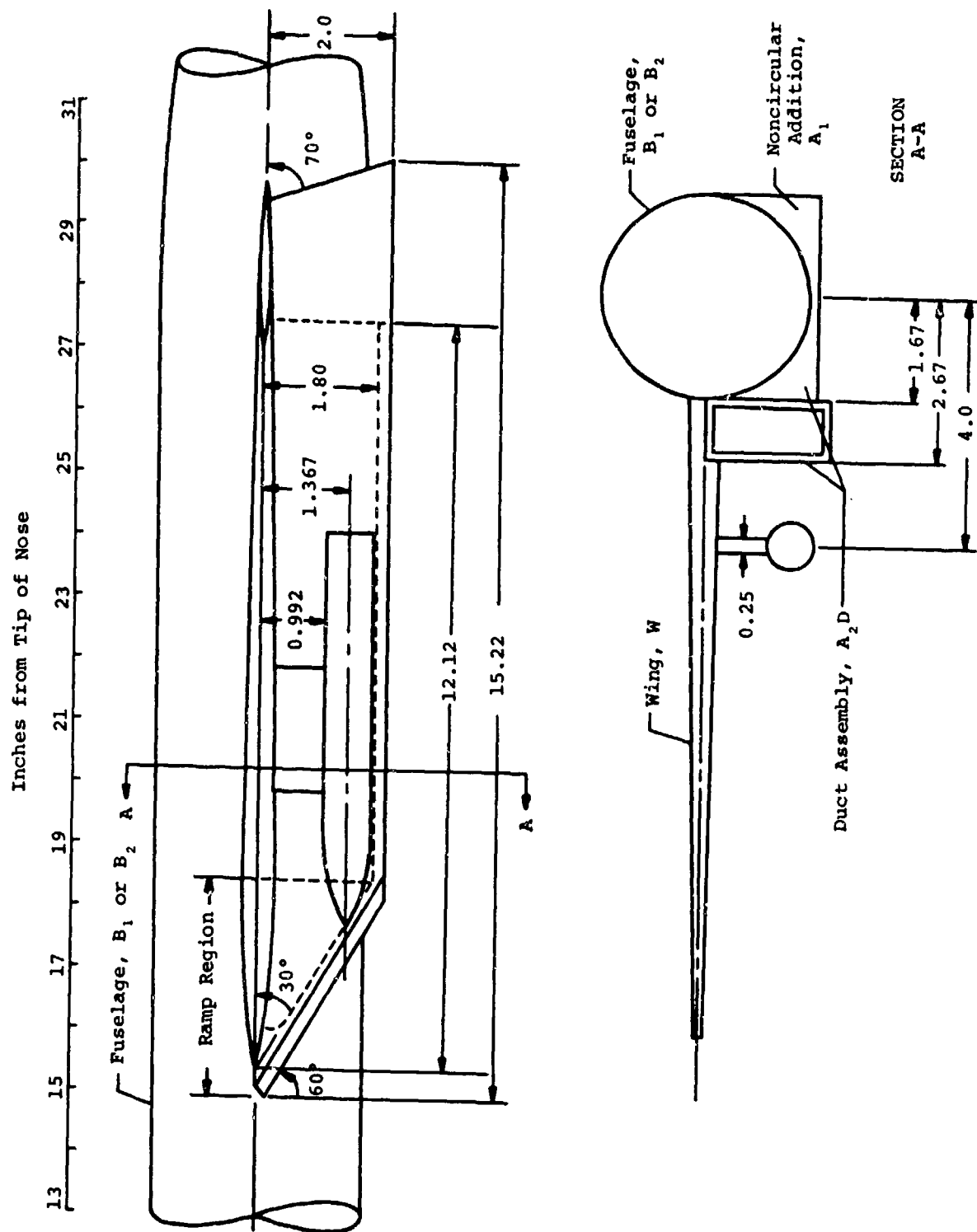


Figure 11.- Wing-fuselage combination.



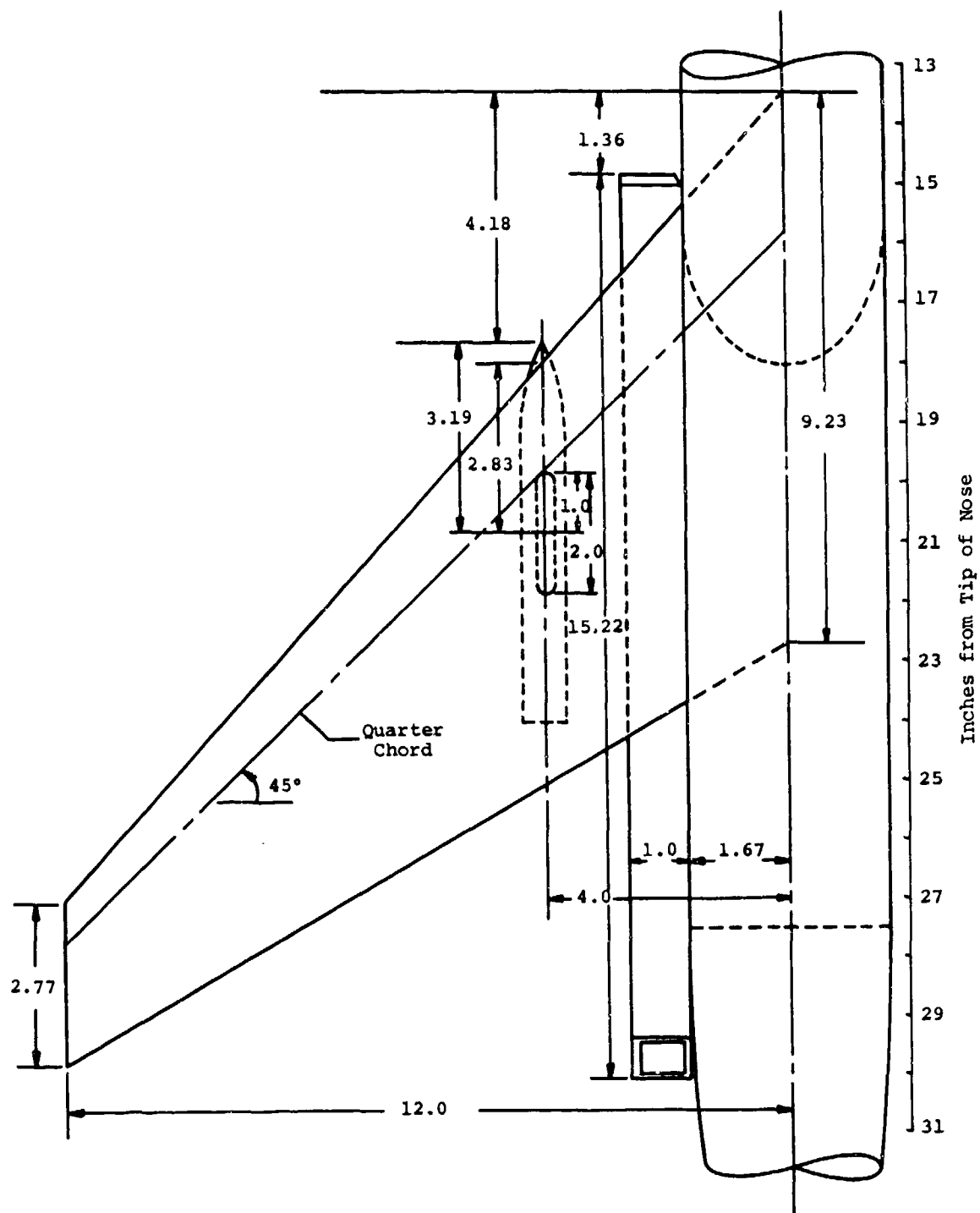


(a) Canopy mounted on fuselage nose.  
Figure 12.- Modified wind-tunnel model.



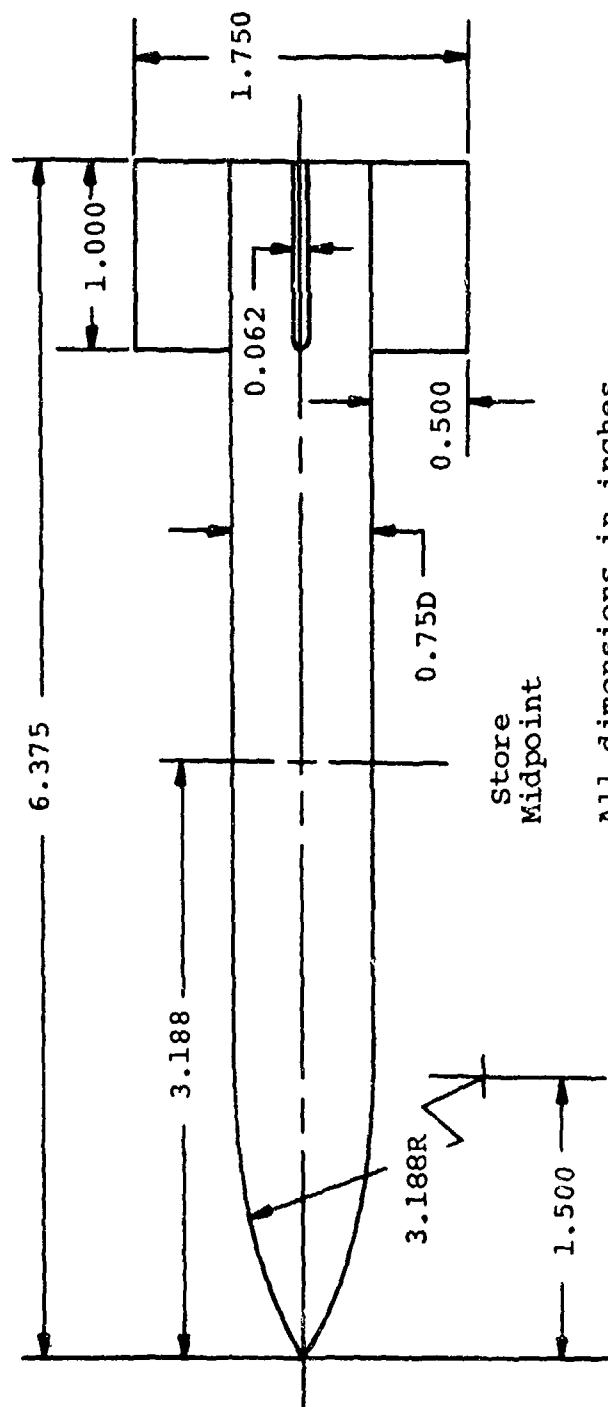
(b) Wing and duct assembly attached to circular fuselage.

Figure 12.- Continued.



(c) Top view of wing and duct assembly attached to circular fuselage.

Figure 12.- Concluded.



All dimensions in inches.

Figure 13.- Ogive-cylinder store with rectangular cruciform fins.

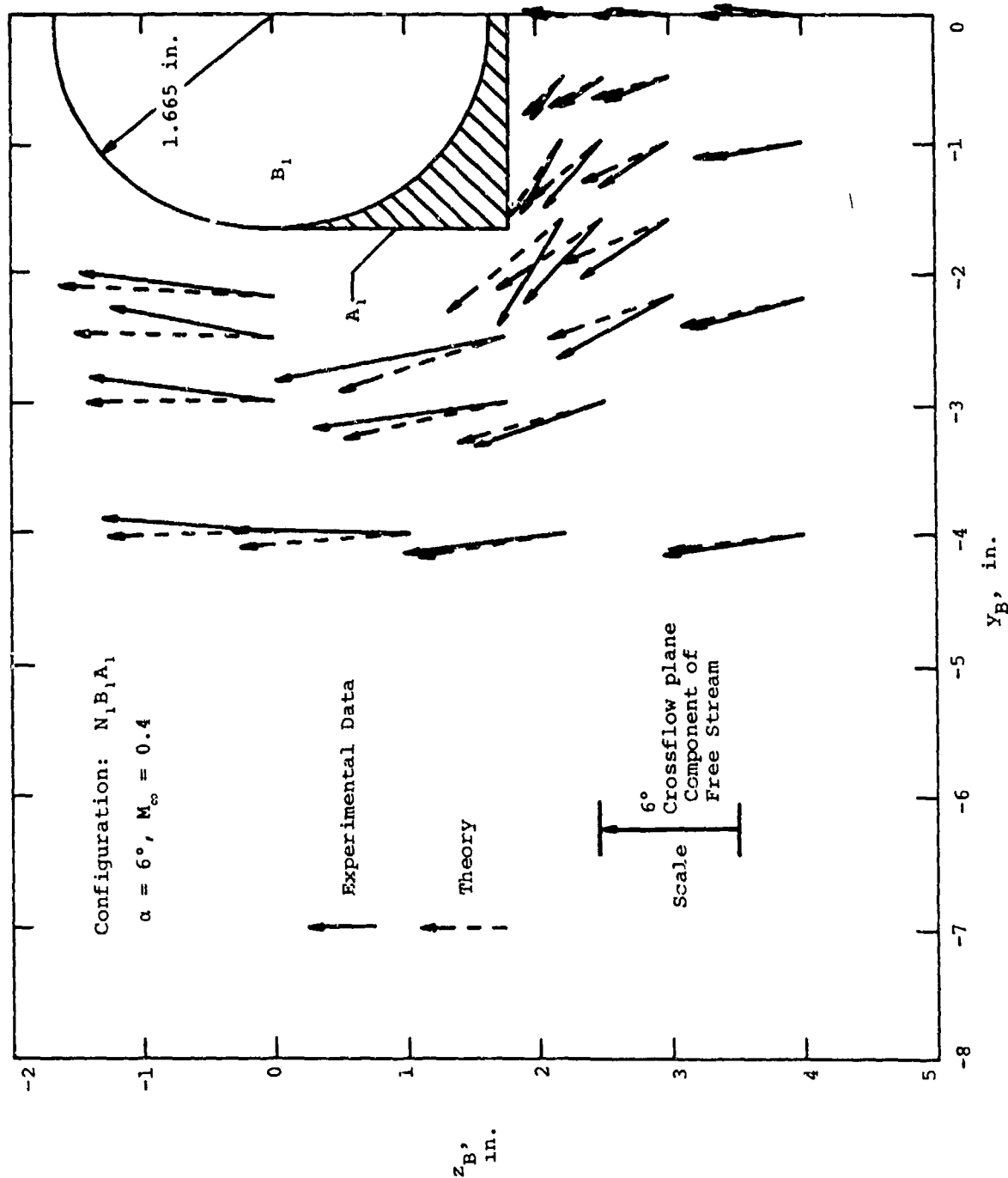
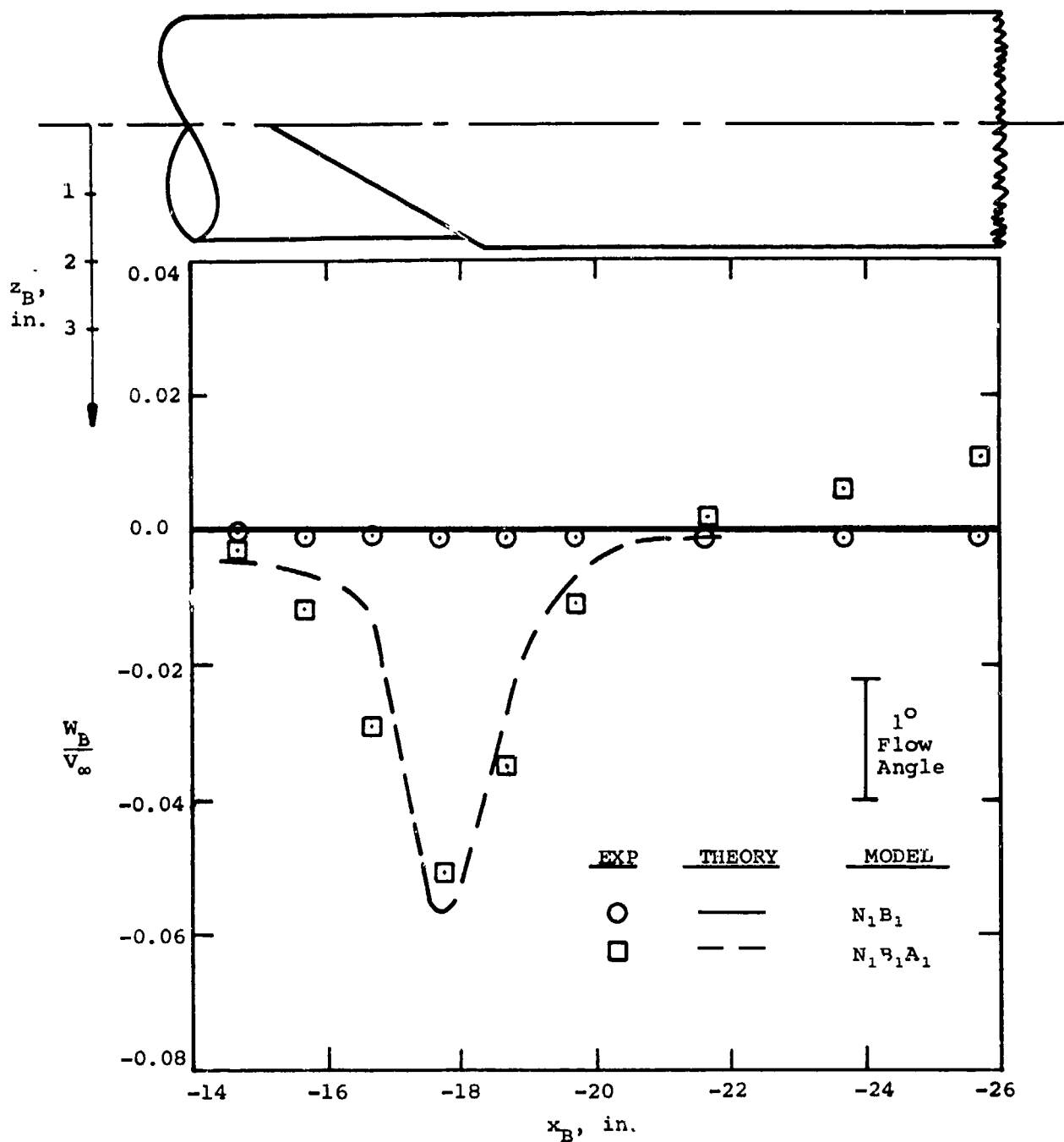
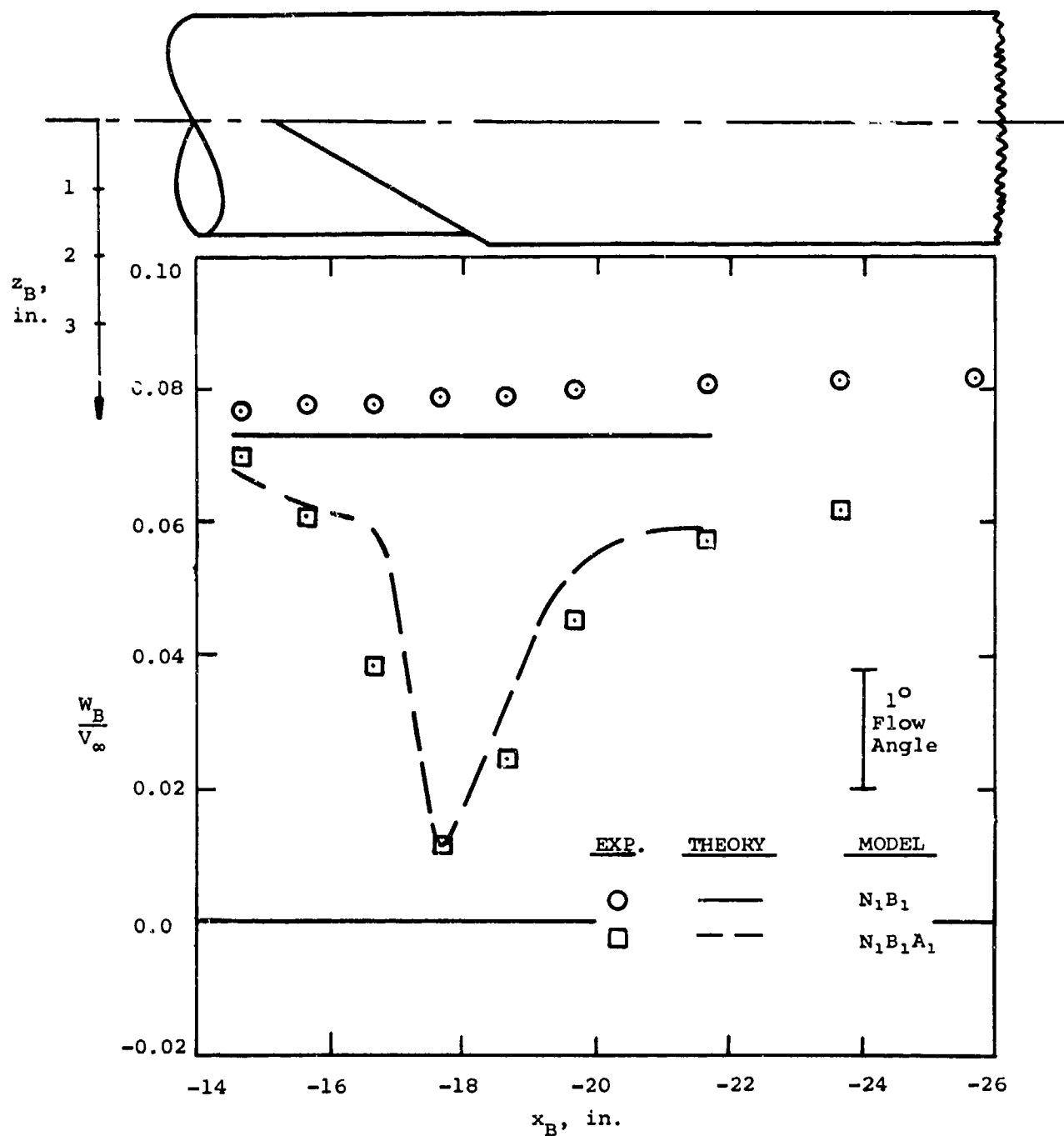


Figure 14.- Velocity vector plot for noncircular fuselage in crossflow plane 19.66 inches aft of nose tip.



(a)  $\alpha = 0^\circ$ .

Figure 15.- Distribution of upwash 3 inches under the fuselage centerline for the circular fuselage and for noncircular addition attached to the fuselage;  $M_\infty = 0.4$ .



(b)  $\alpha = 6^\circ$ .

Figure 15.- Concluded.

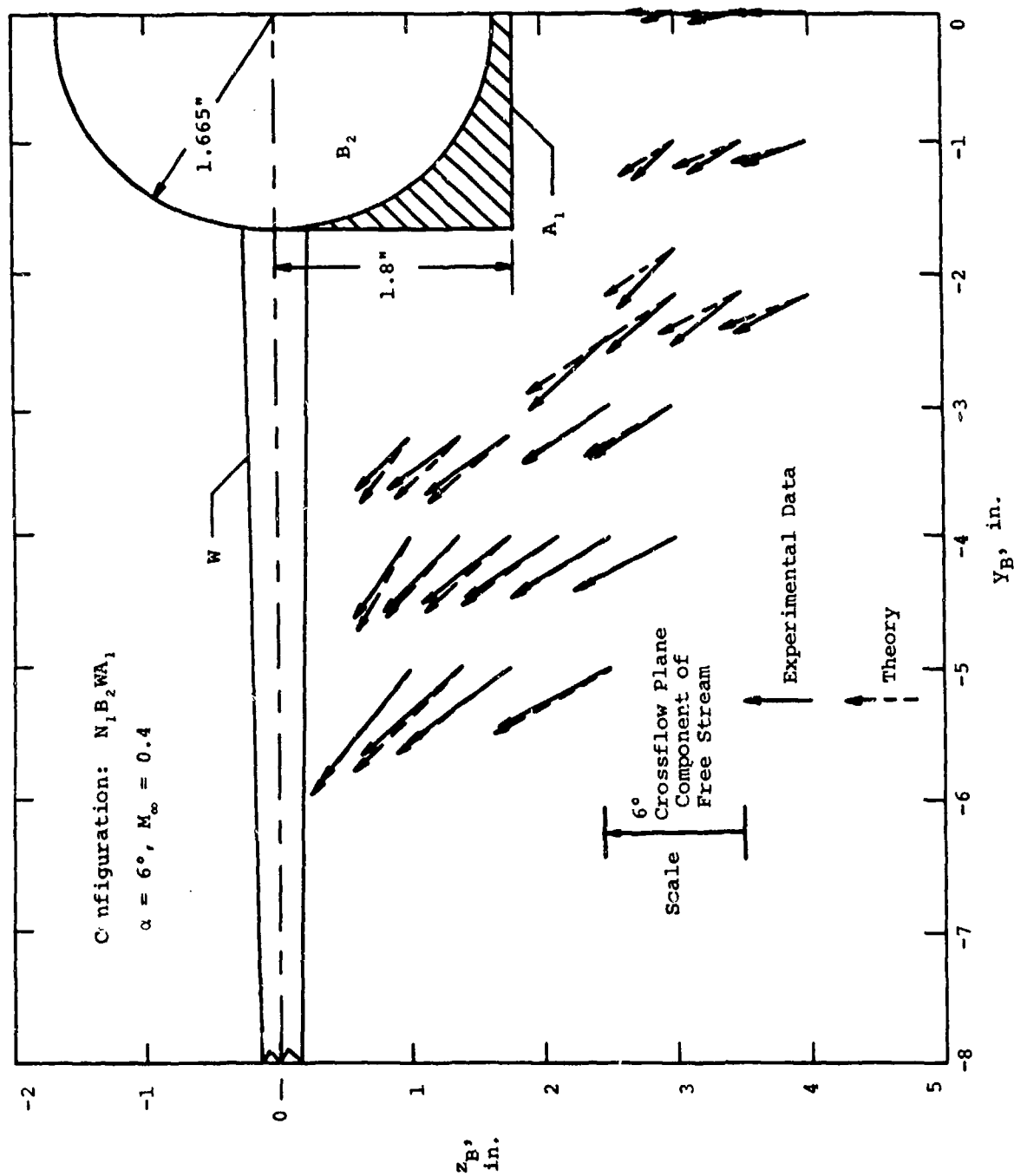
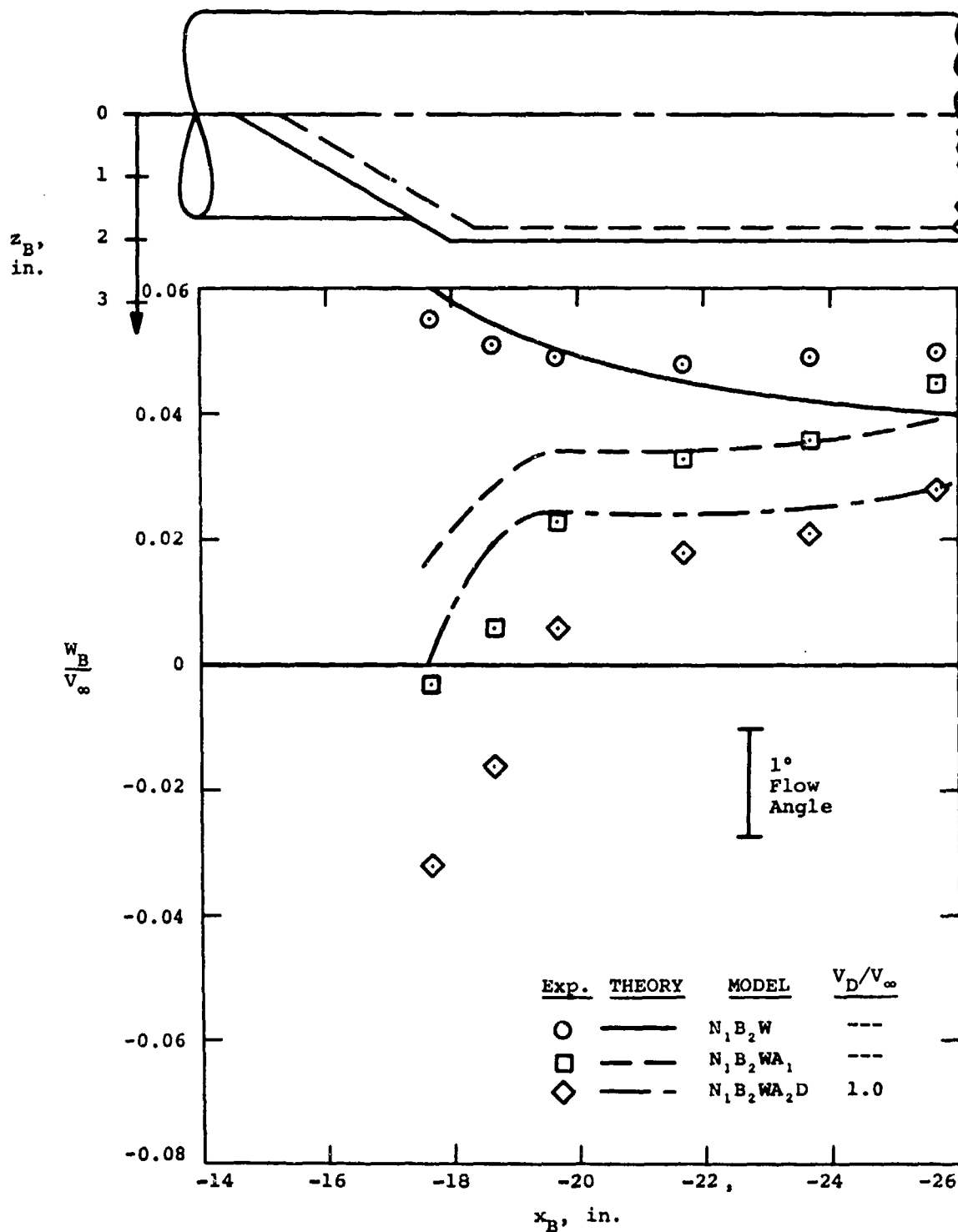


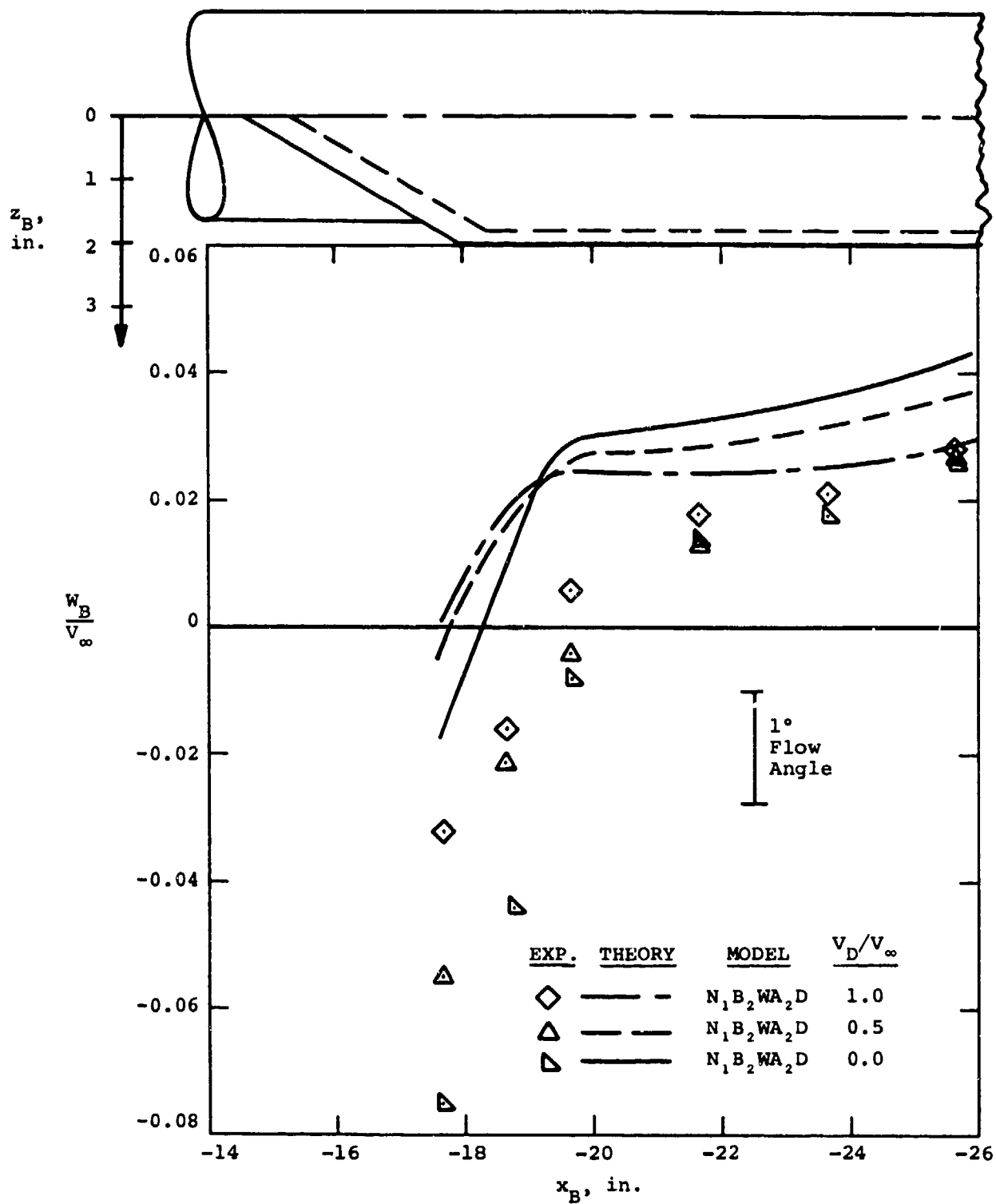
Figure 16.- Velocity vector plot for wing attached to noncircular fuselage in crossflow plane 19.66 inches aft of nose tip.





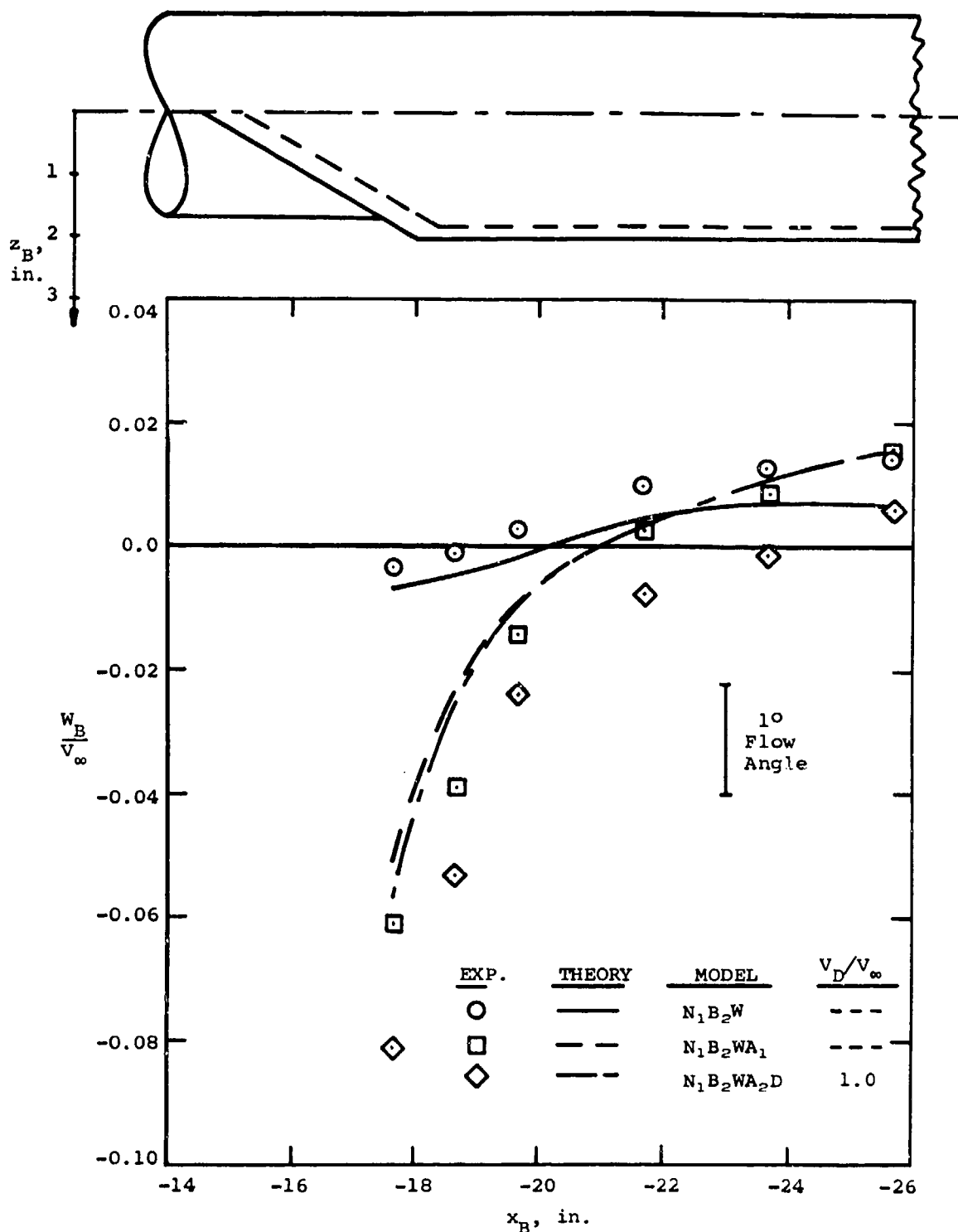
(a) Effects of wind-tunnel model build-up.

Figure 17.- Distribution of upwash 3 inches under the fuselage centerline;  $\alpha = 6^\circ$ ,  $M_\infty = 0.4$ .



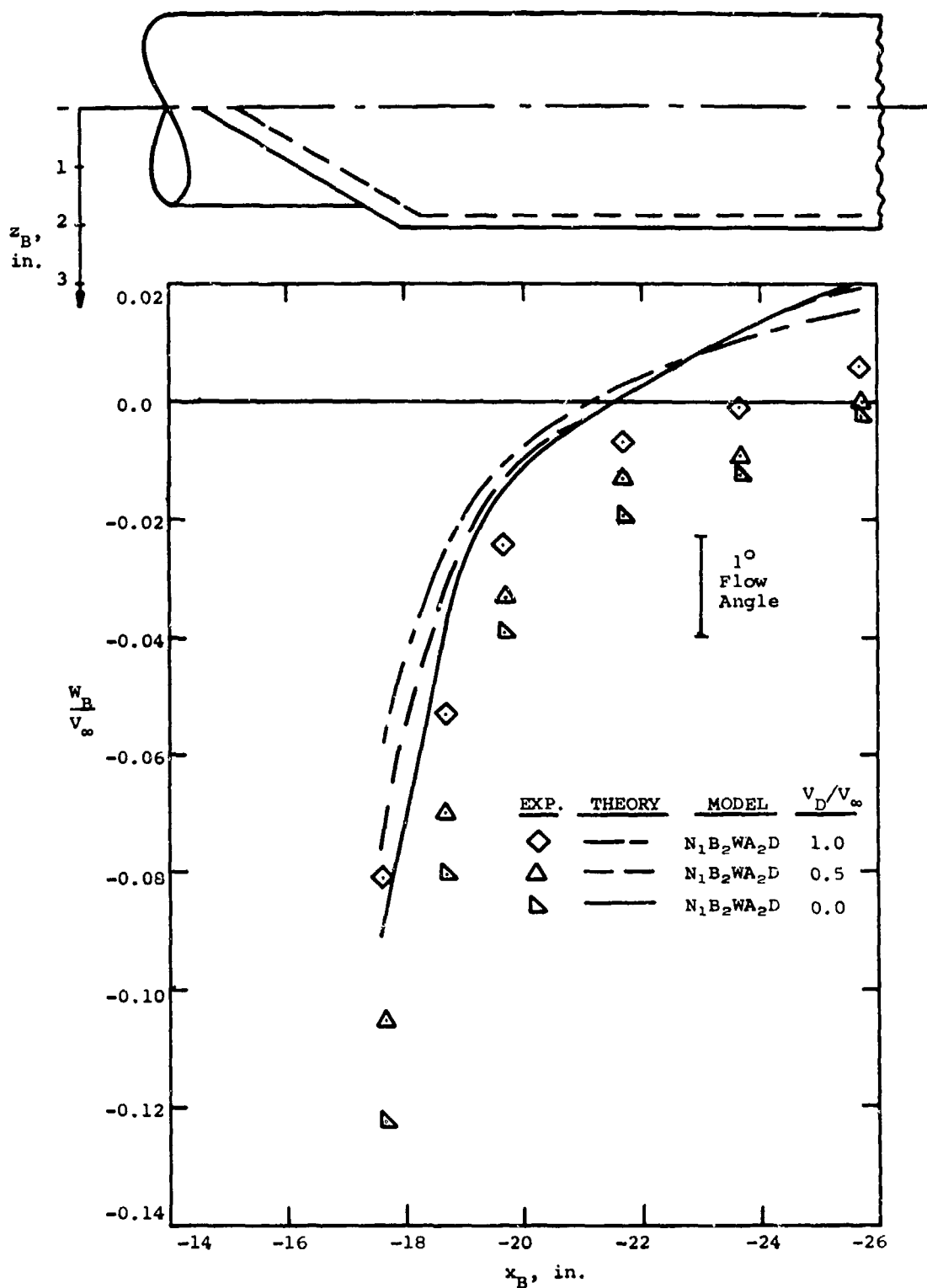
(b) Effects of inlet velocity ratio.

Figure 17.- Concluded.



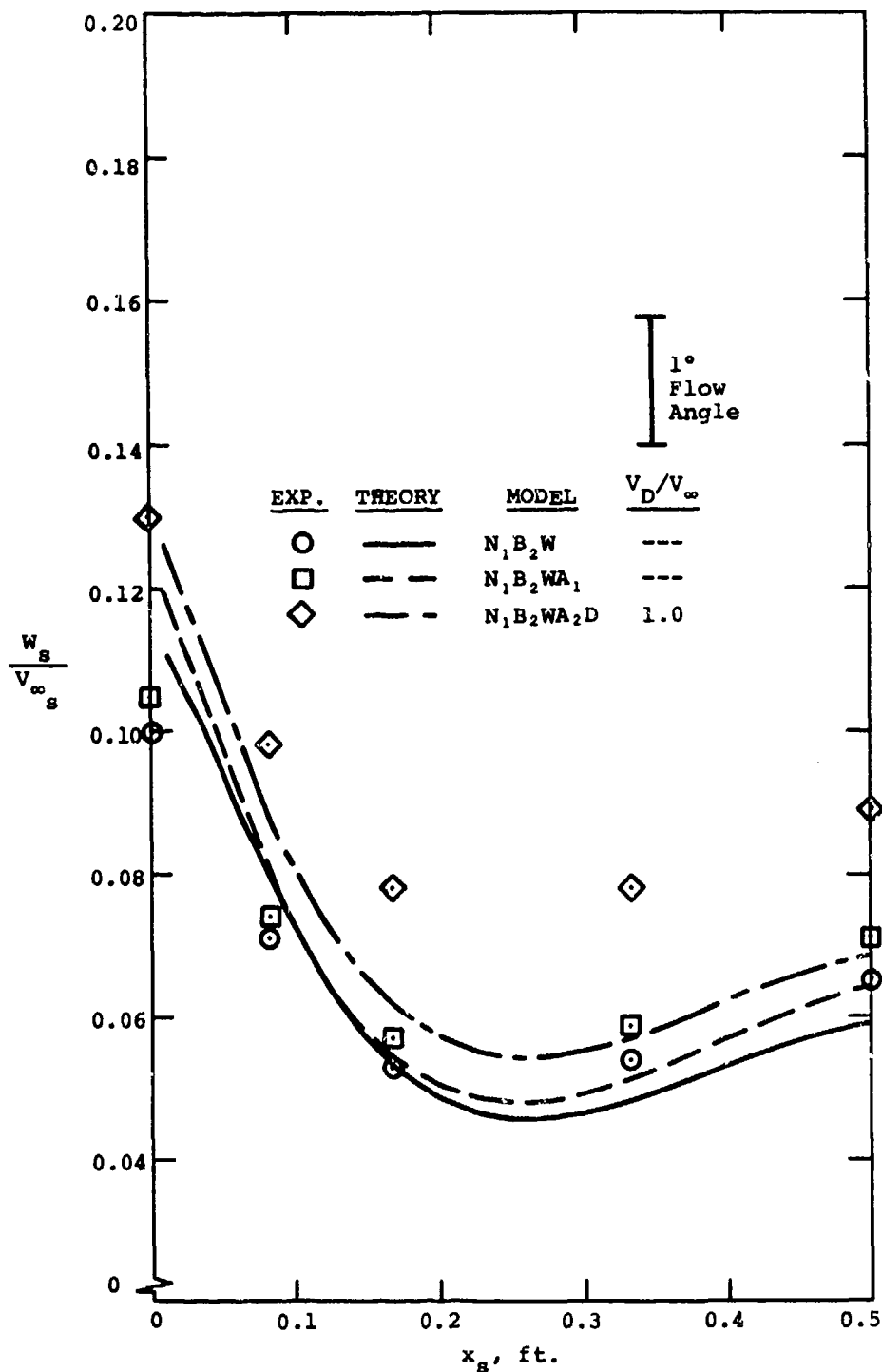
(a) Effects of wind-tunnel model build-up.

Figure 18.- Distribution of upwash 3 inches under the fuselage centerline;  $\alpha = 0^\circ$ ,  $M_\infty = 0.4$ .



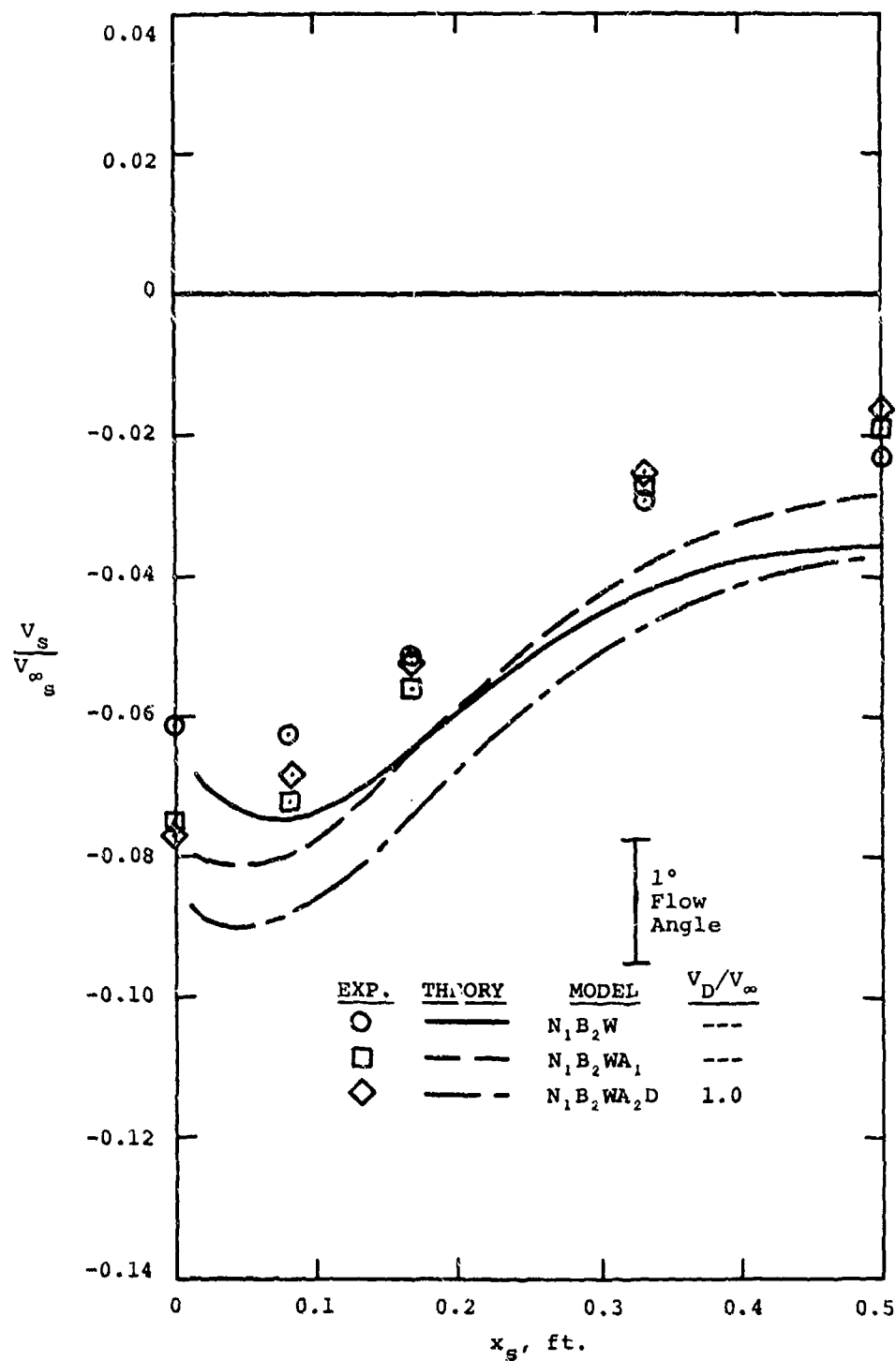
(b) Effects of inlet velocity ratio.

Figure 18.- Concluded.



(a) Upwash distribution.

Figure 19.- Effect of wind-tunnel model build-up on the flow field in the region the store centerline would occupy if the store was present;  
 $\alpha = 6^\circ$ ,  $M_\infty = 0.4$ .



(b) Sidewash distribution.

Figure 19.- Concluded.

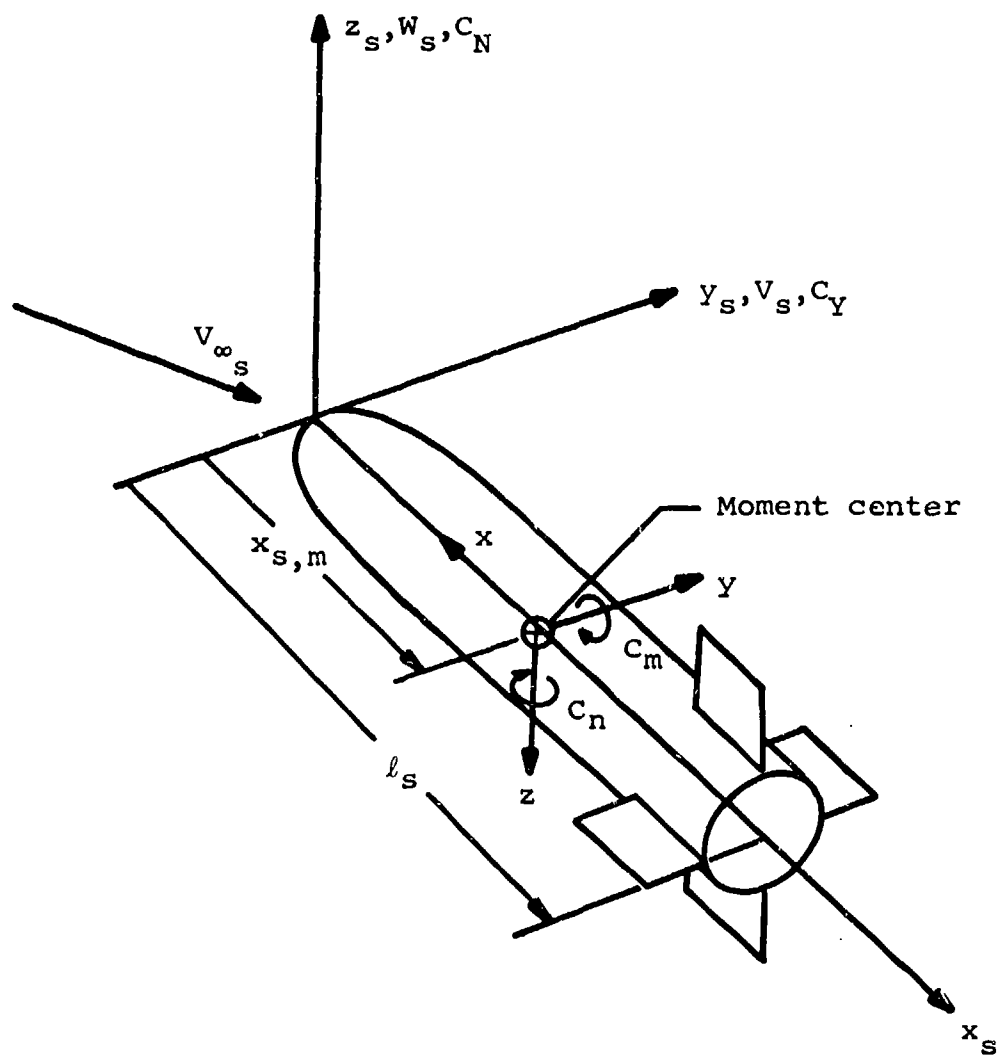
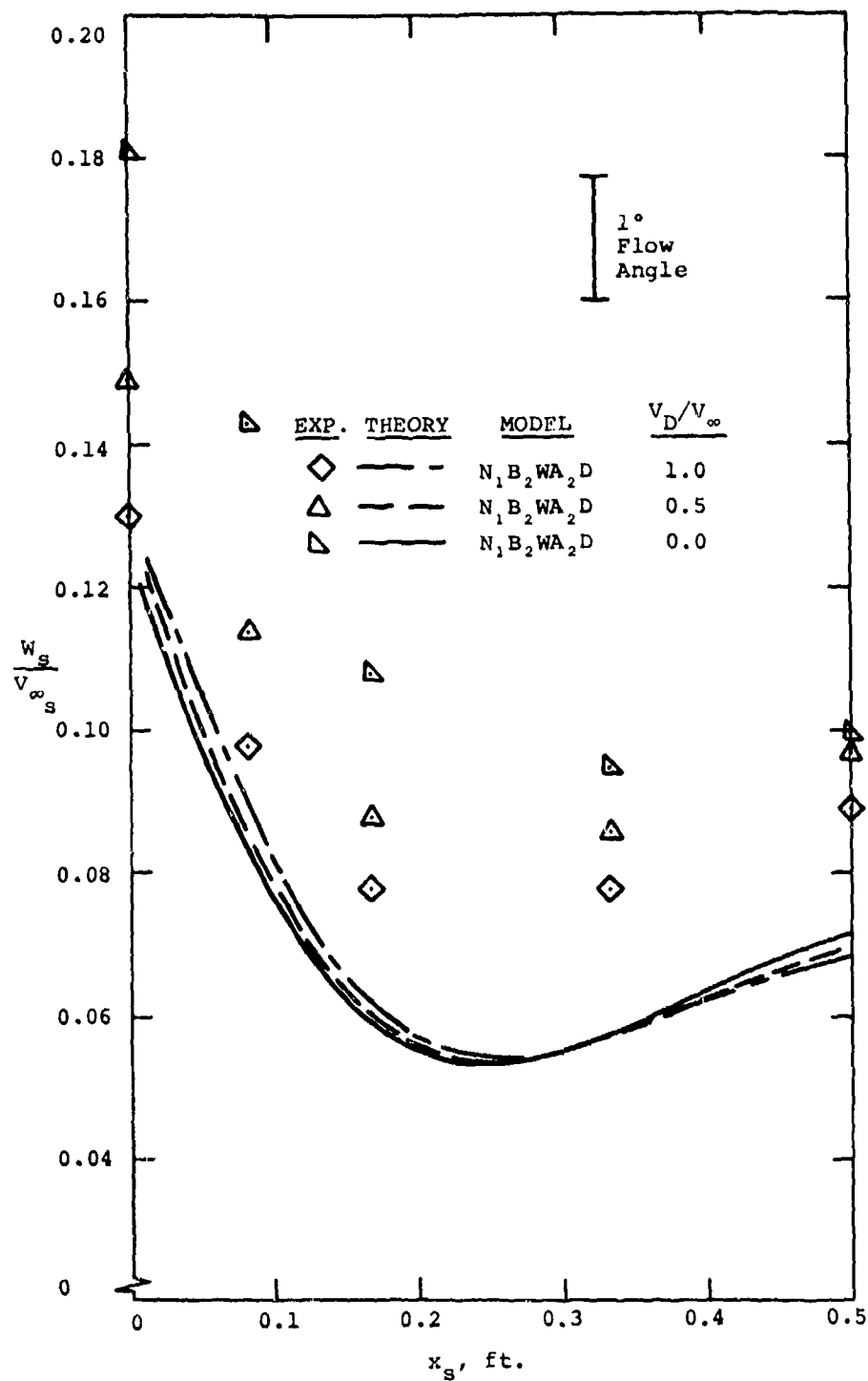


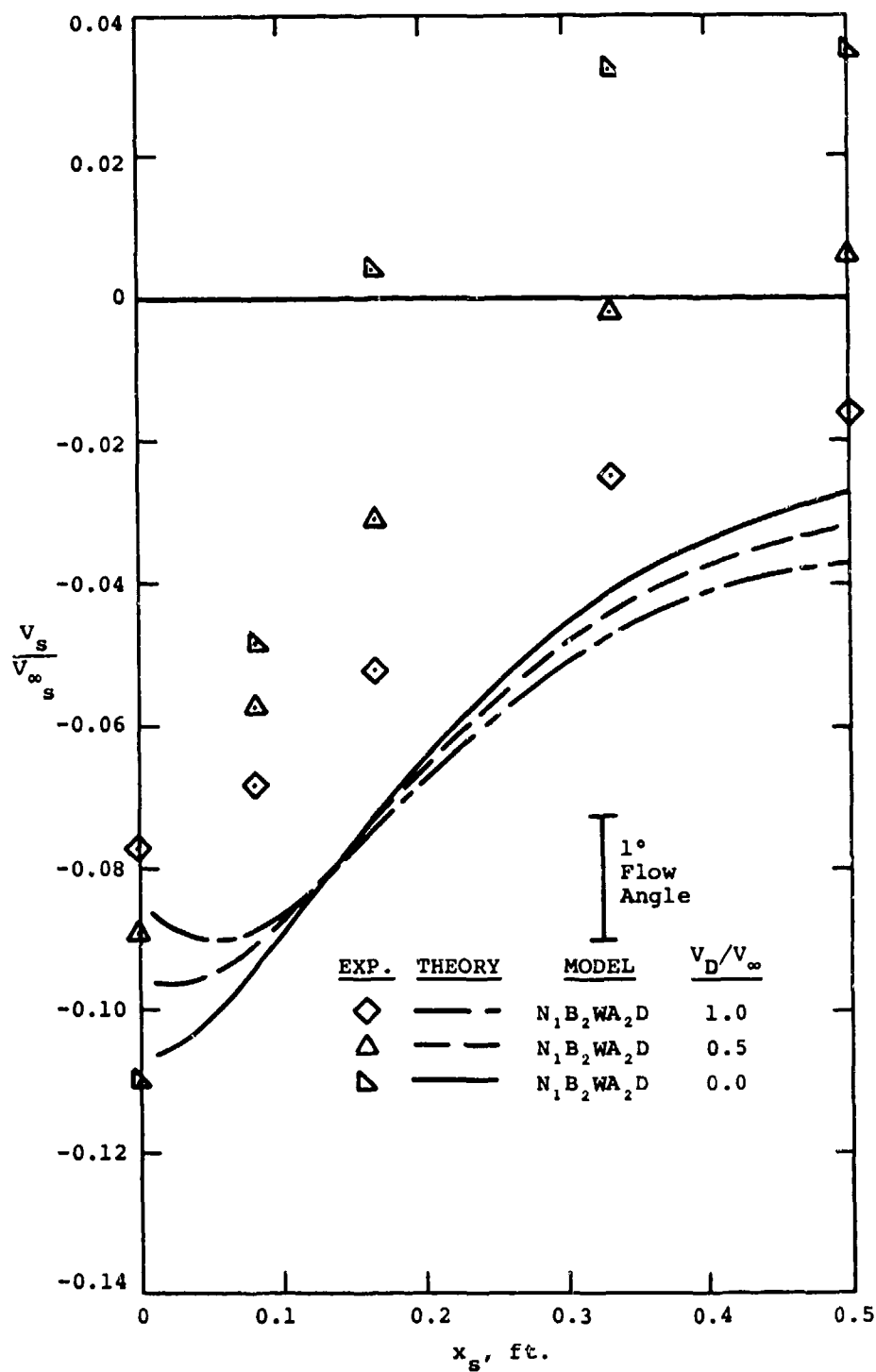
Figure 20.- Coordinate systems fixed in store and positive velocity and force and moment directions.



(a) Upwash distribution.

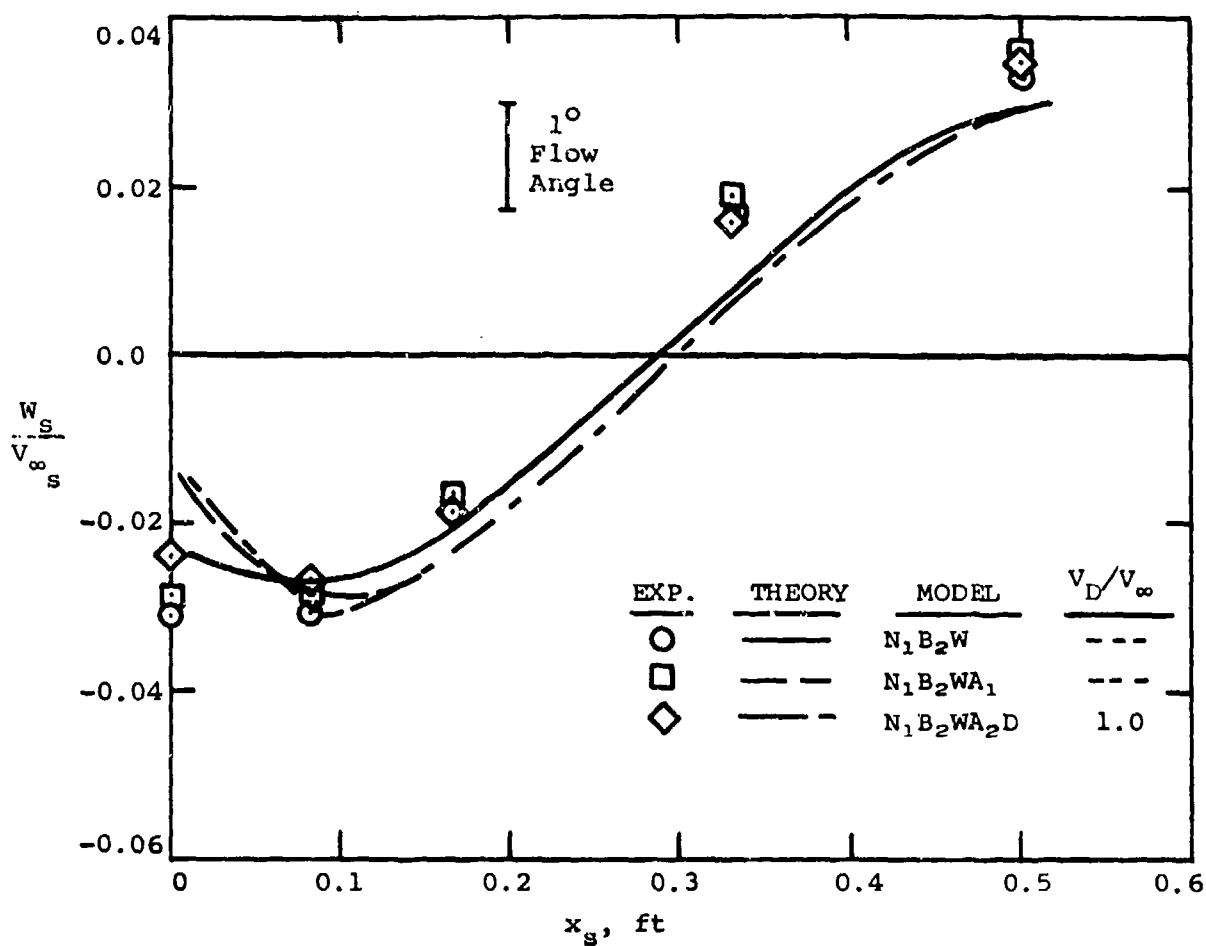
Figure 21.- Effect of air inlet velocity ratio on the flow field in the region the store centerline would occupy if the store was present;  
 $\alpha = 6^\circ$ ,  $M_\infty = 0.4$ .





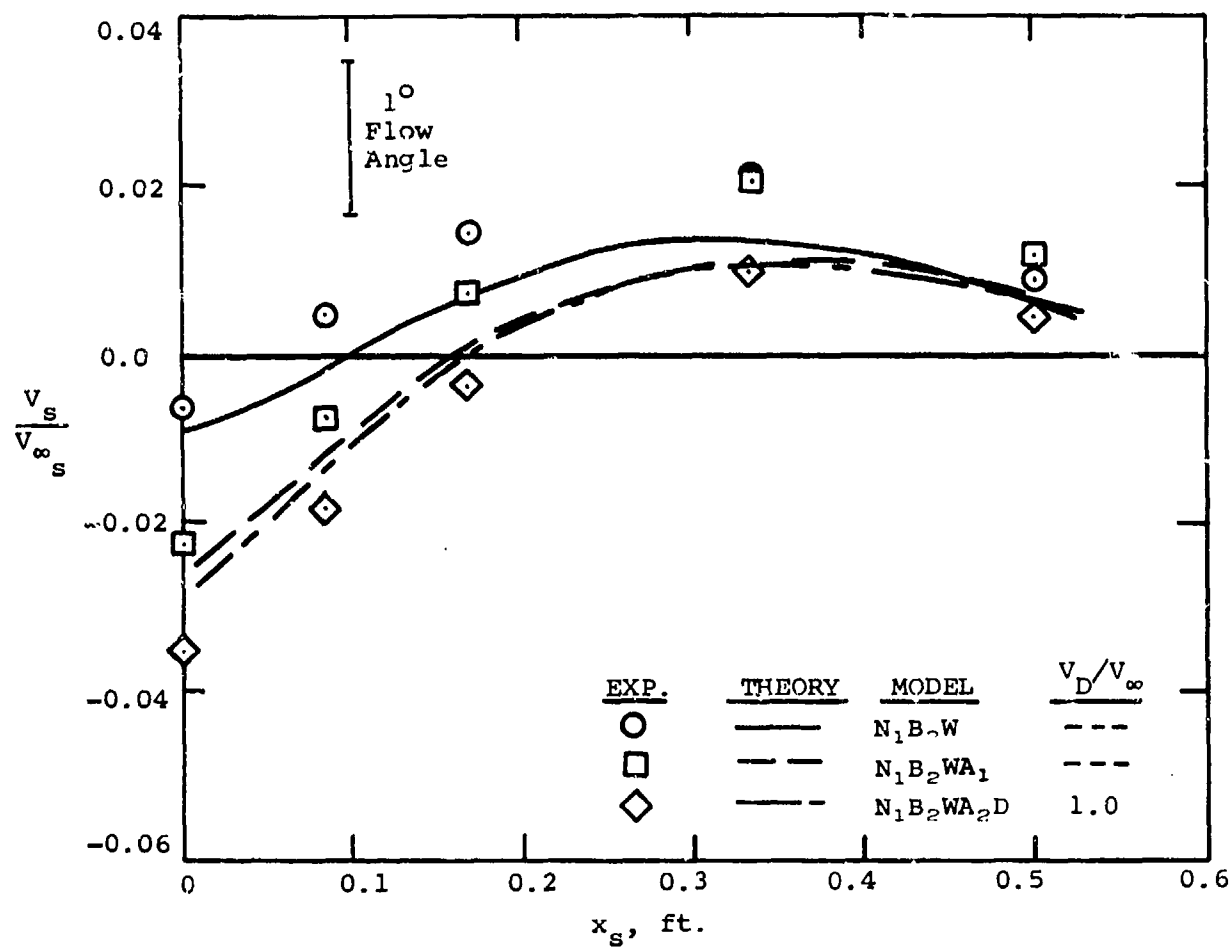
(b) Sidewash distribution.

Figure 21.- Concluded.



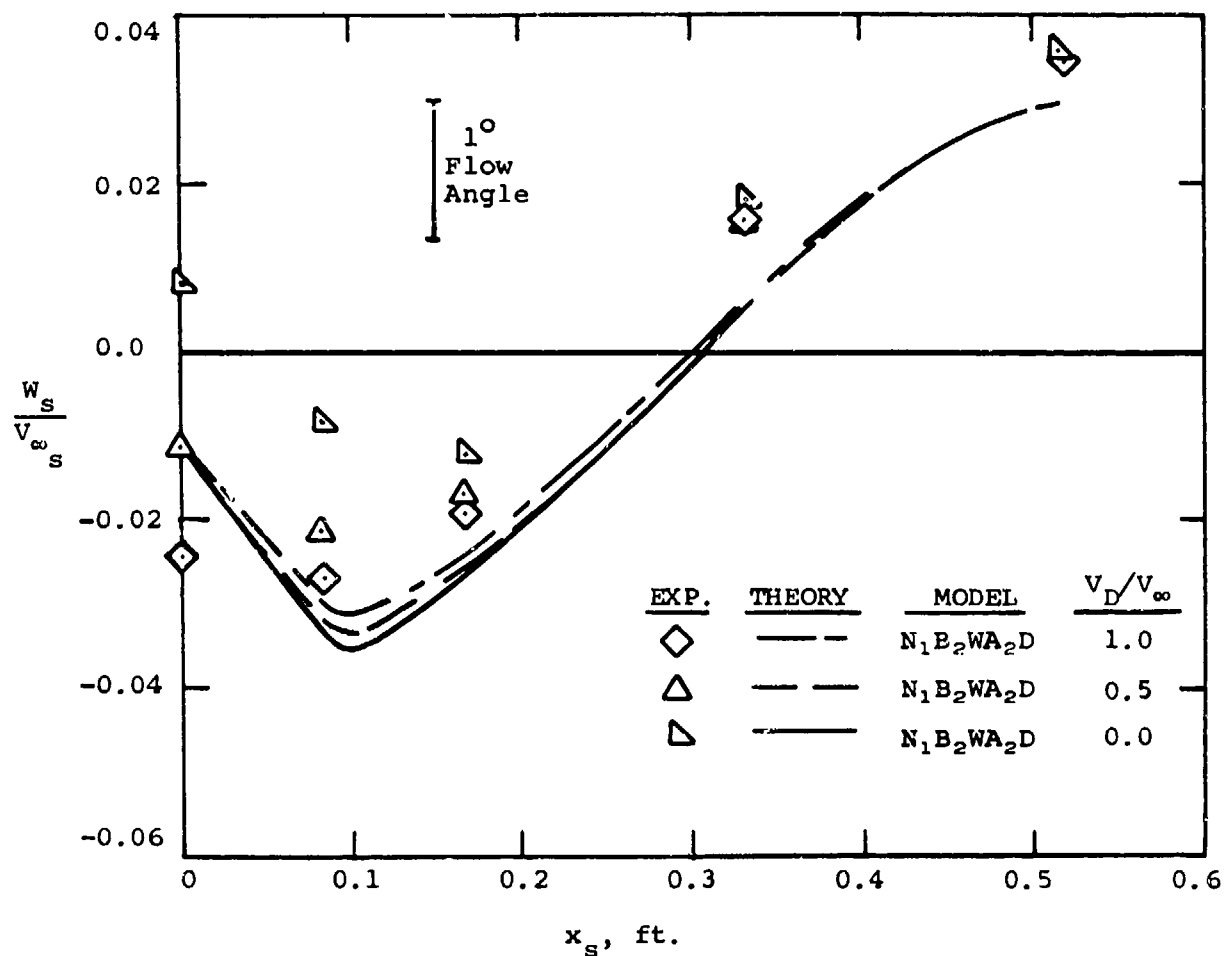
(a) Upwash distribution.

Figure 22.- Effect of wind-tunnel model build-up on the flow field in the region the store centerline would occupy if the store was present;  $\alpha = 0^\circ$ ,  $M_\infty = 0.4$ .



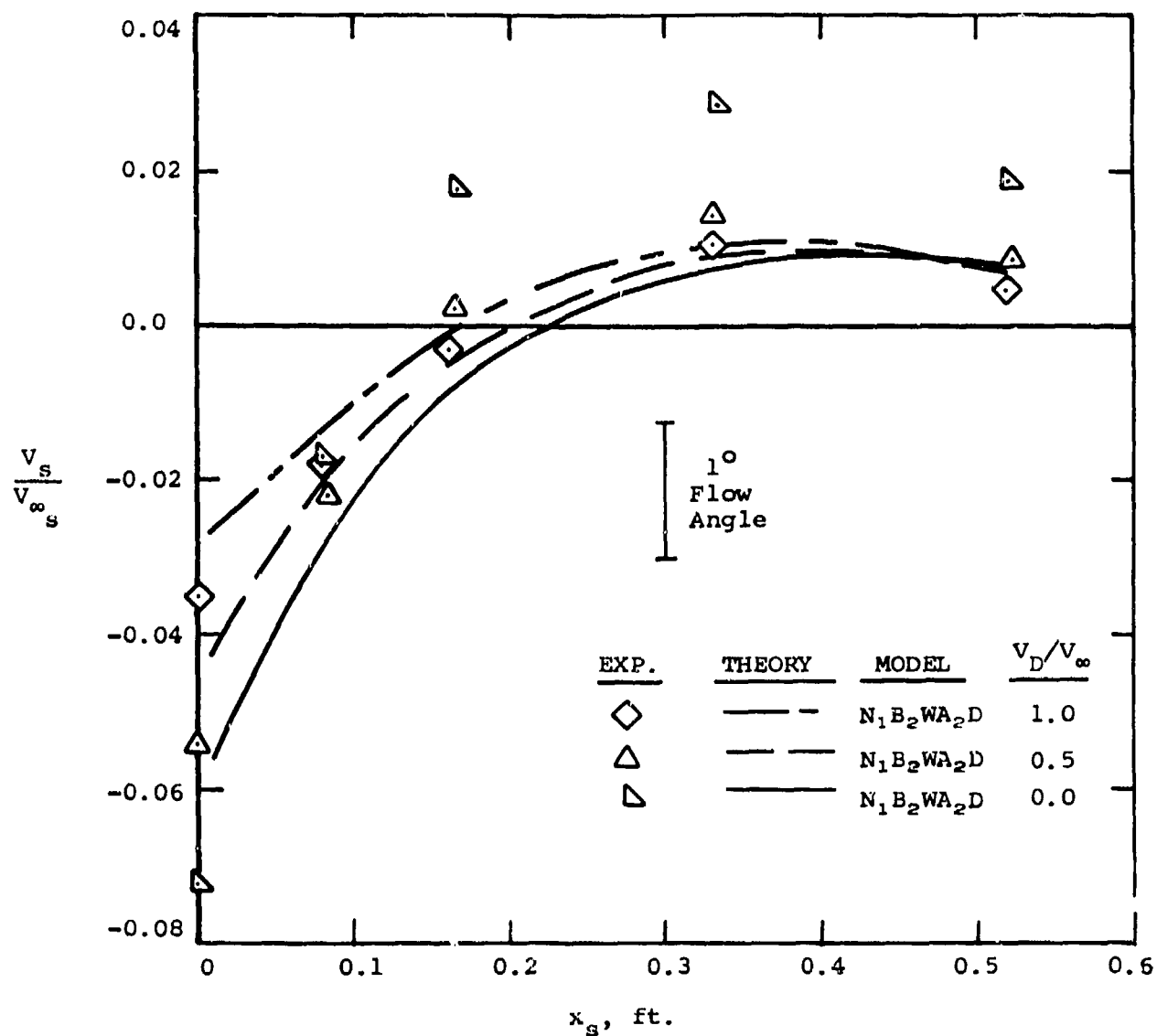
(b) Sidewash distribution.

Figure 22.- Concluded.



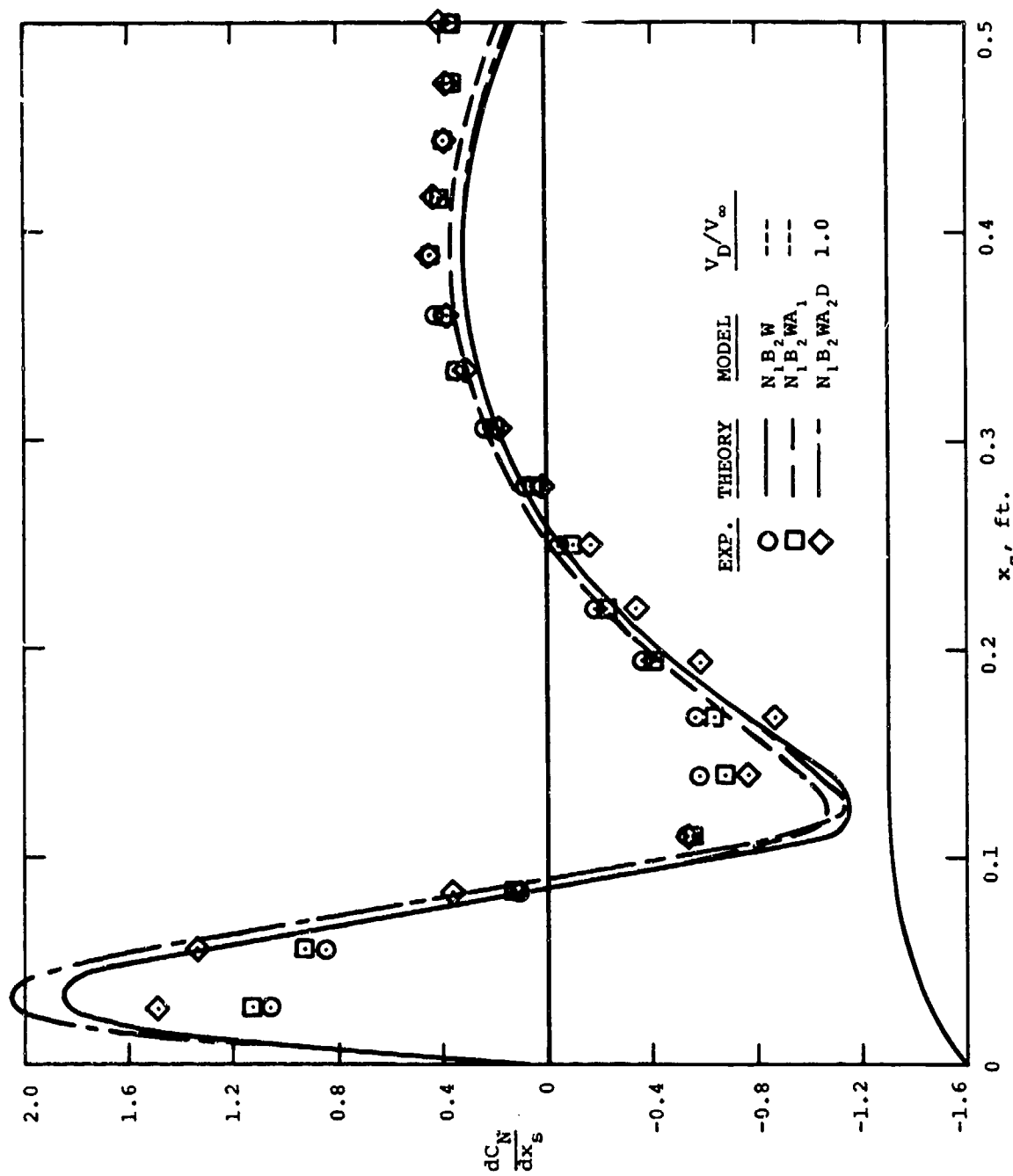
(a) Upwash distribution.

Figure 23.- Effect of air inlet velocity ratio on the flow field in the region the store centerline would occupy if the store was present;  $\alpha = 0^\circ$ ,  $M_\infty = 0.4$ .



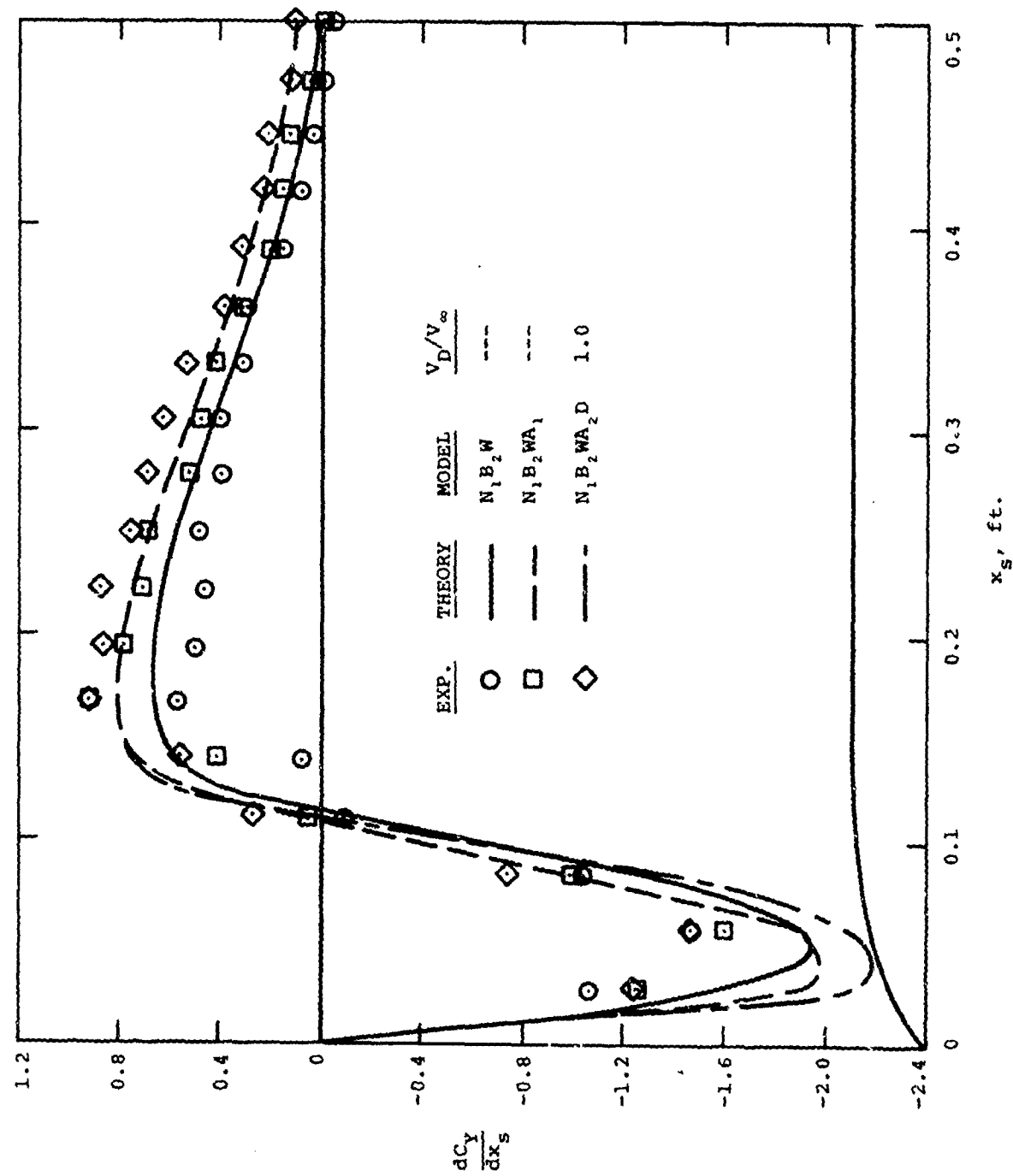
(b) Sidewash distribution.

Figure 23.- Concluded.



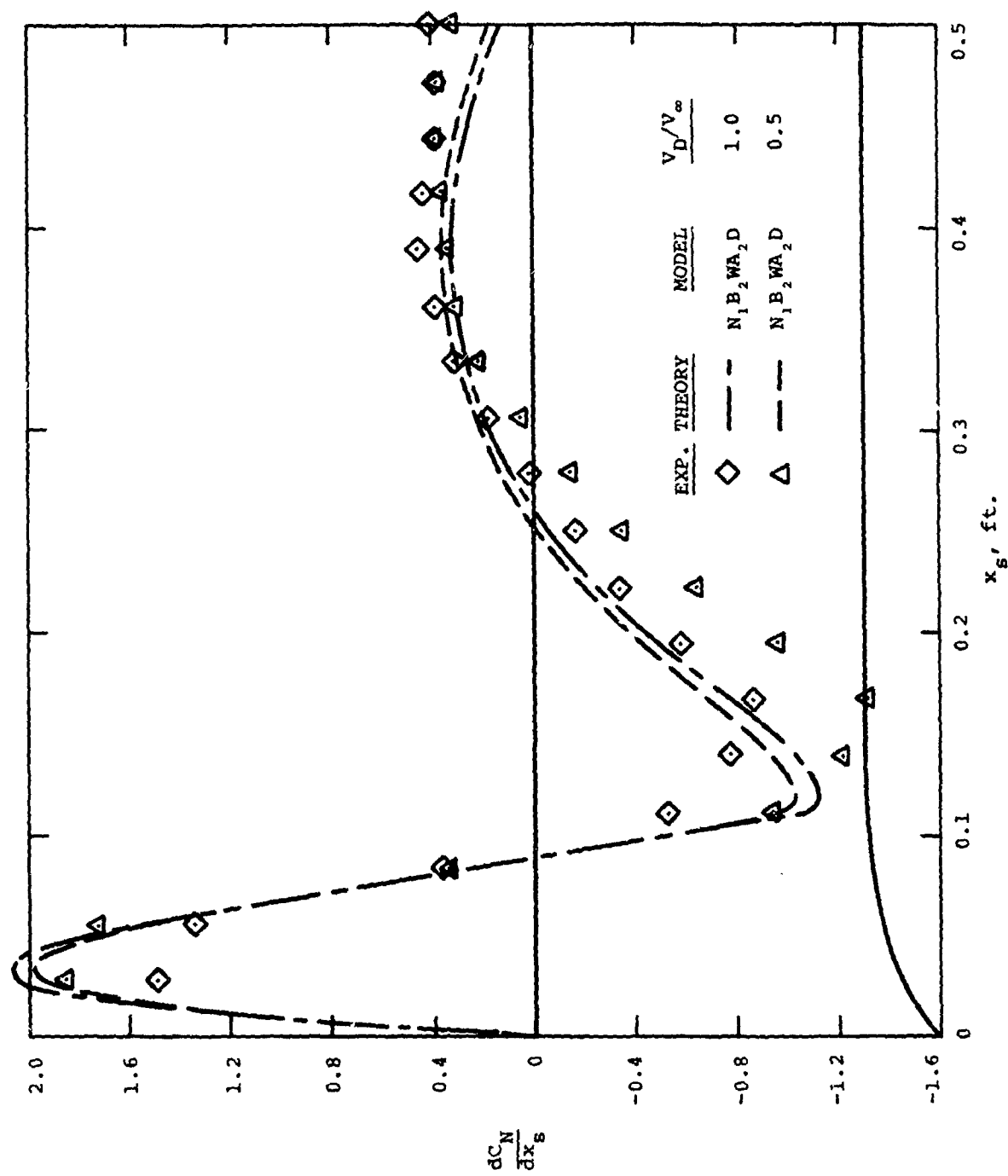
(a) Normal-force distribution.

Figure 24.- Effect of wind-tunnel model build-up on load distribution of attached store;  $\alpha = 6^\circ$ ,  $M_\infty = 0.4$ .



(b) Side-force distribution.

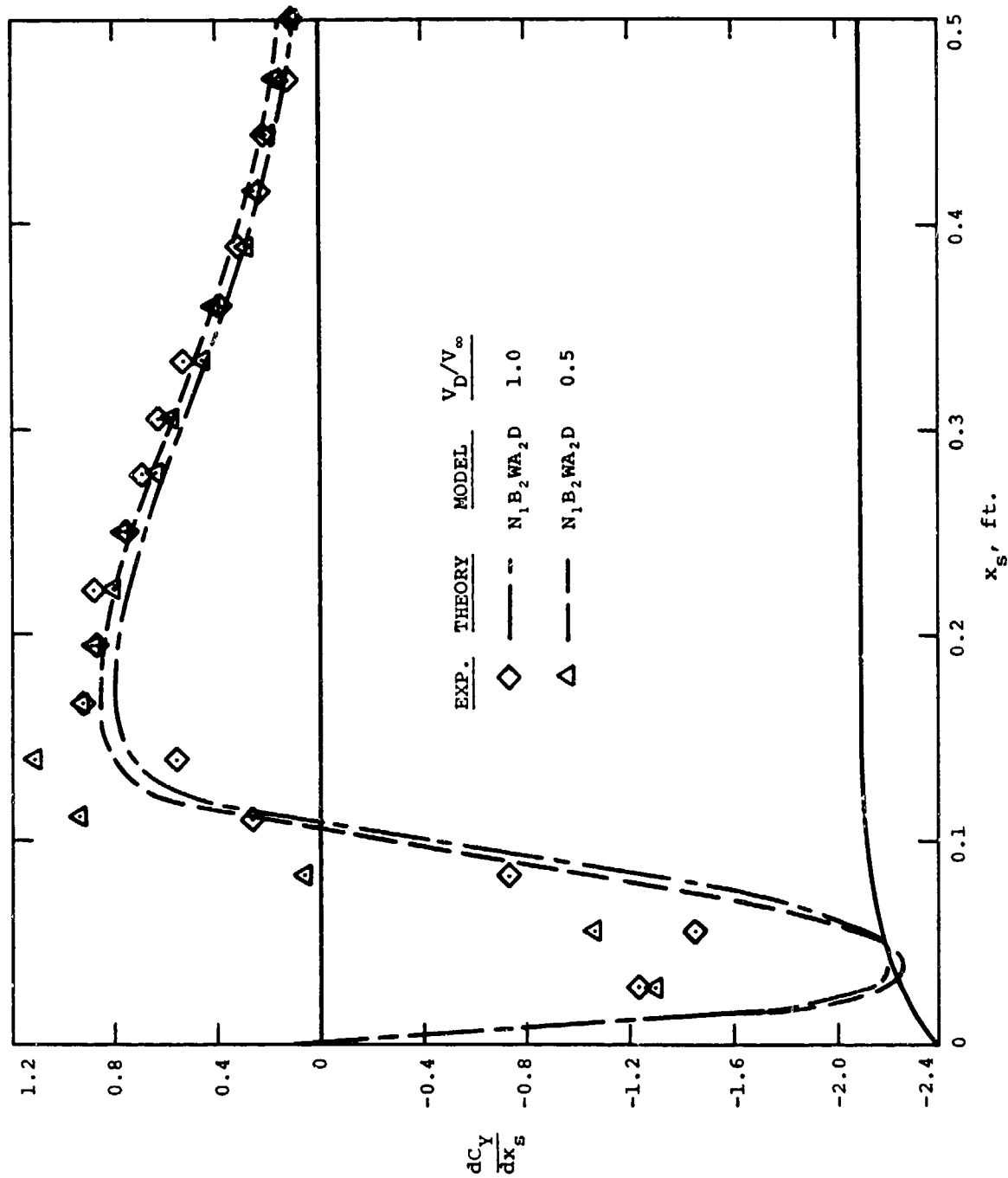
Figure 24.- Concluded.



(a) Normal-force distribution.

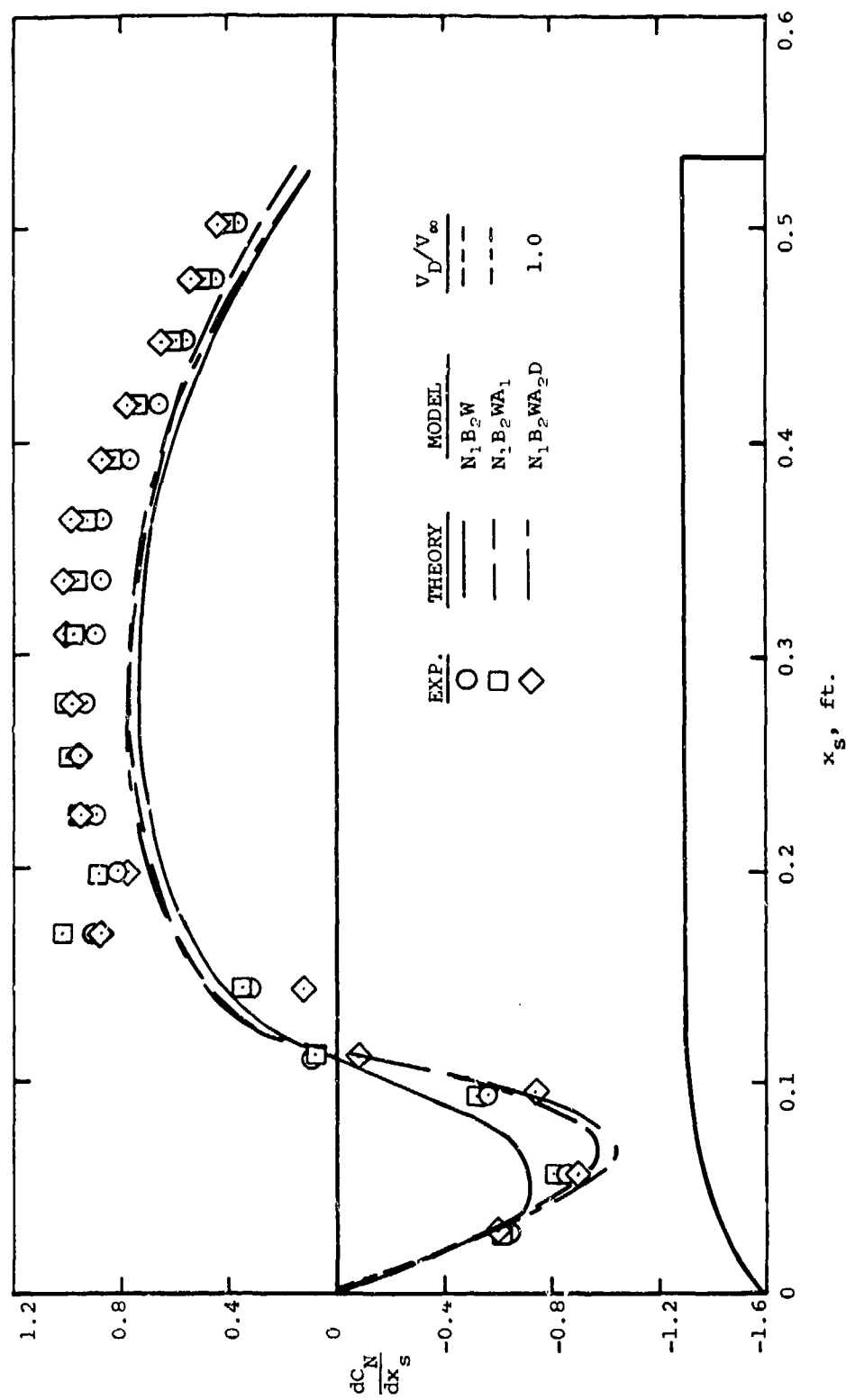
Figure 25.- Effect of inlet velocity ratio on load distribution of attached store;  $\alpha = 6^\circ$ ,  $M_\infty = 0.4$ .





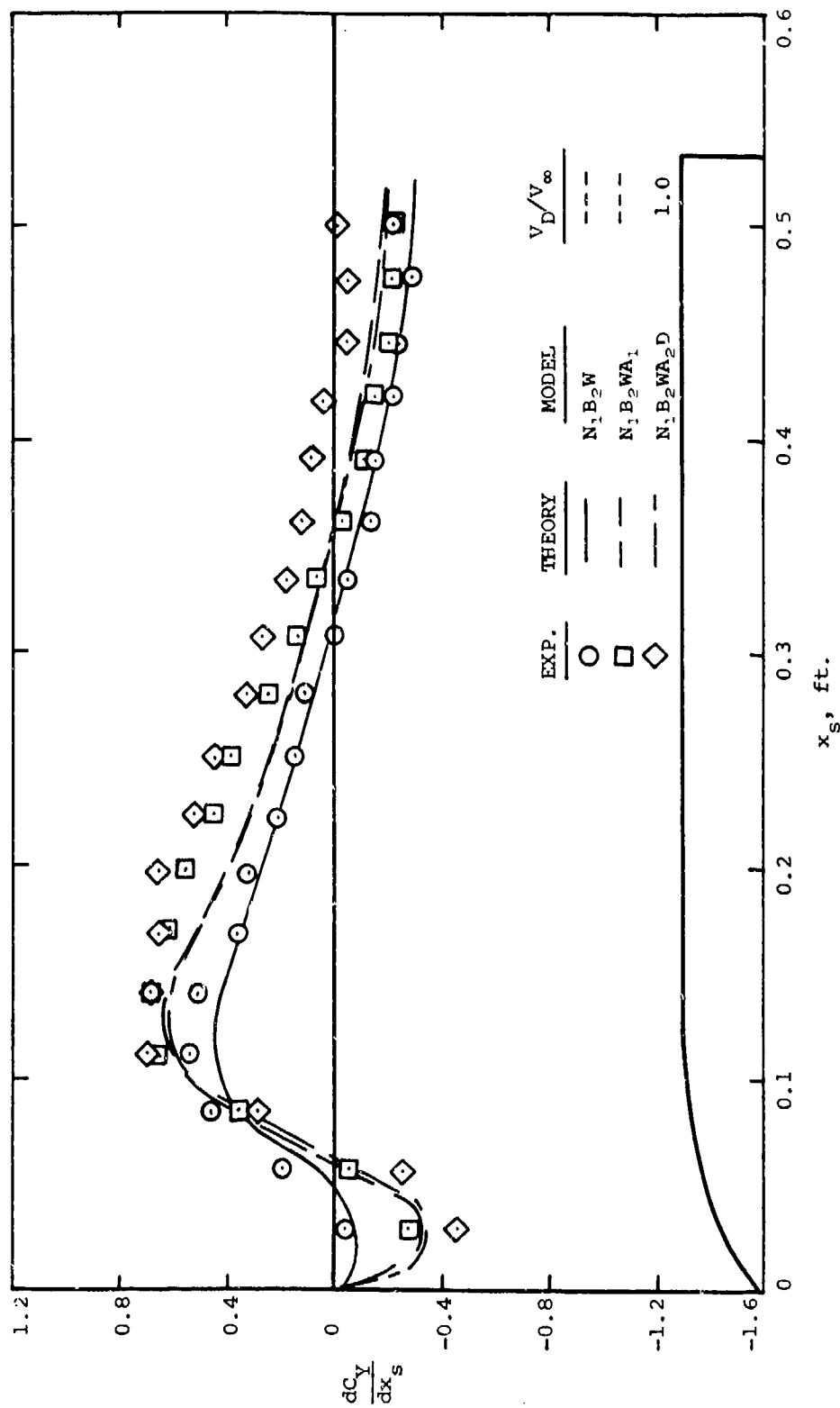
(b) Side force distribution.

Figure 25.- Concluded.



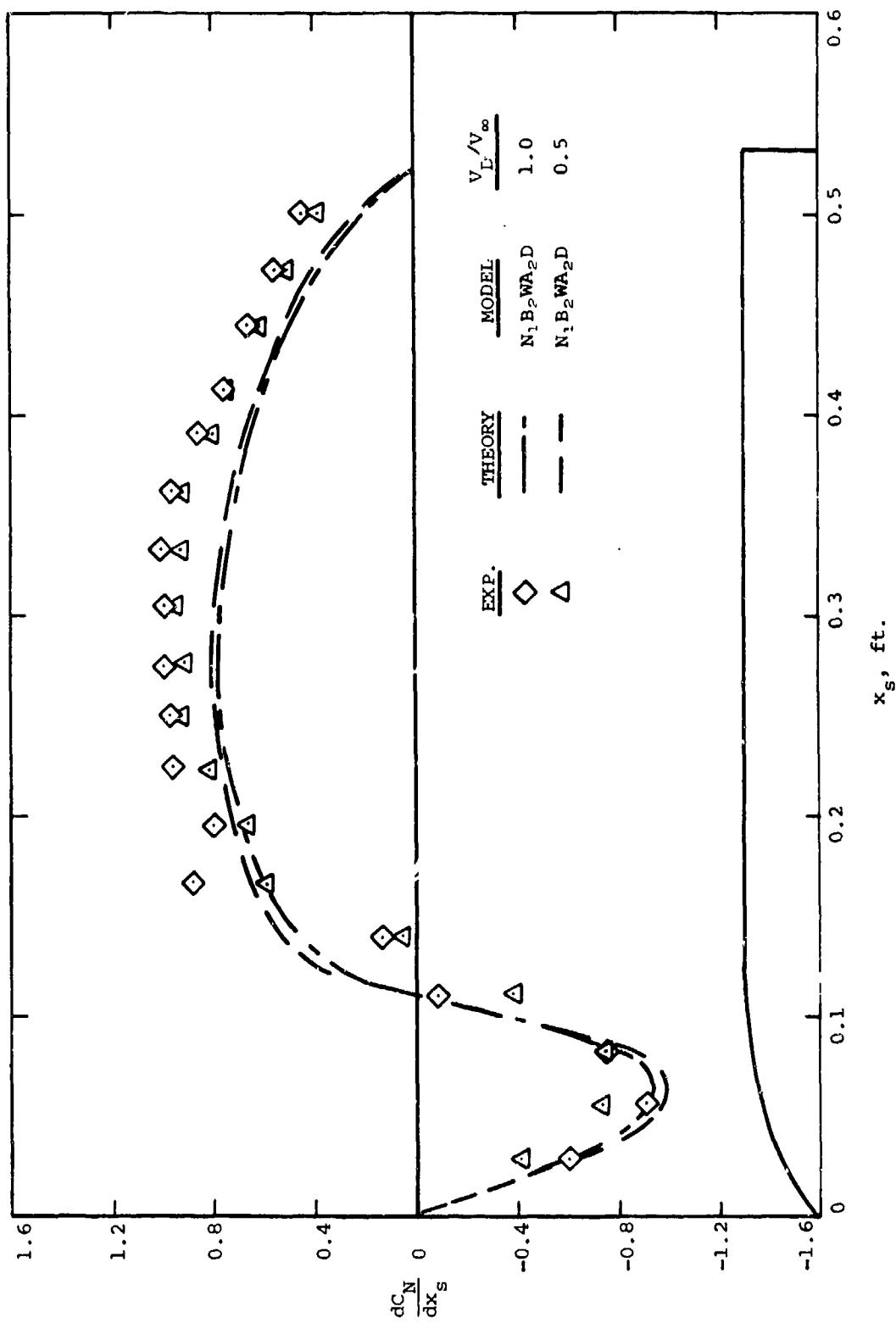
(a) Normal-force distribution.

Figure 26.- Effect of wind-tunnel model build-up on load distribution of attached store;  $\alpha = 0^\circ$ ,  $M_\infty = 0.4$ .



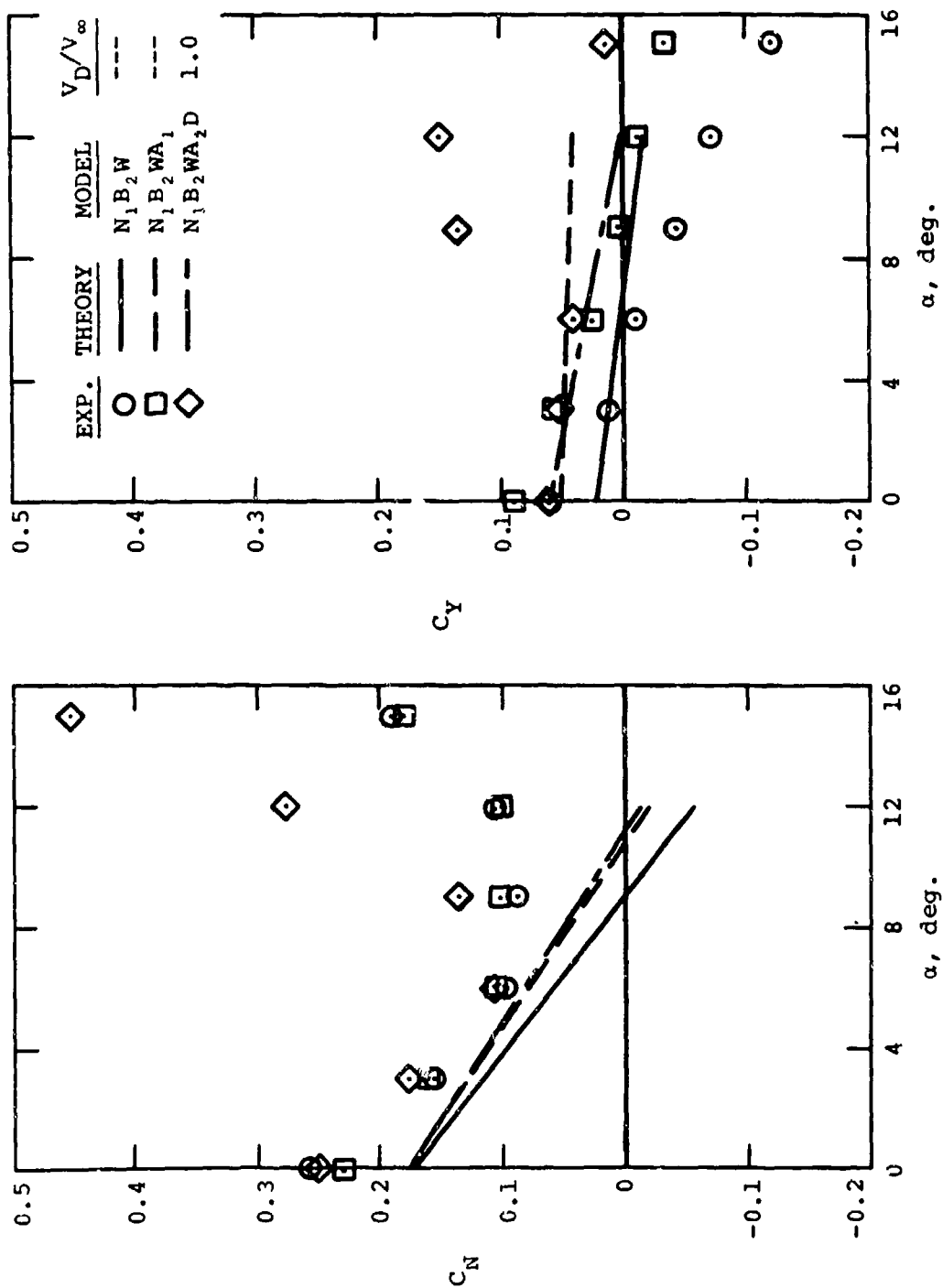
(b) Side-force distribution.

Figure 26.- Concluded.



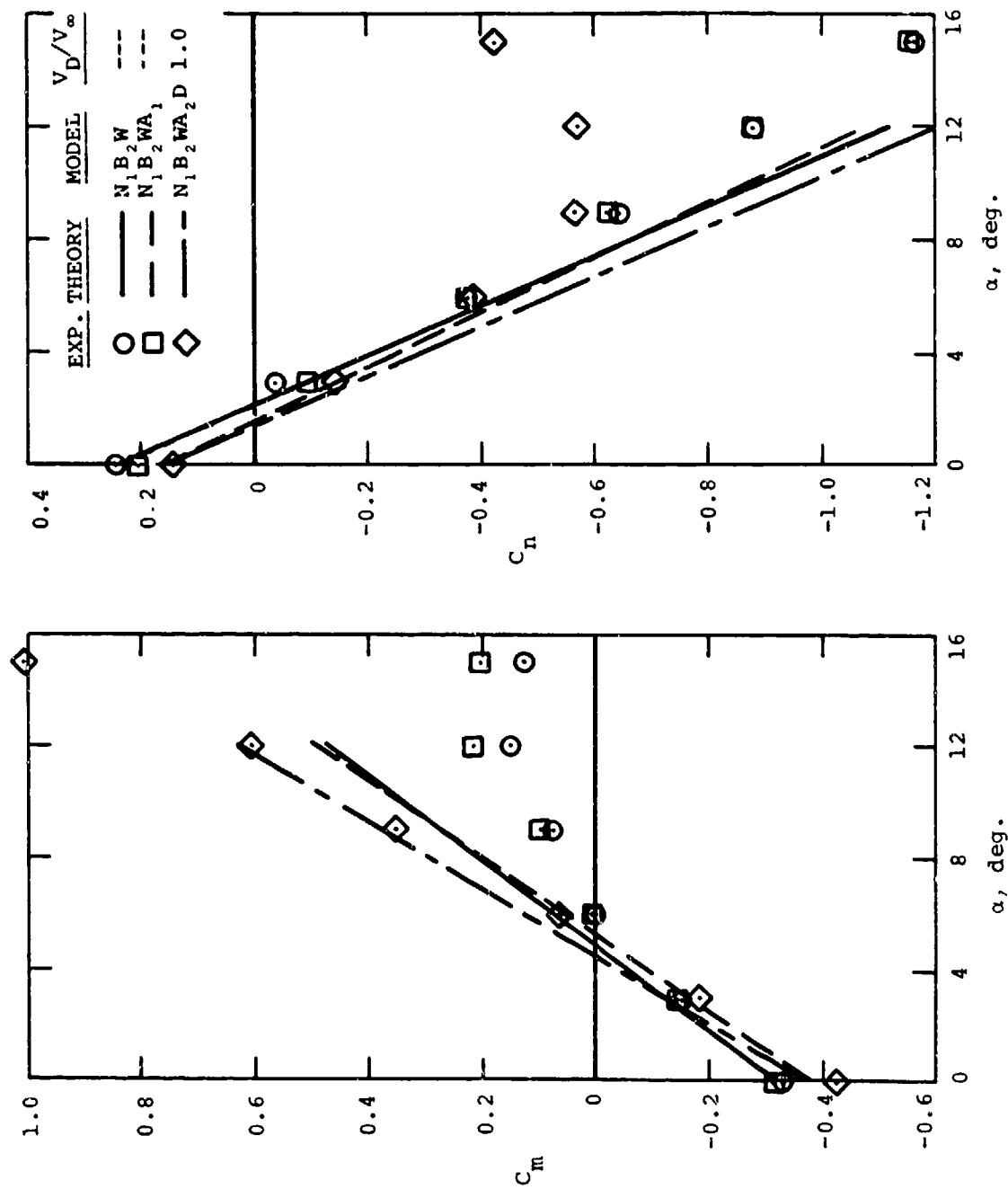
(a) Normal-force distribution.

Figure 27.- Effect of inlet velocity ratio on load distribution of attached store;  $\alpha = 0^\circ$ ,  $M_\infty = 0.4$ .



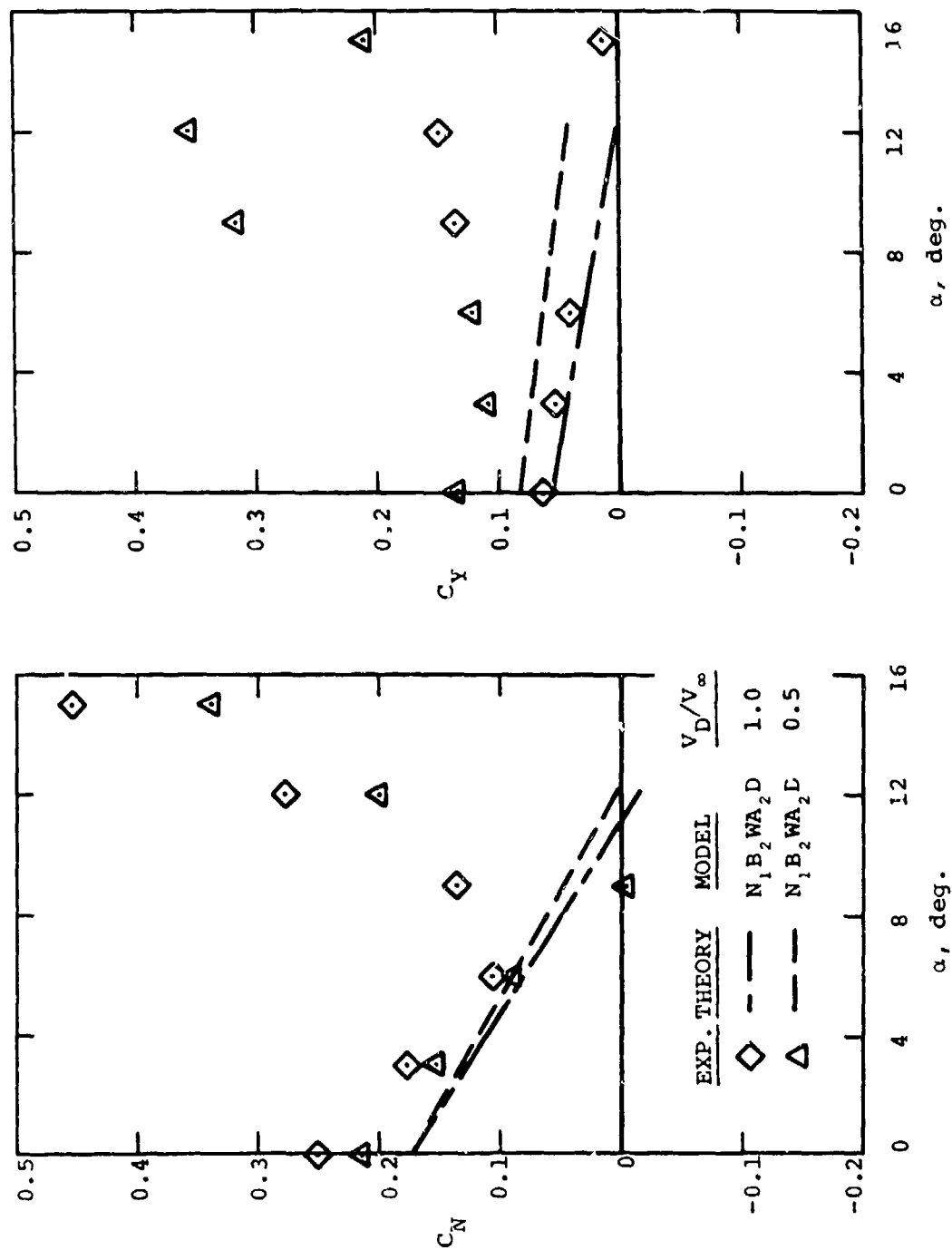
(a) Normal and side force coefficients.

Figure 28.- Effect of wind-tunnel model build-up on store forces and moments;  $M_\infty = 0.4$ .



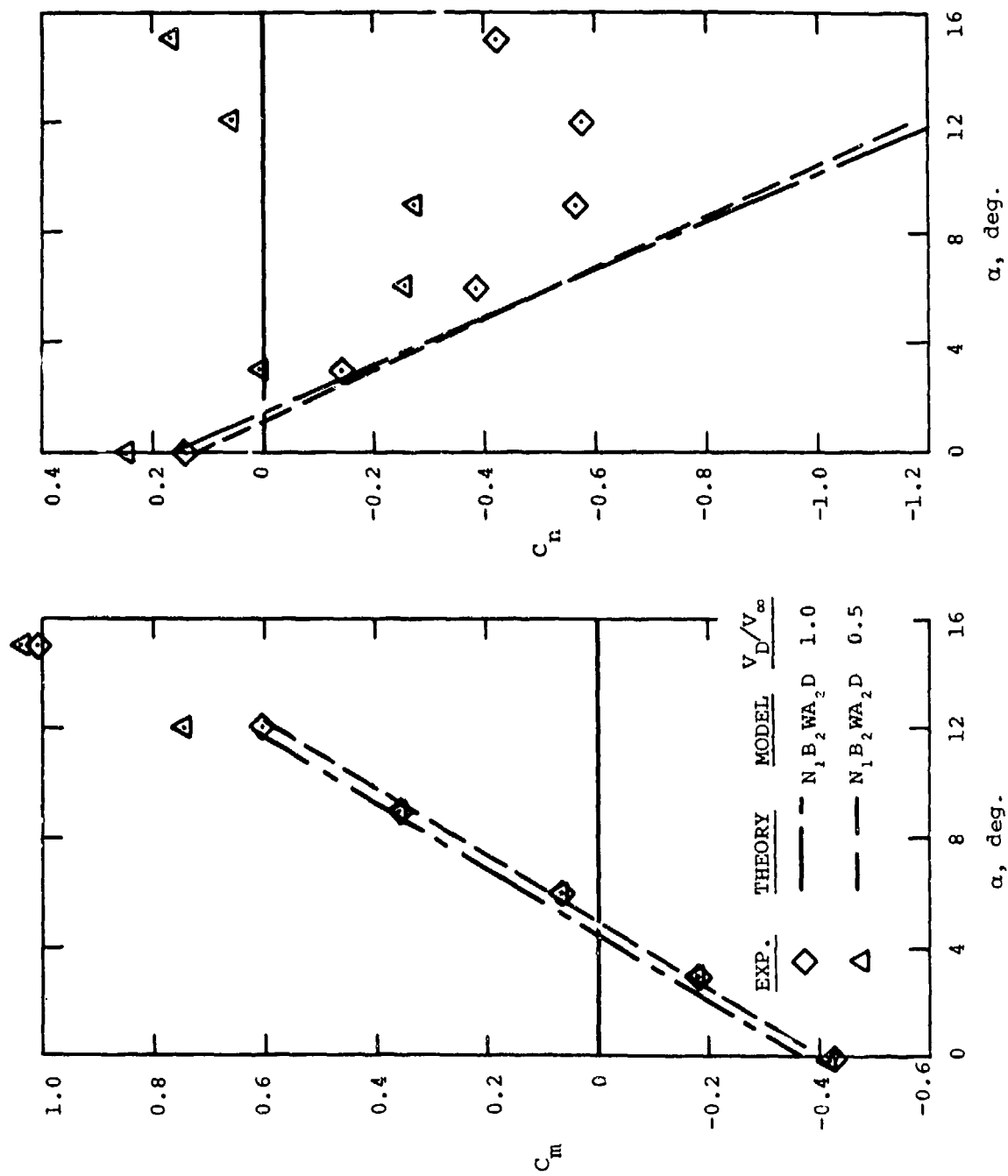
(b) Pitching- and yawing-moment coefficients.

Figure 28.- Concluded.



(a) Normal and side-force coefficients.

Figure 29.- Effect of inlet velocity ratio on store forces and moments;  $M_\infty = 0.4$ .



(b) Pitching- and yawing-moment coefficients.

Figure 29.- Concluded.



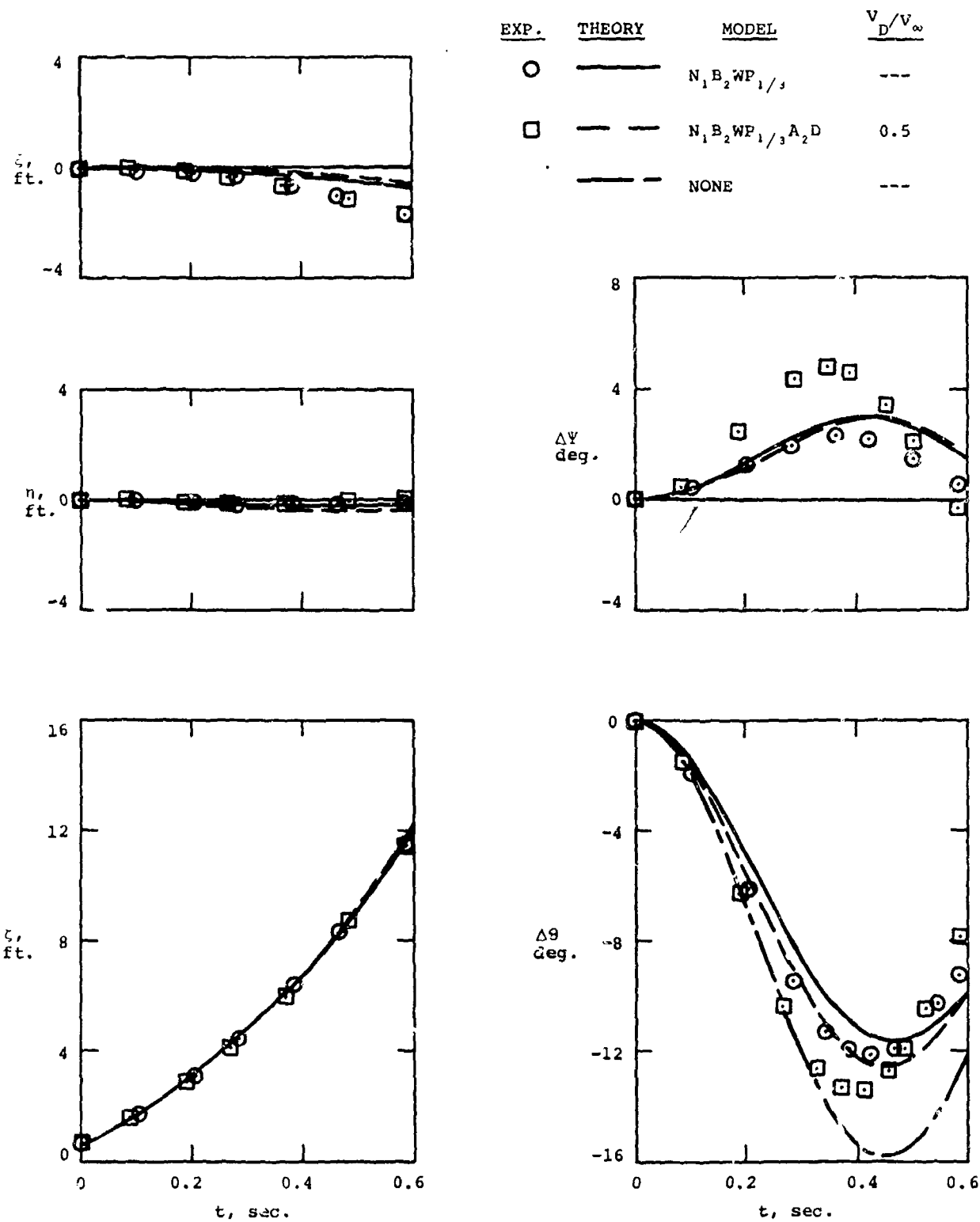


Figure 30.- Comparison between calculated and captive-store trajectories for a store released from the one-third semispan pylon;  $\alpha = 6^\circ$ ,  $M_\infty = 0.4$ , no damping.

# REFERENCES

1. Goodwin, F. K., Dillenius, M. F. E., and Nielsen, J. N.: Prediction of Six-Degree-of-Freedom Store Separation Trajectories at Speeds up to the Critical Speed. Volume I - Theoretical Methods and Comparisons with Experiment. Tech. Rept. AFFDL-TR-72-83, Vol. I, Oct. 1972.
2. Goodwin, F. K. and Dillenius, M. F. E.: Prediction of Six-Degree-of-Freedom Store Separation Trajectories at Speeds up to the Critical Speed. Volume II - Users Manual for the Computer Programs. Tech. Rept. AFFDL-TR-72-83, Vol. II, Oct. 1973.
3. Goodwin, F. K., Nielsen, J. N., and Dillenius, M. F. E.: A Method for Predicting Three-Degree-of-Freedom Store Separation Trajectories at Speeds up to the Critical Speed. Tech. Rept. AFFDL-TR-71-81, July 1971.
4. Nielsen, J. N.: Missile Aerodynamics. McGraw-Hill Book Co., Inc., New York, N.Y., 1960, pp. 40-48 and 55-59.
5. Ashley, H. and Landahl, M.: Aerodynamics of Wings and Bodies. Addison-Wesley Publishing Company, Inc., Reading, Mass., 1965, pp. 107-110.
6. Davis, H. F.: Introduction to Vector Analysis. Allyn and Bacon, Inc., Boston, Mass., 1962, p. 151.
7. Wylie, Jr., C. R.: Advanced Engineering Mathematics. McGraw-Hill Book Co., Inc., New York, N.Y., 1960, pp. 177-178.
8. Ward, G. N.: Supersonic Flow Past Slender Pointed Bodies. Quart. J. Mech. and Appl. Math., vol. 2, part I, 1949.
9. Milne-Thomson, L. M.: Theoretical Hydrodynamics. Fifth ed., The MacMillan Company, New York, N.Y., 1968, pp. 364-368.
10. Glauert, H.: The Elements of Airfoil and Airscrew Theory. MacMillan Press, 1943, chapter 12, pp. 156-160.